UCRL-51797

PROGRESS ON THE CONCEPTUAL DESIGN OF A MIRROR HYBRID FUSION-FISSION REACTOR

R. W. Moir, J. D. Lee, R. J. Burleigh, W. L. Barr,
J. H. Fink, G. W. Hamilton, D. J. Bender, G. A. Carlson,
W. L. Dexter, J. Holdren, C. L. Folkers, M. A. Peterson,
M. E. Rensink, H. W. Patterson, R. L. Nelson, C. E. Taylor

June 25, 1975

Prepared for U.S. Energy Research & Development Administration under contract No. W-7405-Eng-48

Printed in the United States of America
Available from
National Technical Information Service
U. S. Department of Commerce
5285 Port Royal Road
Springfield, Virginia 22151
Price: Printed Copy $___*; Microfiche $2.25

*Pages	NTIS Selling Price
1-50	$4.00
51-150	$5.45
151-325	$7.60
326-500	$10.60
501-1000	$13.60

Distribution Category
UC-20

LAWRENCE LIVERMORE LABORATORY
University of California/Livermore, California/94550

UCRL-51797

PROGRESS ON THE CONCEPTUAL DESIGN OF A MIRROR HYBRID FUSION-FISSION REACTOR

R. W. Moir, J. D. Lee, R. J. Burleigh, W. L. Barr,
J. H. Fink, G. W. Hamilton, D. J. Bender, G. A. Carlson,
W. L. Dexter, J. Holdren, C. L. Folkers, M. A. Peterson,
M. E. Rensink, H. W. Patterson, R. L. Nelson, C. E. Taylor

MS. date: June 25, 1975

26

Contents

PROGRESS ON THE CONCEPTUAL DESIGN OF A MIRROR HYBRID FUSION-FISSION REACTOR

Abstract

A conceptual design study has been made of a fusion-fission reactor for the purpose of producing fissile material and electricity. The fusion component is a D-T plasma confined by a pair of magnetic mirror coils in a Yin-Yang configuration and is sustained by neutral beam injection. The neutrons from the fusion plasma drive the fission assembly which is composed of natural uranium carbide fuel rods clad with stainless steel and helium cooled. We have shown conceptually how the reactor might be built using essentially present-day technology and how the uranium-bearing blanket modules can be routinely changed to allow separation of the bred fissile fuel. Averaged over the 30-year life of the plant with an 80% duty factor, the plutonium production is 690 kg per year and the electricity production is 480 MW_e-years per year (610 MW_e). The 20-atm helium gas used as a coolant is contained by thin-walled stainless steel pressure vessels surrounding cylindrical bundles of fuel rods. The engineered safeguards that prevent release and escape of radioactive material in the case of a loss of coolant accident are briefly addressed. The neutral beam injectors employ a direct energy converter for recovery of ions not converted to neutrals. The efficiency of producing the 100-keV D^0 and 150-keV T^0 is approximately 70%. The capital cost of the plant is $1200 million. Assuming a 14% return on capital and an 80% duty factor, the electrical cost would be 40 mills per $kW_e h$ if the plutonium were sold at $20/g. The design is not optimized, and we give examples of projected designs having costs about half those above.

I. Introduction

It may be possible and advantageous to obtain fissile fuel and/or electrical energy from the combination of fusion and fission. The major advantage of combining fusion and fission is that the weaknesses of each are offset by their respective strengths; that is, fusion is neutron rich but power poor, while fission is neutron poor but power rich. The 14-MeV neutrons resulting from the fusion reactions can be used to drive a subcritical fission blanket that surrounds the plasma.

Several combinations of fusion reactors and fission reactors have been suggested and are reviewed in Ref. 1-1. This report describes our work on the conceptual design of one particular fusion-fission hybrid reactor — one which emphasizes both fissile fuel and electrical production by using the 14-MeV fusion neutrons produced in a magnetic

mirror-confined D-T plasma as a source to drive a subcritical, unmoderated assembly of natural uranium. This assembly surrounds the plasma and is called a "blanket". The 14-MeV fusion neutrons are used to directly fission the abundant uranium isotope (^{238}U), and the additional neutrons generated are captured in ^{238}U and ^{6}Li to produce ^{239}Pu and tritium.

It should be possible to utilize one or several of the existing or nearly developed fission technologies for the blanket. In a previous study,[1-2] we looked at a high energy multiplying thermal lattice blanket based on the General Atomic graphite-moderated, helium-cooled reactor technology. For this present study, we chose a fast-spectrum blanket[1-3, 4] that has a lower energy multiplication but higher fissile fuel production compared to the thermal blanket and is based in part on the helium-cooled breeder reactor technology presently under development.

We show conceptual engineering approaches to problems such as removal of uranium-bearing blanket modules (for recovery of bred fissile fuel, and replacement of radiation-damaged structures) and the steady operation of high-powered, efficient, neutral beam injectors. The design combines fuel production with electrical power production. We have succeeded in obtaining a blanket design that we think could be built with essentially present-day fission technology and that would produce large amounts of fuel (690 kg of plutonium per year) and electricty (600 MW_e).

This report is organized so that the Summary (Section 2) can be read without reference to the rest of the report. For a more thorough understanding, the reader can refer to subsequent sections for in-depth discussions and much material presented for the first time.

REFERENCES

1-1. B. R. Leonard, "A Review of Fusion-Fission (Hybrid) Concepts," Nucl. Technol. 20 (1973).

1-2. W. C. Wolkenhauer, B. R. Leonard, Jr., A. M. Sutey, and R. W. Moir, "Conceptual Design of a Fusion-Fission Hybrid Reactor Based on a Mirror Fusion Reactor with a Subcritical Gas Cooled Fission Blanket," in Proc. First Topical Meeting on the Technology of Controlled Nuclear Fusion, 1974 (San Diego, CA, 1974), CONF-740402-P1, vol. 1, p. 238.

1-3. J. D. Lee, "Neutronic Analysis of a 2500 MW_{th} Fast Fission Natural Uranium Blanket for a DT Fusion Reactor," in Proc. First Topical Meeting on the Technology of Controlled Nuclear Fusion, 1974 (San Diego, CA, 1974), CONF-740402-P1, vol. 1, p. 233; also LLL Rept. UCRL-75304 (1974).

1-4. J. D. Lee, "Neutronics of Sub-Critical Fast Fission Blankets for D-T Fusion Reactors," in Proc. 7th Conf. Intersociety Energy Conversion Engineering, 1972 (American Chemical Society, 1972), p. 1294.

2. Summary

The objective of this work is to conceptually design a reactor that uses the 14-MeV neutrons from a mirror fusion reactor to release additional energy and produce plutonium in a natural uranium subcritical blanket that surrounds the fusion plasma. Although preliminary, the design is sufficiently detailed to permit an assessment of the technological problems and to make a rough cost estimate. The design, then, is in effect a reference design of a mirror fusion-fission reactor, although preliminary and not optimized.

The high-temperature deuterium and tritium fuel ions are confined in a magnetic field whose strength increases everywhere away from the center, i.e., in a magnetic well. The field shape is produced by the "Yin-Yang" coil shown in Fig. 2-1. The

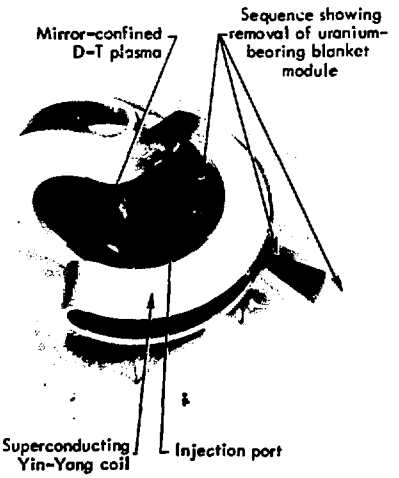

Fig. 2-1. Yin-Yang coil.

virtue of the magnetic well configuration is that the plasma is stable to gross lateral displacements; a fact well established by laboratory experience. The particle confinement transverse to the magnetic field is exceedingly good — almost perfect. Along the field, the magnetic-mirror, or reflection principle, causes those particles having sufficient transverse energy to be reflected by the increased magnetic field at the ends. However, collisons among fuel ions and electrons cause transverse energy to be converted to parallel energy (and vice versa) and destroy the reflection property, thus causing the fuel ions to "leak" out the ends of the magnetic container. We calculate this collisional loss rate with Fokker-Planck transport codes to determine the expected particle confinement time, τ; and for our case, we find $n\tau = 2.7 \times 10^{13}$ cm^{-3}·s (where n is the density of deuterium and tritium ions inside the plasma).

Demonstration of this $n\tau$ value is the only remaining problem in scientific feasibility. A class of instabilities known as microinstabilities has been predicted and observed, and there is the possibility that such effects could decrease the value of $n\tau$ to unacceptably low values. Accordingly, the main thrust of the research program on magnetic mirror confinement is directed toward eliminating microinstabilities and obtaining higher $n\tau$ values in laboratory devices. For our reference case, we assume that the instabilities are suppressed so that the associated losses are small compared to collisional losses; however, in an earlier study[2-1] we

investigated a reactor system with a high-energy multiplication blanket that could tolerate instability losses which doubled or tripled the loss rate.

The plasma in our reference design is fueled and sustained by the steady injection of neutral deuterium (100-keV) and tritium (150-keV) atoms. Figure 2-2 shows one of the four injectors. These fast atoms are produced by first accelerating positive ions, then passing them through a deuterium or tritium gas cell where about half are neutralized by electron capture. The neutralized particles continue into the plasma and are captured by ionization. The remaining ions are decelerated and collected in a direct energy converter, where most of their energy is converted back into electrical energy.

Processes such as electron capture and penetration into the plasma are the same for both deuterium and tritium traveling at the same speed; that is why we have the tritium more energetic than the deuterium. The efficiency of depositing energy in the plasma via the neutral atoms is estimated to be 70%. The injected neutral beam power that is trapped is 225 MW, and the trapped current is 1270 A of deuterium and 630 A of tritium. The fraction of the neutral beam that is trapped is 0.94.

The plasma that leaks out of the confinement region carries 225 MW of power and is recovered at 50% efficiency in a simple, one-stage direct energy converter. This recovered 112 MW of dc power is used to supply part of the 325 MW of power consumed by the injector. Helium ions produced by D-T fusion reactions carry away 42 MW of power, which is converted in a thermal cycle only. The energy of the helium ions is not converted directly because they are born at 3.5 MeV and do not thermalize before escaping confinement.

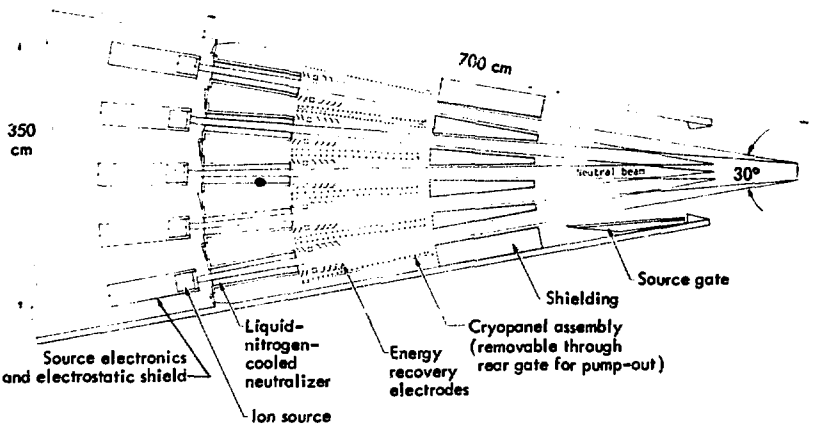

Fig. 2-2. Side view of neutral beam injector.

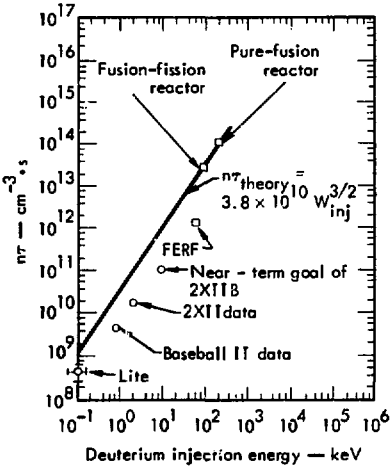

Fig. 2-3. Plasma parameters for hybrid and pure-fusion reactors.

The plasma parameters for the hybrid are

- $n\tau = 2.7 \times 10^{13}$ cm^{-3} · s,
- Deuterium injection energy, E_{inj} = 100 keV, and
- Q(Q is the ratio of fusion power taking 17.58 MeV per reaction to trapped injected power) ≈ 0.94.

For comparison, a pure fusion mirror reactor needs to have $n\tau \approx 1.0 \times 10^{14}$ cm^{-3} · s, E_{inj} = 200 keV, and Q ≈ 1.5; while the conceptual mirror fusion engineering research facility (FERF) has $n\tau = 1.9 \times 10^{12}$ cm^{-3} · s, E_{inj} = 65 keV, and Q ≈ 0.11. These operating parameters are shown in Fig. 2-3 along with earlier data from the Baseball-II and 2XII experiments at the Lawrence Livermore Laboratory (LLL), and the LITE experiment at the United Aircraft Research Laboratory. The near-term goal of the present 2XIIB experiment is also shown. The data points for the experiments and for FERF are below the line because they have smaller mirror ratios than either the pure-fusion or the fusion-fission reactor.

The blanket contains natural uranium fuel in the form of uranium carbide in stainless steel tubes. For breeding tritium, the blanket contains lithium in the form of small particles of $LiAlO_2$ in tubes or cans, with porous end caps to allow the tritium resulting from neutron capture in lithium to diffuse into the coolant stream from which the tritium is continuously removed. The coolant, helium gas at 20 atm, is contained in thin-walled (0.5-cm) stainless steel cylinders (30-cm diam × 100 cm long) having hemispherical ends. A model of the plasma, coil, and blanket configurations is shown in Fig. 2-1. A composite drawing of the blanket is shown in Fig. 2-4. A block diagram of the major components is shown in Fig. 2-5 along with the power-flow pattern. Not included in the power flow diagram (Fig. 2-5) or elsewhere in the report is the auxiliary power requirement of 25 MW for the refrigeration system for the magnets and cryogenic pumping system. This 25 MW represents only a 1% change in the thermal efficiency of the reactor. A cross section of the power plant is shown in Fig. 2-6 and an artist's view is shown in Fig. 2-7.

The D-T fusion reaction produces neutrons with 14 MeV of kinetic energy. Neutrons with kinetic energy above ~0.4 MeV can cause the nucleus of ^{238}U to fission. It is the potential use of fusion neutrons to directly fission this abundant (99.3%) isotope of uranium that this hybrid reactor concept is attempting to exploit. Both experiments and calculations

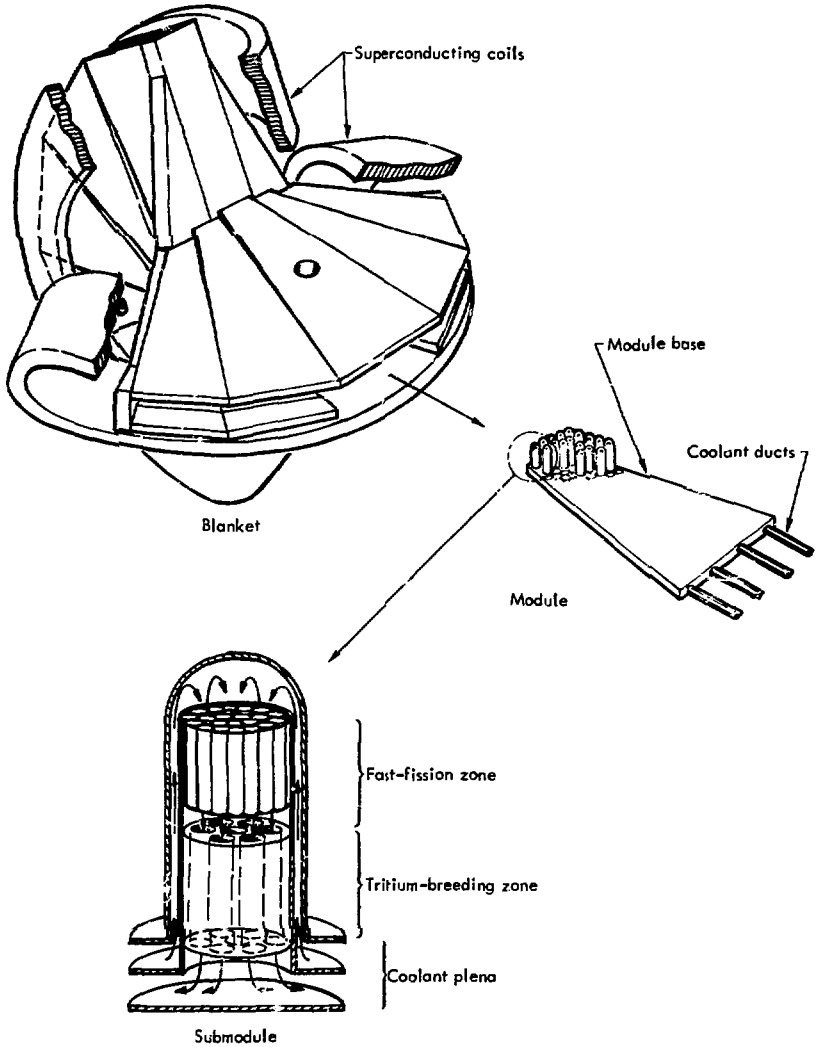

Fig. 2-4. Uranium-bearing blanket module and submodules.

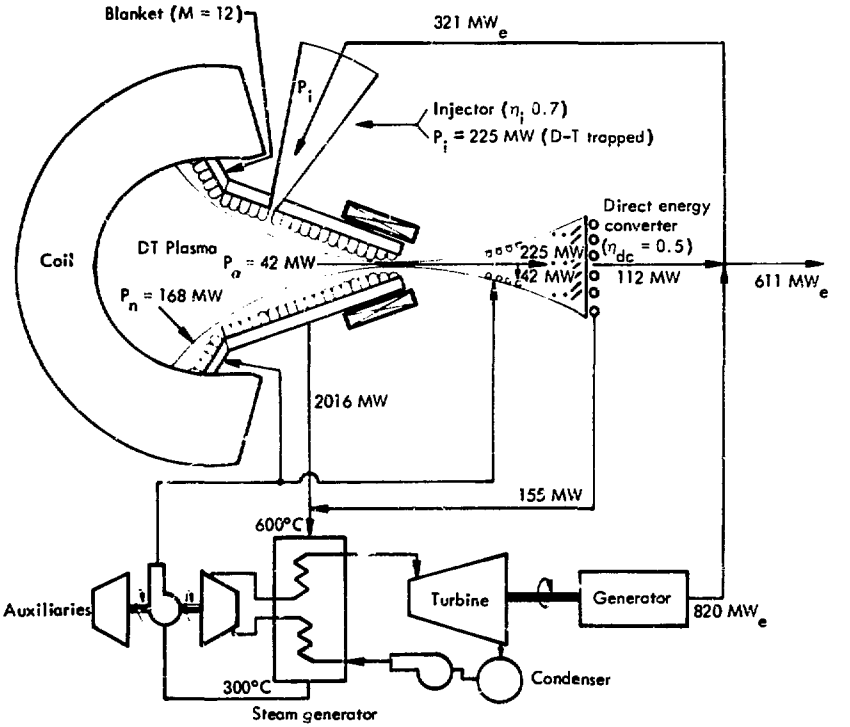

Fig. 2-5. Major components and power flow of the 600-MW_e, 700-kg(Pu)/year, mirror fusion, fast-fission, hybrid reactor.

have shown that, on the average, a 14-MeV neutron causes ~1.5 fissions in a thick assembly of pure natural uranium; ~80% is ^{238}U fission. In addition to the 300 MeV produced, ~4 additional neutrons are produced by fission and other processes, and these neutrons can be used to produce fissile and fusile fuel. Obviously, a pure uranium system is not possible because a blanket in a reactor must contain structure, a tritium-breeding material, and other materials that will degrade performance. The specific fast-fission blanket and fuel management scheme developed for this study produces per 14-MeV neutron an average of 160 MeV, 0.9 atoms of ^{239}Pu, and 1.2 tritium atoms. At a fusion power of 210 MW_t (neutron power of 168 MW_t), the average blanket power is 2000 MW_t, and the net ^{239}Pu production is 690 kg/year.

A fast fission blanket gives, by a factor of 2, a higher yield of fissile fuel per

fusion reaction than any other design known to us. Our present design is a factor of 10 more productive than our previous thermal blanket design.[2-1] Our previous design, by contrast, emphasized power generation and resulted in 0.3 atoms of fissile fuel and 560 MeV per fusion reaction. That design employed a thermal blanket, slightly enriched in ^{235}U; however, it was incomplete in that it did not contain the necessary structure needed to contain the pressurized helium coolant.

An estimate of the cost is given in Table 2-1. This cost estimate is based on a first-cut, unoptimized design. The total capital cost of $1.2 billion with 600-$MW_e$ power production and 700 kg of ^{239}Pu per year gives a capitalization of $2000/$kW_e$ or $1700/g of Pu/year. We realize that this price is probably too high to be competitive, but we are encouraged that our first cut at a complete design is only a factor of 2 to 3 away from being competitive. For the economic analysis, we take a charge for the use of capital of 14% and a plant duty factor of 80%. To recover this capital cost, we consider the sale of both electricity and ^{239}Pu. Cost could be recovered, for example, if ^{239}Pu is sold for $20/g, and electricity is sold for 40 mills/kWh; or, alternately, if electricity is sold for

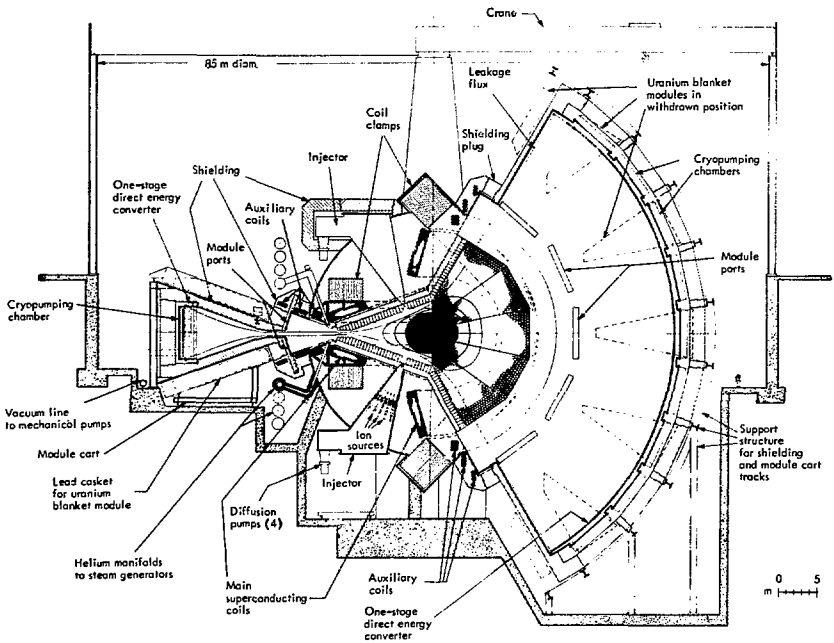

Fig. 2-6. Vertical cross section through reactor.

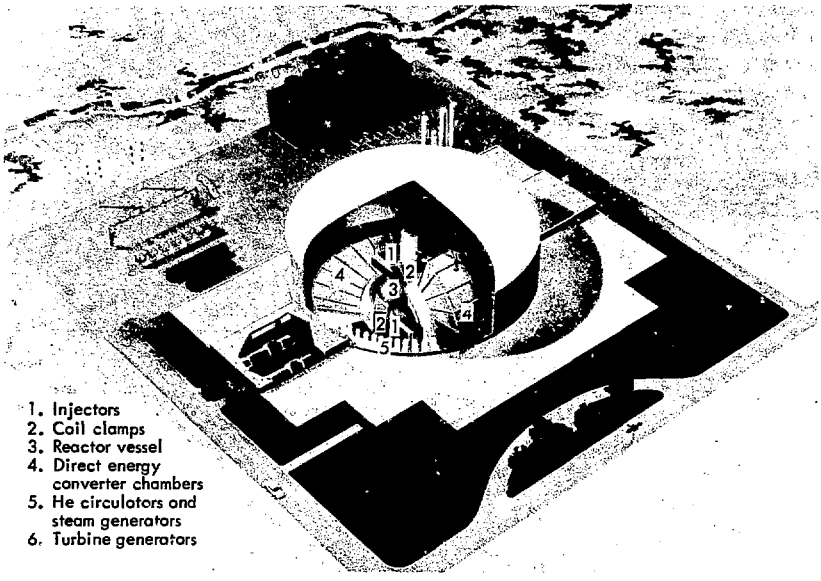

Fig. 2-7. Artist's conception of power plant.

20 mills/kWh, and ^{239}Pu is sold for $140/g. We think it may be possible to halve the unit capital cost by increasing the power and improving the design, thus considerably improving the economic outlook (~22 mills/kWh and $20/g are perhaps attainable). The possible tradeoffs are compared in Fig. 2-8.

The important question of safety in the event of an accident that could release radioactive elements has been studied only briefly. Since it is impossible for the system to experience a nuclear excursion ($k_{eff} < 0.5$ while criticality occurs at $k_{eff} = 1.0$), the most serious problem is posed by a partial blanket melt due to a loss of coolant flow. We have assumed redundancies in the coolant paths and emergency helium circulators so that the probability of a partial core melt will be very small. Redundant containment systems are also assumed. This is an area needing much more attention.

Table 2-2 gives some of the parameters of our design. To give our design some perspective, we have listed in Table 2-3 some of the advantages and disadvantages of our design. Table 2-4 gives some possible scaled parameters for essentially the same design; however, with the magnetic field increased and the injection power doubled, the fusion plasma would put out twice the power. The capital cost per kW is then much more competitive.

If the fusion plasma should have losses twice those expected, due, for example, to microinstabilities, then a fusion-fission

hybrid with a higher-multiplication blanket still might be interesting. We illustrate this high-multiplication blanket, low fusion-plasma performance case by the example parameters in Table 2-5, where we use the plasma components extrapolated from our present design and the neutronic performance of a thermal-lattice blanket (see Refs. 2-2 and 2-3 for examples of the thermal lattice).

Combining the thermal-lattice blanket with classical plasma confinement results in the projected performance and cost parameters given in Table 2-6. The only differences between this extrapolated 'design' and the point design are the use

Table 2-1. Cost summary.

Item		Millions of $[a]	
Nuclear island:			
Magnet	302		
Injectors	45		
Blanket	40		
Shielding	77		
Direct energy converter	24		
Vacuum system	27		
Tritium system	70		
Diagnostics	1		
Plasma start-up equipment	2		
Total nuclear island construction (A)		588	
Engineering, 2.5% of (A)		15	
Contingency, 20% of (A)		118	
Total nuclear island:			720
Thermal system:			
Helium cooling system	16		
Steam system	122		
Electrical substation	13		
Cooling water system	12		
Controls and instrumentation	3		
Total thermal conversion system constr. (B)		165	
Engineering, 5.6% of (B)		9	
Contingency, 3% of (B)		5	
Total thermal conversion system:			180
Building, facilities, and site construction (C):		39	
Architect, engineering, 11% of (C)		4	
contingency, 5% of (C)		2	
Total building, facilities & site:			45
Temporary facilities, 0.4% of (A)+(B)+(C)			3
Other costs (taxes, insurance, training, start-up, administration, licensing, etc.) 3.6% of (A)+(B)+(C)			29
Total (D):			976
Interest during construction, 24% of (D)			234
Total plant cost:			1,211

[a] 1975 dollars.

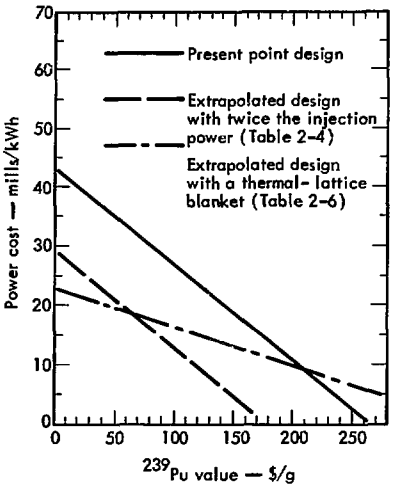

Fig. 2-8. Electric power cost vs Pu value.

of the high-energy multiplying thermal-lattice blanket in place of the lower-multiplying fast-fission blanket, and an increase in the size of the thermal system needed to handle the increased blanket power. While we have not examined the implications of using the thermal-lattice blanket, we expect that the uncertainties in such an extrapolation of our point design are less than those associated with the doubling of the injection and plasma power (Table 2-4).

The estimated economic performances of these design extrapolations (from Tables 2-4 and 2-6) are compared with that of the point design in Fig. 2-8. These extrapolations suggest a few of the directions we can take to improve our mirror hybrid reactor design.

We think the mirror hybrid fusion-fission reactor is sufficiently interesting that further work should be done. For example, handling and shielding of the modules and monitoring tritium in high ambient radiation fields will both require attention. Work should be directed towards decreasing capital cost and maximizing the safety while using the least extrapolation from present-day technology — a tall order!

REFERENCES

2-1. W. C. Wolkenhauer, B. R. Leonard, Jr., A. M. Sutey, and R. W. Moir, "Conceptual Design of a Fusion-Fission Hybrid Reactor Based on a Mirror Fusion Reactor with a Subcritical Gas Cooled Fission Blanket," in Proc. First Topical Meeting on the Technology of Controlled Nuclear Fusion, 1974 (San Diego, 1974), CONF-740402-P1, vol. 1, p. 238.

2-2. B. R. Leonard, Jr. and W. C. Wolkenhauer, "Fusion-Fission Hybrids: A Subcritical Thermal Fission Lattice for a DT Reactor," Proc. Conf. on Technology of Controlled Thermonuclear Fission, 1972 (Univ. of Texas, 1972); also, Pacific Northwest Laboratories Rept. BNWL-SA-4390 (1972).

2-3. J. A. Maniscalo and L. L. Wood, Advanced Concepts in Fusion-Fission Hybrid Reactors, Lawrence Livermore Laboratory Rept. UCRL-75835 (1974).

Table 2-2. Fusion-fission reactor parameters.

Reactor:	
Power	2060 MW_t 610 MW_e
Efficiency	30%
Fuel production	690 kg(Pu)/yr average over 30-yr plant life 11.2 kg(tritium)/yr (9.3 kg of tritium consumed per year)
Material inventory	1.03×10^6 kg of natural uranium 4.1 kg of tritium 1.13×10^4 kg of ^6Li 1300 kg of helium in coolant system 4400 kg of helium in cryogenic system
Total cost	$\$1.2 \times 10^9$ or \$2000/kW_e
Cost of electricity	(selling Pu at \$20/g) 40 mills kWh)
Cost of Pu produced	(selling electricity at 20 mills/kWh) \$140/g
Plasma:	
Length, L	25 m
Radius, r_p	3.5 m
Mirror field, B_m	6.8 T
Peak field in the conductor, $B_{conductor}$	8.1 T
Vacuum central field, B_{vac}	1.94 T
Vacuum mirror ratio, R_{vac}	3.5
Mirror ratio, R	7.8
Plasma pressure/field pressure, β	0.80
Density × containment time, $(\overline{n\tau})$	2.7×10^{13} $cm^{-3} \cdot s$
Fusion power/injected energy, Q	0.935
$(\sigma v)_{DT}$	9.2×10^{-16} cm^3/s
Peak density, n_0	5.85×10^{13} cm^{-3}
Peak power density, $(\frac{P}{V})_0$	2.2 W/cm^3
Fusion power, P_F	210 MW
Mean energy, $\overline{W}$	117 keV
Ambipolar potential, $\phi_{ambipolar}$	54 kV
Injector:	
η_i	70%
Injection energy (D), $W_{in,D}$	100 keV
Injection energy (T), $W_{in,T}$	150 keV
Injected D^0 current, I_{D0}	1270 A (trapped)
Injected T^0 current, I_{T0}	630 A (trapped)
Trapping fraction	0.94
Beam direct converter efficiency	71%
$P_{D0} + P_{T0}$	225 MW
Cost	\$47 million or \$210/kW (trapped power)
Direct energy converter:	
Type	one-stage
Efficiency	50%
Thermal bottoming cycle	35%
Power out	112 MW
Cost	\$25 million or $\$225/kW_{out}$
Blanket:	
Average energy multiplication, M_{ave}	12
Peak power density in fuel	100 W/cm^3 at startup (~300 W/cm^3 at equilibrium)
Peak-to-average fuel power density at startup	~5 to 1
Peak-to-average fuel power density at equilibrium	~10 to 1
Total thermal power	2000 MW_t
Inlet helium temperature	300°C
Outlet helium temperature	600°C
Net fissile-fuel production	690 kg/yr (assuming an 80% duty factor)

Table 2-3. Advantages and disadvantages of the fusion-fission reactor.

Advantages	Disadvantages
Fusion-fission reactors in general:	
Large energy multiplication in blanket.	Radioactive fission products.
Fissile fuel production (^{239}Pu and/or ^{233}U).	Tritium handling.
Subcritical (cannot have a nuclear excursion).	Physically very large components.
Reduced performance required of fusion components relative to pure fusion, e.g., reduced first-wall loading, reduced Q required, reduced injection, and efficient direct energy conversion.	Relatively high capital cost.
	Complex geometry.
Low magnetic field (< 80 kG).	
Fissile fuel not required. The blanket can be fueled with natural or depleted uranium or spent light-water reactor fuel. Long-lived fission reactor actinide wastes could be "burnt."	
Mirror confinement for the fusion component of a fusion-fission reactor:	
Nearly spherical shape for neutron source.	Low Q ($Q = P_{fusion}/P_{injected}$).
Access for removal of blanket modules.	Sensitivity to enhanced losses.
Access for neutral beam injection.	Complicated magnet.
No known impurity problems.	
Steady-state operation.	
Problems with present reference design:	
Unit costs ($/kW and/or $/g fissile fuel per year) are high.	
High peak-to-average blanket power density (~5 to 1 at start up; ~10 to 1 at equilibrium).	
Average blanket power density too low.	
Power output increases with time (360 MW_e at start up; 740 MW_e at equilibrium).	
Blanket modules are large (~10^5 kg).	

Table 2-4. Parameters for a high-power fast-fission-blanket reactor.

Power	1200 MW_e (all powers are double the reference design)
Blanket multiplication, M	12
Q	0.935
Fuel production	1380 kG/year
Total cost[a]	$\$1.6 \times 10^9$ or $\$1300/kW_e$
Cost of electricity	(selling fuel at $20/g) 26 mills/kWh
Cost of fuel	(selling electricity at 20 mills/kWh) $55/g

[a]The magnet was assumed to have a lower cost structure than before by $100 million, but otherwise the magnet scales as fusion power, $\sqrt{P}$, resulting in a magnet cost of $280 million. The mirror ratio must be dropped slightly to keep the peak field within the limits of Nb T. .luctor technology.

Table 2-5. Parameters of hybrid reactor with lower Q and higher M than the reference design.

Departure from point design[a]:	
Q	$1/2 \times Q_{classical} = 0.47$
Injected power, P_{in}	$2 \times P'_{in} = 450$ MW
Blanket multiplication, M	$2 \times M' = 24$ (thermal lattice)
Net fissile breeding ratio	0.80 · (NFBR) = 0.7 atom/fusion
System performance:	
P_e (net)	1200 MW_e
η(net)	0.30
Fissile production (net)	550 kG/year
Plant cost (extrapolated)	$\$1.50 \times 10^9$
Cost of electricity (if ^{239}Pu is sold at \$20/g)	27.5 mills/kWh
Cost of ^{239}Pu (if electricity is sold at 20 mills/kWh)	\$137/g

[a]Where primed quantities are the reference values.

Table 2-6. Parameters of hybrid reactor with classical Q (0.935) and higher M than the reference design.

Departure from point design:	
M	24
Net fissile breeding ratio	0.7 atom/fusion
System performance:	
P_e (net)	1375 MW
η (net)	0.34
Fissile production	550 kg ^{239}Pu/year
Plant cost	1.32×10^9
Cost of electricity (if ^{239}Pu is sold at \$20/g	22 mills/kWh
Cost of ^{239}Pu (if electricity is sold at 20 mills/kWh)	\$47/g

3. General Description of Reactor and Facilities

The reactor and its associated facilities consist of the following main components and systems:

- The main superconducting coils that generate the magnetic mirror field for the confinement of the plasma in which the fusion reactions take place.
- The coil supports that restrain the main coils from distorting under the enormous forces generated by the magnetic field.
- The auxiliary superconducting coils that control the shape of the leakage flux from the plasma.

- The injectors that supply the fuel (deuterium and tritium) to the plasma.
- The uranium blanket that surrounds the plasma and in which the fission reactions take place. The power generated by the fusion reactions in the plasma is multiplied by the fission reactions in the blanket. This blanket also contains lithium for breeding tritium to feed the injectors. The blanket is divided into modules to facilitate removal and recharging.
- The helium cooling system that transfers the heat from the uranium blanket to the steam generators.
- A thermal power system that converts the thermal power from the steam generators into useful electrical power via conventional steam turbines and electrical generators.
- The direct energy converters that turn the leakage flux from the plasma directly into electrical current.
- The direct energy converter electrical system that collects the current from the direct energy converters and produces useful electrical power.
- A vacuum envelope that surrounds the main coils, the plasma, the uranium blanket, the direct energy converters, and the injectors.
- Vacuum pumping systems that remove gas from the plasma space, the injectors, and the direct energy converters.
- Systems that include a tritium handling system, a fuel-recovery system, a purification and isotopic separation system, and tritium containment inventory and storage.
- Shielding that
  Reduces neutron heating in the superconducting coils.
  Reduces neutron damage to the superconducting coils.
  Provides biological protection.
- Remote handling systems that facilitate
  Removing and recharging the uranium blanket modules.
  Servicing the injectors and other elements of the machine.
- A building that houses the reactor and its associated facilities.

MAIN SUPERCONDUCTING COILS

The Yin-Yang coil configuration shown in Fig. 2-1 is really a variation of the familiar "Baseball" design (where the shape of the coil is similar to the seam of a baseball) that has been used in a number of mirror devices. The Yin-Yang arrangement results if the conductors of a baseball coil are divided into two bundles, identical, but rotated 90° to each other. In fact, the halves of the reactor are rotated 90°. The Yin-Yang arrangement provides space between the coils for the four injectors and permits easy removal of the blanket.

The individual superconductors are fine filaments of Nb Ti embedded in 1-cm square copper bars. Suitable spacers between the copper bars provide passages for the liquid-helium coolant. The windings are housed in a stout, stainless steel coil tank that must be enclosed in a suitable thermal shield consisting of a liquid-nitrogen-cooled copper plate and a multilayered reflective heat shield (not shown in the drawings).

Details of the magnetic design of the coils and the refrigeration calculations are discussed in Section 7.

COIL SUPPORTS

Enormous forces are produced by the coils. One component, which tends to straighten out the arc of the coil, can be resisted by the coil tank itself; the other component tends to open up the coil gap.

Because it is impractical to make the coil tank strong enough to contain the coils, massive clamps are provided. These clamps consist of a large number of truss subassemblies, fabricated from non-magnetic stainless steel and laminated together. The coil clamps are cooled to the same temperature as the coils. Therefore, these members must be surrounded by the same type of thermal shield as the coil. If the clamps were not cooled along with the coils, there would be differential thermal contraction, and large forces would be transmitted across thermal barriers. The computations for the clamps are shown in Section 7.

The total weight of these clamps is on the order of 15,000 tons, and their cost appears to be disproportionately large. We therefore feel that, while this is one possible solution, other ideas must be studied. This particular design was based on the requirement that the coil gap be kept completely open. If we back off somewhat from this requirement, we might largely replace the clamps with water-cooled tension members.

AUXILIARY SUPERCONDUCTING COILS

With the main coils alone, the magnetic flux lines would start to expand outwardly as soon as they emerged from the coil gap. The leakage plasma would, of course, expand along with the magnetic flux lines and would then strike the vacuum gates for the blanket modules. To avoid this, and to lead the leakage plasma into the direct energy converters, auxiliary coils must be added.

The auxiliary coils are superconducting coils of the same general construction as the main coils. The coils also must be surrounded with shielding.

The magnetic design of the auxiliary coils is discussed in Section 7.

INJECTORS

With a mirror configuration utilizing Yin-Yang coils, it is possible to introduce high-energy neutrals into the reactor via four separate injectors. Each injector is roughly pyramidal in shape with a rectangular base and apex angles of 30° and 60°, and each holds 70 modified Berkeley sources mounted in five columns of 14 units each. Each injector is located in a large pumping chamber serviced by four 120-cm Hg ejector pumps. All of the beams pass through a 20- by 50-cm opening in the blanket.

The beams coming from each column of 14 sources go into a common liquid-nitrogen cooled neutralizer, about 1-m long, and subsequently pass between electrodes that recover the energy of that portion of the beam that was not neutralized. A cryogenic panel mounted on each side of the column pumps away the unwanted neutral gas and also provides magnetic shielding. By providing adequate pumping capacity, continuous operation is possible; i.e., each cryopanel can be removed from service (by sliding it between the columns of sources into the pumping chamber), outgassed, and subsequently reintroduced into the injector.

URANIUM BLANKET

The gross blanket geometry is defined by the plasma and coil geometries for a minimum-B Yin-Yang magnetic mirror. The blanket design, shown schematically in Fig. 2-4, is constructed from pie-shaped modules whose assembled geometry conforms to the Yin-Yang magnetic field. Each module, in turn, is composed of a collection of domed, cylindrical, pressure vessels (submodules) mounted to the module base.

The submodule, the basic component of the blanket, contains an inner fast-fission zone and an outer tritium-breeding zone. The inner contains natural uranium carbide contained in wire-wrapped pins in a hexagonal array. The outer zone contains lithium aluminate. Helium coolant is supplied to, and removed from, the submodule by plena in the module base. The helium flow within the submodule first cools the pressure vessel wall and then removes the heat from the fuel pins and the heat and tritium from the breeding material.

A new blanket starts life with natural uranium fuel and has an energy multiplication (M) of 8, a net fissile breeding ratio (NFBR) of 1.2 atoms/fusion, and a tritium breeding ratio (T) of 1.05. As the blanket is exposed, it will enrich itself in plutonium, thereby causing M and T to increase and NFBR to decrease. With the refueling scheme used, the life time average M, T, and NFBR are 12, 1.2, and 0.9.

HELIUM COOLING SYSTEM

The heat from the uranium blanket is transferred to the steam generators by helium. To ensure safety, the entire system is duplicated: there are two inlets and two outlets on each blanket module; two inlet manifolds and two outlet manifolds are provided for each side of the reactor; a helium circulator is provided in each circuit; and in addition, the helium is everywhere enclosed by two walls. While in the module, the helium is enclosed, of course, by the module itself, but it is also enclosed by the vacuum envelope surrounding the entire reactor. All helium lines to and from the reactor are double-walled. Likewise, within the steam generators the helium is again doubly enclosed.

Each of the helium circulators (Fig. 3-1) consists of a helium compressor with a steam turbine main drive and a water turbine (Pelton wheel) auxiliary drive. The latter supplies power to the circulators when steam supply is not available. This arrangement is similar to that used in General Atomic's Fort St. Vrain, Colorado, helium-cooled fission reactor.

An auxiliary after-heat cooling system, also using helium, cools the modules while they are being withdrawn and transported for processing. A value in the main cooling line at each module makes the module gas-tight during removal and transport.

See Section 8 for calculations on the helium cooling system.

THERMAL POWER SYSTEM

The thermal power system converts the thermal power from the steam generators into useful electrical power. Because we have studied this aspect of the plant only very superficially, we assume

that this system employs conventional steam generators, steam turbines, and electrical generators.

We are patterning the thermal power system after that of the General Atomic helium-cooled fission reactor. We employ vertical, steam-generator modules. The hot helium from the reactor flows vertically through the casing, giving up its heat to helically wound water- and steam-tube bundles that surround a central header. The steam generator modules are in the main reactor room (Fig. 3-1), and the turbine and electrical generators are in the adjacent generator room. While Figs. 3-1 and 3-2 show many helium circulators and steam generators, we would actually use from 4 to 6 of each. Figures 3-3 and 3-4 provide additional detail.

DIRECT ENERGY CONVERTERS

The power in the inevitable leakage flux from a mirror reactor may be largely recovered by direct energy converters. The direct energy converter we propose to use here is similar to that described in Ref. 3-1.

As previously described, the auxiliary coils guide the leakage flux into the expander tanks and then into the direct energy converters. The beam of ions is allowed to expand to a peak power density of about 100 W/cm^2. We have shown experimentally that, at this power density,

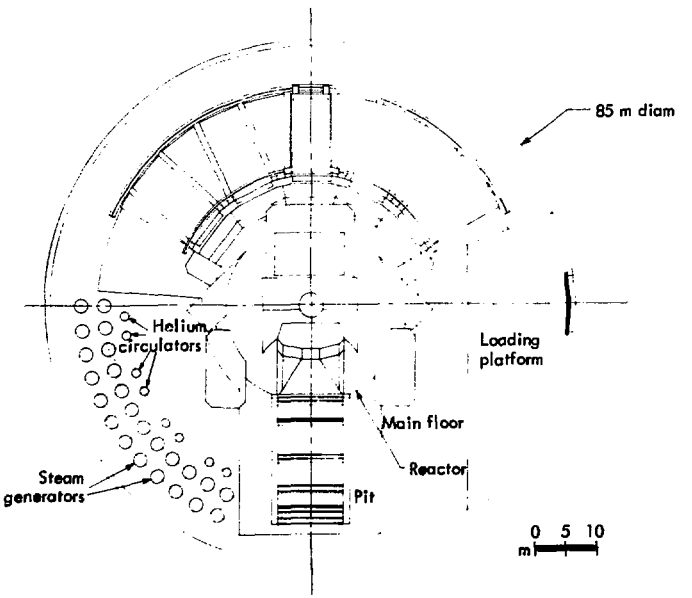

Fig. 3-1. Plan view of reactor in reactor room.

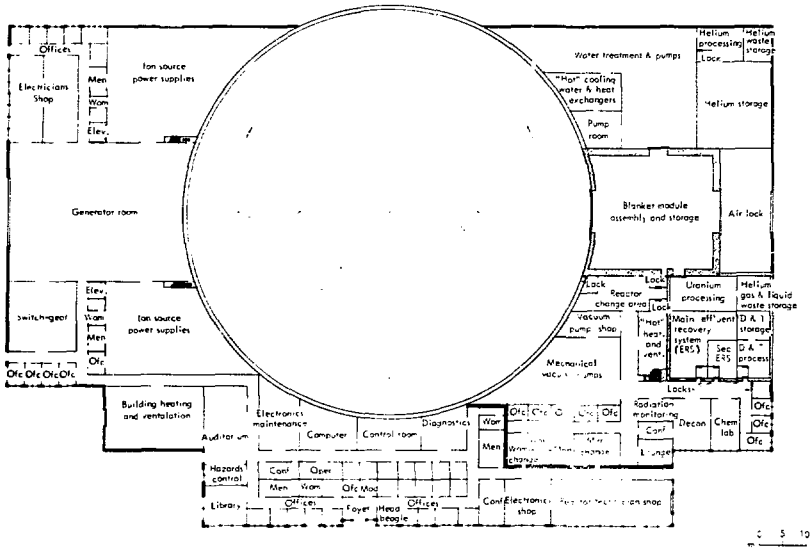

Fig. 3-2. Plan view of main floor of building.

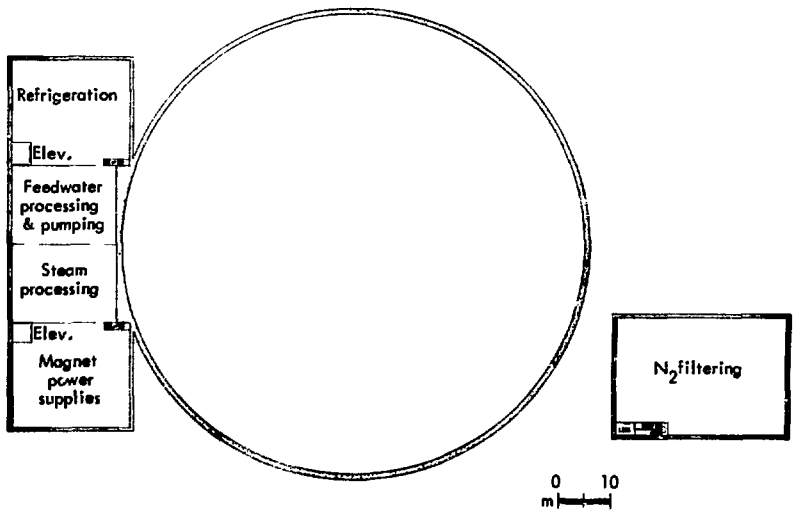

Fig. 3-3. Plan view of building basement.

the elements of the direct energy converter may be cooled by direct radiation. The converter we show in this report (see Fig. 8-1) is single-stage and employs a pair of wire grids followed by a ribbon grid. The wire grids reflect the electrons and allow the positively charged ions to continue on through; the ribbon grid acts as an ion trap. Thus, the particles see the first wire grid at zero potential, the second wire grid at negative potential, and the ribbon grid at high positive potential. The wires and ribbons are cooled by radiation to helium-cooled tubes that line on the expander tank.

When the ions are neutralized, the large quantity of gas that is produced is pumped by cryopumping chambe behind the ribbon grid. The ribbon grid is opaque to the ions, but presents only a modest impedance to the neutral gas.

ELECTRICAL SYSTEM FOR THE DIRECT ENERGY CONVERTER

Through a system of grids and ribbons resembling a venetian blind (see Fig. 2-6), the direct energy converter reclaims the energy lost by the reactor through leakage of charged particles.

To initiate the collection pro ess, the potentials of the grids and ribbons must be accurately established. These potentials are supplied by an inverter-rectifier power supply arrangement, where (in the rectifier mode) appropriate voltages are applied to the grids and ribbons. Once the potentials are established and the collection process begins, the recovered electrical energy can be used. In some cases, all of the power from the direct energy converter will be used by the accel grids in the ion source.

The phasing of the inverters and rectifiers is controlled by an electronic regulator

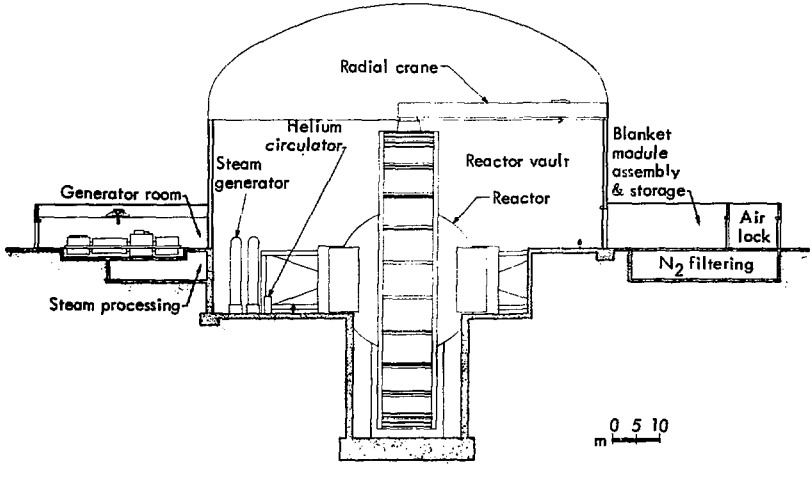

Fig. 3-4. Sectional elevation of building.

system that accurately maintains the potential on the venetian blind electrodes. Because the voltage required for the ion-sources does not always match the output voltage of the direct energy converter, small series-topping power supplies are provided to obtain the precise ion source voltages.

VACUUM ENVELOPE

The entire reactor, including the direct energy converters, is enclosed in a vacuum envelope. This envelope has a conventional, welded construction. Other than the flange joints provided for the removal of the cryopumping chambers and for access to the direct converters, no joints are provided for major dismantling. The tank would be simply welded in place and expected to remain there for the life of the machine.

The spherical portion of the tank surrounding the reactor proper is supported internally by the shielding and the magnet structure. The expander tanks, however, require external supports to resist the atmospheric loading. This external stiffening structure also supports both the shielding around the expander tanks and the tracks for the blanket module trucks. As proposed, the external structure consists of radial members connected at their inner ends to the spherical tank. At their outer ends, each pair of radial members is supported by a column. At their ends, these columns are connected together by a box-beam that is curved in a circular arc to conform to the shape of the expander tank.

VACUUM PUMPING SYSTEMS

The large volume of gas produced at the direct energy converters is pumped by cryopumping chambers behind the ribbon grids. These cryopumping chambers contain liquid-helium-cooled panels that are thermally shielded with liquid-nitrogen-cooled panels and multiple, reflective, heat shields. Any one panel may be isolated in automatic sequence for "defrosting" by means of a "Jalousie" louvred valve. The cryopumping panels may then be warmed up and the evolved gas collected through a mechanically pumped vacuum manifold.

To maintain a good vacuum in the plasma area, additional cryopumping panels may be introduced into the intermediate volume formed by the constriction between the coils and the entrance to the expander tank. See Section 8 for pumping calculations.

The large quantity of gas also produced in the injectors is pumped by a combination of cryopumping and conventional diffusion pumps. See Section 6 for further details.

TRITIUM-HANDLING SYSTEM

The tritium-handling system is divided into two primary systems: a helium-coolant, tritium-recovery system and a purification and isotopic-separation system. If tritium is accidentally released, the gas will be contained by secondary purifiers that will remove tritium from the room atmospheres and by special design features in the containment structure.

Fuel Recovery System

Helium coolant will carry tritium picked up during passage through the blanket. Of the hot helium-coolant flow, 1% is directed to the tritium recovery system.

Traces of water are removed by a regenerative heat exchanger and cold trap operating at liquid-nitrogen temperature. The coolant is reheated in the same heat exchanger and then continues to a vanadium diffuser. Here the helium passes through an array of vanadium tubes, while the tritium diffuses through the vanadium. The tritium is recovered from an outer chamber by a pumping system and can either be sent directly to the injectors or stored elsewhere.

Details are discussed in Section 10.

Purification and Isotopic Separation System

Tritium and deuterium recovered from the vacuum pumping systems must be purified and isotopically separated before being returned to the injectors. The gas is purified by passing it through a palladium diffuser. Cryogenic distillation columns then separate the gas into tritium and deuterium streams which are reinjected immediately. The components of this system are similar to those used in the FERF design.

These components and appropriate pumping systems are described in Section 10.

Tritium Containment, Inventory, and Storage

Rooms containing components with large amounts of tritium will be sealed with a nitrogen atmosphere. In case of an accidental release within the room, a purifier will catalytically oxidize the tritium and hold it on molecular sieve beds. This equipment follows the FERF design.

Tritium can also slowly permeate the outer walls, which have very large surface areas. We are proposing a new "getter wall" that can be readily adapted to a variety of situations. In this method, a structural wall is coated on the outside with a getter that forms stable hydrides. The getter is, in turn, covered with a protective outer layer. The getter operates at ambient temperature and need hold only the small amount of tritium that permeates the structural wall.

Containment details are given in Section 10.

SHIELDING

Shielding is required

- To reduce neutron heating within the superconducting coils,
- To reduce neutron damage to the superconducting coils, and
- To provide biological protection against induced radioactivity and prompt radiation.

The coil shield consists of a layer of Boral* (not shown) placed immediately outside the coil thermal shield to absorb neutrons. Boral produces alpha particles rather than more penetrating gamma rays. Next is a layer of lead to capture gamma rays. Outside of this is the main bulk of the shielding: this main shielding consists

*"Reference to a company or product name does not imply approval or recommendation of the product by the University of California or the U.S. Energy Research & Development Administration to the exclusion of others that may be suitable."

of stainless steel and water placed adjacent to the coils and immediately outside the uranium blanket. The layer of shielding immediately within the spherical vacuum tank is of concrete encapsulated in stainless steel tanks.

To prevent the escape of radiation through the injectors and through the direct energy converters, additional shielding is provided immediately outside the vacuum envelope.

REMOTE HANDLING SYSTEMS

Means must be provided for removing and loading the uranium blanket modules and for servicing the injectors, direct energy converters, and other elements of the reactor.

During shutdown, the shielding shown (Fig. 2-6) should provide sufficient biological protection so that the reactor room may be entered as long as all parts of the shielding are in place. However, because of the tritium contamination that may result when the reactor has been opened (e.g., for replacement of ion sources), operating personnel must wear protective, airtight suits with separate air supplies. When any part of the shielding is removed, the resulting radiation level (at least in the immediate vicinity of the opening), will be such that operating personnel must be excluded. Therefore, remote manipulation will be required for all operations involving opening the shielding. The shielding design requires far more study.

The general arrangement of the uranium blanket modules is shown in Figs. 2-1 and 2-4. The wedge-shaped modules are arranged in a radial array, as in the sections of a pie. Each module is provided with stationary tracks that support it and along which it may be rolled. Opposing pairs of modules cross each others paths as they are withdrawn. The vacuum envelope for each module has a port with a vacuum-tight gate. A removable plug is provided in the shielding for each port. When a module is withdrawn, a set of temporary tracks must be inserted to bridge the gap between the permanent tracks and the port.

Because a spent, withdrawn module is, of course, very radioactive, it must be placed in a lead casket. These caskets are mounted on carts that run on tracks placed on either side of each expander tank. A temporary cooling system removes the after-heat from the module during transportation.

The sequence of operations for the removal of a module is as follows (see Fig. 3-5):

1. Remove the shielding plug.
2. Open the vacuum gate.
3. Put the temporary tracks in place.
4. Attach the temporary cooling lines to the module.
5. Close the main helium valves at the module
6. Separate the joints at the module in the main cooling lines.
7. Roll the module into the casket.
8. Run the cart to a position where the casket may be handled by the overhead crane.
9. Take the casket, by crane, to the loading platform.

To load a fresh module into the blanket, reverse this process. Remotely operated means are provided for servicing the injectors, direct energy converters, and other elements of the reactor.

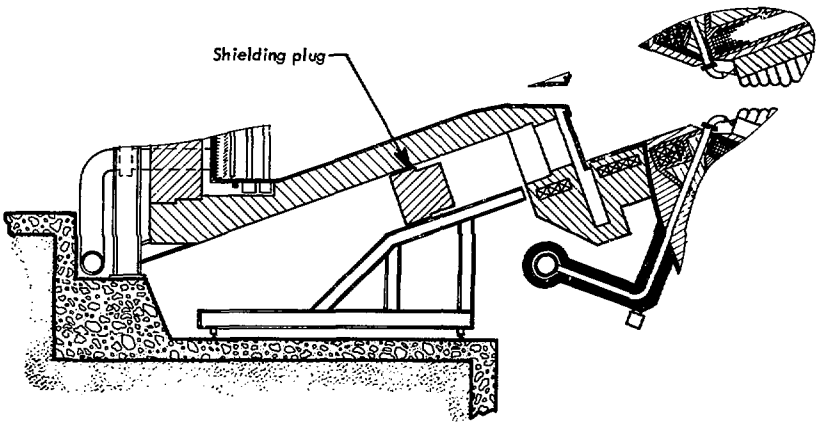

Fig. 3-5(a)

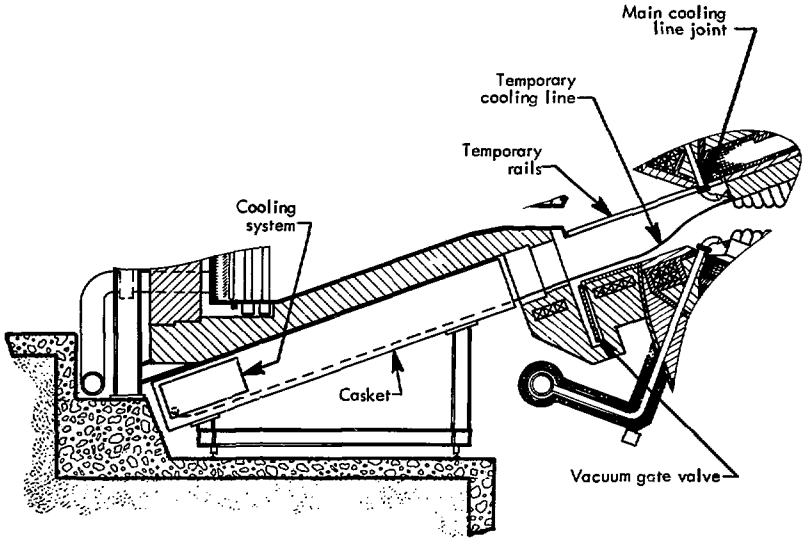

Fig. 3-5(b)

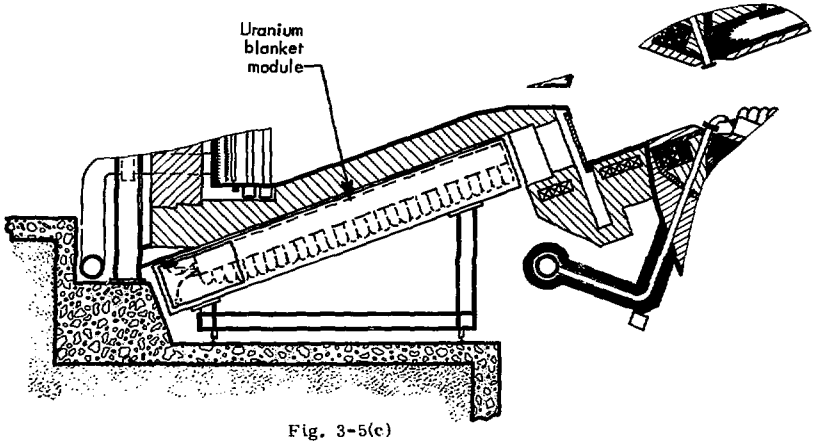

Fig. 3-5(c)

Fig. 3-5. Module removal sequence:
(a) Tritium shielding plug removed; (b) Casket in place, vacuum gate valve opened, temporary rails and cooling line attached; (c) Module in casket.

BUILDING AND UTILITIES

The fusion-fission hybrid reactor building is a highly specialized steel and concrete structure. Its design is integrated with the design of the reactor systems, the blanket module assembly, the disassembly facilities, the tritium handling systems, and the power generation facility.

Building Functions

The building will provide

- Shelter space for the reactor and allied equipment (including maintenance and operating equipment).
- Radioactive contamination control and protection of personnel from excessive amounts of radiation.
- A containment vault that will retain released radioactive materials and gases coming from the reactor or its equipment.
- Facilities for the safe collection and disposal of tritium and contaminated wastes so that the hazard to personnel operating the facility will be minimized.
- Work areas for assembly of uranium blanket modules and for storage.
- Tritium recovery and storage facilities.
- Steam turbine power generation facilities.
- Utilities, office space, and shops as required to meet the minimum need of operation and maintenance.

Description of Principal Areas

Building plans, sections, and elevations are shown in Figs. 3-1 through 3-4.

Reactor Containment Vault

The reactor containment vault provides a housing for the reactor and a gas-tight vessel for any radioactivity or particles released in the event of an accident. The vault is constructed of steel with walls and roof approximately 1-1/2 in. thick. Inside, the vault is 280 ft in diameter and 218 ft high. To assure gas-tight integrity, all ducts which penetrate the vault are suitably sealed to the steel vault housing. Also, all cables or pipes within these ducts are sealed or otherwise closed in a positive manner to assure that the vault is leak-tight. The reactor vault is designed to withstand a positive pressure of 2 psi above atmospheric; however, it is normally operated at a negative pressure.

A vertical, hydraulically operated, gas-tight shielding door provides equipment access at the side of the vault. Personnel enter and leave the vault via an air lock that leads from a limited-access area.

A 200-ton radial crane with a shielded control cab covers the entire vault area and is used to assemble and disassemble the reactor.

The reactor vault is operated at a negative pressure and contains an inert gas such as nitrogen. To remove radioactive contamination, this inert atmosphere is continuously circulated through high-efficiency filters. A leak test is performed periodically to assure that there are neither leaks nor penetrations in the structure. For this test, the vault is pressurized to about 2 psi and the leak rate is determined over a 24-h period.

Blanket Module Assembly and Storage Area

At one side of the reactor vault, a reinforced-concrete extension forms a shielded area for assembly and disassembly

of the blanket modules. The radioactive blanket modules are transferred from the reactor vault through the shielding door by truck or dolly. A sliding, shielding door communicates with an air lock that provides the means for removing parts from the area without compromising the atmosphere of the assembly area. A personnel air lock connects the assembly area with the limited-access area.

Generator Room

A 110-ft wide, 140-ft long, 30-ft high room houses two 500-MVA steam turbine generators. This room is adjacent to the steam generators located in the reactor vault. Located under the generators is the steam processing equipment.

Administration and Control Area

The administration and control wing, a single-story structure of approximately 87,500 ft^2, contains the following:

- Reactor control room. Here is space for operation consoles, computer terminals, and closed-circuit television monitors for viewing various parts of the reactor system.
- Computer room. Computer and associated equipment are housed here.
- Diagnostics room. The remote data collecting and counting equipment are housed here.
- Small assembly and maintenance shops.
- Offices.
- Library.
- Auditorium.
- Conference rooms.
- Electronic maintenance shop. This shop provides facilities for maintaining the computer, control, and diagnostics equipment.
- Toilet facilities.
- Lobby.

Power Supply Areas

Rooms on the first floor and basement level house the following electrical equipment and power supplies:

- Emergency generator.
- 400-Hz alternator for ion source filaments.
- Power supplies for the magnet.
- Power supplies for ion sources.
- Distribution switchgear.

In general, all power supplies will be water-cooled to minimize the ventilation requirements in these areas.

Mechanical Equipment Areas

There are two mechanical equipment areas: a conventional one housing equipment for building heating, ventilation, and reactor refrigeration; and second, limited-access area housing potentially radioactive equipment that includes the following:

- Mechanical vacuum pumps.
- Fluid heat exchangers and pumps for cooling radioactive components.
- Treatment facilities and pumps for the water coolant.
- Heating and ventilation equipment for the limited-access area.

Limited-Access Area

A limited-access area on the first floor is provided for operations and equipment that are radioactive or potentially radioactive. Entry is through two change areas One group of change rooms contains lockers and clothing bins, toilet and shower facilities, and personnel decontamination and monitoring facilities. Shielding and life-support suits are located

in a second change area that provides entry to the reactor containment vault and the blanket module assembly area.

Much of the space in the limited-access area is used for module maintenance, nitrogen filtering, and tritium recovery and storage.

Cooling Towers

The reactor power that has been dissipated in the heated, low-conductivity cooling water is transferred to the atmosphere. The water is passed through heat exchangers that transfer the heat to a cooling tower. There are six cooling-tower heat-exchanger combinations in the facility, each rated at 350 MW. The total installed capacity is in excess of 2000 MW.

Electrical Substation

The installed power capacity of the fusion-fission hybrid facility substation is 750 MVA. Four 230-kV lines come to the site on two rows of towers. These lines terminate on disconnect switches for isolation and switching. Both of the separate, three-phase transformer banks have three 125-MVA single-phase transformers. One spare standby transformer can be switched into service to replace any defective transformer. The voltage ratings of the transformers are 230 kV to 13.8 kV. Circuit breakers connect each set of transformers to a 13.8-kV bus. A normally open bus tie breaker connects the two 13.8-kV busses.

Outdoor distribution transformers rated at 13.8 kV to 2.4 kV provide power to the large loads such as the refrigerators and water pumps. Other outdoor transformers rated at 13.8 kV to 480 V supply power to 480-V switch-gear that is housed within the building at approximate centers of load and serves major loads. Local, dry, indoor transformers feed panels to supply lighting, communications, alarm equipment, and control.

Two gas-turbine-driven generators provide emergency power. Batteries are provided for switchgear operation, dc lighting, dc instruments, dc safety circuits, and dc-to-ac inverters.

Site Requirements

No specific site has been chosen for the fusion-fission hybrid facility; however, the cost estimate is based on a level site having the following requirements:

- Suitable substrata for massive structures.
- Close proximity to a utility company power grid.
- Adequate pure water supply.
- Easily accessible to supporting industry and to commerce and transportation networks.
- Access roads.

REFERENCE

3-1. W. L. Barr, R. J. Burleigh, W. L. Dexter, R. W. Moir, and R. R. Smith. IEEE Trans. Plasma Physics, PS-2, 2, 71 (1974).

4. Operating Parameters and System Performance

REACTOR POWER FLOW

The average net electric power output of the reactor is P_e = 610 MW. A one-stage direct energy converter that recovers power from the leakage ions with an efficiency η_{DC} = 50% is followed by a bottoming thermal cycle that operates with an efficiency η_{Th2} = 35%. The combined efficiency is 68%. Power carried by the 3.52-MeV fusion-product helium is also recovered at η_{Th2} = 35%. The fast-fission blanket multiplies the fusion neutron power by a factor M = 12, and this increased power is recovered in a thermal cycle at η_{Th1} = 38%.

Figure 4-1 shows the power-flow diagram with an injector efficiency η_i = 70% and with $Q = Q_{classical}$ = 0.935. The entire flow of power is varied in proportion to the injected power P_{in}, with P_e given by:

$$P_e = P_{in}[\eta_{DC} + (1 - \eta_{DC} + 0.2Q)\,\eta_{Th2} + 0.8MQ\eta_{Th1} - 1/\eta_i] \qquad (4\text{-}1)$$

Here, $0.2QP_{in}$ is the power carried by the helium ions. Thus, for P_{in} = 225 MW of neutral beam power injected and trapped, the fusion power yield is $P_F = QP_{in}$ = 210 MW.

INJECTOR POWER FLOW

The 71% injector efficiency results from considering each of the various processes that takes place in the production and trapping of the neutral beam.

Figure 4-2 shows the power flow through the injector system that results in 225 MW of trapped neutral beam. The fraction neutralized, F = 0.55, and the fraction trapped, f_t = 0.94, remain the same for

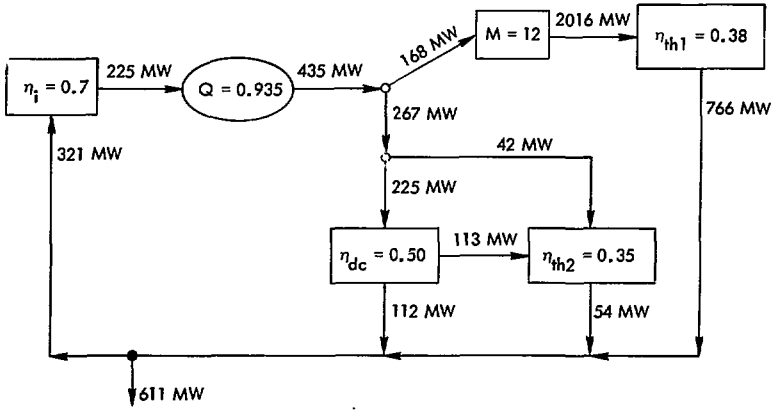

Fig. 4-1. Power flow through the reactor for injector efficiency η_i = 70% (see text for definitions of symbols).

both the 100-keV D^0 and 150-keV T^0 injection because the velocities and cross sections are equal. The efficiencies of the beam direct energy converter, $\eta_{BDC} = 0.69$, and of the two thermal converters, $\eta_{Th1} = 0.38$ and $\eta_{Th2} = 0.35$, also remain the same for both species. $\eta_{BDC} = 0.69$, results from assuming that the expected efficiency of 0.78 can only apply to the 88% of the unneutralized beam that is at the full 100-keV or 150-keV energy. The remaining 12% is at 2/3, 1/2, or 1/3 of full energy and can probably be collected at only a very low efficiency. The efficiency of the positive ion accelerator, $\eta_{acc} = 95\%$, results from using 3.8 keV to create each ion and then losing about 1% in the acceleration process.

Therefore, 320 MW is consumed in injecting 239 MW of beam of which 225 MW is trapped in the plasma. The remaining 14 MW is intercepted by the vacuum wall and is recovered in a thermal cycle.

ELECTRICAL OUTPUT AND FUEL PRODUCTION

The net electric power output is $P_e = 600\ MW_e$. Assuming an 80% plant availability, 480 MW_e-years of electricity is produced. This output power results mostly from fissions in the subcritical blanket as a result of bombardment by 14-MeV neutrons from D-T fusion reactions in the plasma. In addition to power, the neutrons in the blanket also produce ^{239}Pu and tritium.

Of the 11.2 kg/yr of tritium produced, 9.3 kg/yr is used in the neutral beam injectors that maintain the plasma. The 690 kg/yr of plutonium that is generated is salable for fuel used in fission reactors. The rate of production of plutonium can be increased at the expense of a decreased electrical output.

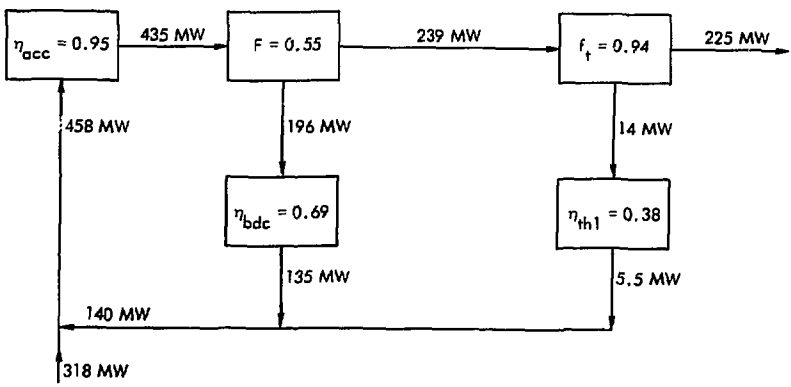

Fig. 4-2. Power flow through the 100-keV D^0 and 150-keV T^0 injector system (see text for definitions of symbols).

5. Plasma Physics Design

PLASMA CONFINEMENT

The physics parameters presented here and listed in Table 5-1 represent a consistent set, although certainly not an optimum set. Optimization will require several more iterations. The design presented here is based on some reasonable but slightly arbitrary choices and a few simplifying assumptions. In Section 12, we discuss the effects of varying these choices and of relaxing these assumptions. The purpose in this section is to present one complete design that can be used as a reference point.

The simplifying assumption having the most serious influence on the design is that the plasma behaves classically (for the effects of nonclassical losses, see Section 12). In particular, we assume that the plasma is magnetohydrodynamically (MHD) stable and that microinstabilities are suppressed to a level where they have a negligible effect on the containment time for the plasma. Containment time is a determining factor in the power gain Q. The effect of a change in containment time (due to microinstabilities, for example) is to produce a corresponding change in Q.

Q is defined as the ratio of the fusion power produced, P_F, to the power injected and trapped, P_{in}; i.e.,

$$Q = \frac{P_F}{P_{in}} . \qquad (5\text{-}1)$$

Table 5-1. Physics parameters.

Distance between mirrors, L	25 m
Plasma radius, r_p	3.5 m
Mirror field, B_m	6.8 T
Vacuum central field, B_{vac}	1.94 T
Vacuum mirror ratio, R_{vac}	3.5
Mirror ratio, R	7.83
Plasma pressure/field pressure, β	0.80
Density × containment time, $(\overline{n\tau})$	2.7×10^{13} s/cm^3
Fusion power/injected power, Q	0.935
Central density, n_0	5.85×10^{13} cm^{-3}
Reaction rate parameter, $(\overline{\sigma v})_{DT}$	9.2×10^{-16} cm^3/s
Fusion power, P_F	210 MW
Mean energy, $\overline{W}$	117 keV
Ambipolar potential, $\theta_{ambipolar}$	54 kV
Power injected and trapped, P_{in}	225 MW
Injected D^0 current, I_{D0}	1270 A
Injected T^0 current, I_{T0}	630 A
Injection energy (D), $W_{in,D}$	100 keV
Injection energy (T), $W_{in,T}$	150 keV

P_F is calculated by integrating the reaction rate over the volume of the plasma and multiplying the result by E_F, the energy released per fusion reaction (E_F = 17.58 MeV*). Thus,

$$P_F = E_F \int n_D n_T \overline{(\sigma v)}_{DT} \, dV \, . \quad (5\text{-}2)$$

We assume that the densities of deuterium and of tritium are equal everywhere ($n_D = n_T = n/2$). The reaction rate parameter, $\overline{(\sigma v)}_{DT}$, is averaged over the ion velocity distributions. Because this rate parameter is nearly constant over the plasma volume, Eq. (5-2) can be rewritten

$$P_F = \frac{1}{4} \overline{(\sigma v)}_{DT} E_F \int n^2 dV \, . \quad (5\text{-}3)$$

P_{in} in the denominator of Eq. (5-1) can be written similarly by noting that the injected particle current, I_{in}, must just equal the loss current, I_{loss}, for each ion species. The loss is due to scattering into the velocity-space loss cone determined by the magnetic field. For example, the deuterium current is

$$I_{D,\,in} = I_{D,\,loss} = \int \frac{n_D}{\tau_D} \, dV \, .$$

Here, n_D is the density and τ_D is the mean containment time for deuterium. The product $(n\tau)_D$ is nearly constant along a field line; therefore, for a small flux tube it can be removed from inside the integral. Then the injected power can be expressed as

$$P_{D,\,in} = W_{D,\,in} I_{D,\,in} = \frac{W_{D,\,in}}{2n\tau_D} \int n^2 \, dV \, ,$$

where $W_{D,\,in}$ is the injection energy for deuterium, and where we assume that $n_D = n/2$. The total ion density is $n = n_D + n_T$. A similar expression holds for tritium; the total injected power is therefore

$$P_{in} = \frac{1}{2} \left(\frac{W_{D,\,in}}{n\tau_D} + \frac{W_{T,\,in}}{n\tau_T} \right) \int n^2 \, dV \, . \quad (5\text{-}4)$$

If we define a mean $(\overline{n\tau})$ by

$$(\overline{n\tau}) = 2n \left(\frac{1}{\tau_D} + \frac{1}{\tau_T} \right)^{-1} ,$$

and a mean injection energy $\overline{W}_{in}$ by

$$\overline{W}_{in} = \frac{I_{D,\,in} W_{D,\,in} + I_{T,\,in} W_{T,\,in}}{I_{D,\,in} + I_{T,\,in}} = \frac{\tau_T W_{D,\,in} + \tau_D W_{T,\,in}}{\tau_T + \tau_D} ,$$

then Eq. (5-4) simplifies to

$$P_{in} = \frac{\overline{W}_{in}}{4(\overline{n\tau})} \int n^2 \, dV \, .$$

Q for any flux tube is given by the ratio of P_F to P_{in} for that tube. Because in the ratio the volume integrals cancel, Q becomes

$$Q = \frac{(\overline{n\tau}) \, \overline{(\sigma v)}_{DT} \, E_F}{4 \, \overline{W}_{in}} \, . \quad (5\text{-}5)$$

Losses due to bremmstrahlung and synchrotron radiation are negligible for the range of ion energy considered here.[5-1] Losses due to charge exchange with the injected neutral beam are discussed in Section 9. The analysis of the losses due to charge exchange of confined ions with background gas is left for future work.

*If one includes the average kinetic energy of the reactants, then for a 100-keV injection, E_F = 17.7 MeV (see footnote on p. 39).

the calculation of this effect must be included in a plasma buildup calculation.

FOKKER-PLANCK CALCULATIONS

The velocity-space averages of $(n\tau)$ and $(\sigma v)_{DT}$ are obtained from a two-dimensional, multispecies, Fokker-Planck code[5-2] that models the plasma on each magnetic flux surface within the volume. Input to the code includes the mirror ratio, R, the various angles of injection, and the source strength for each plasma species on each flux surface. The spatially-averaged quantities $(\overline{n\tau})$ and $(\overline{\sigma v})_{DT}$ are obtained later by averaging the values on the various flux surfaces with a weighting factor determined by an assumed plasma density distribution $n(\vec{r})$.

The code also calculates the maximum plasma pressure for MHD stability on each flux surface.

Beta is defined as the ratio of perpendicular particle pressure to total perpendicular pressure including the magnetic field:

$$\beta = \frac{p_\perp}{p_\perp + B^2/2\mu_0} \qquad (5\text{-}6)$$

where B is the actual magnetic field in the presence of the diamagnetic plasma. In a mirror machine, β can be quite high $\left(\frac{1}{2} < \beta < 1\right)$ and is limited by the so-called mirror or firehose instabilities. The most severely limiting instability is the mirror mode, which is stable if

$$\frac{B}{\mu_0} + \frac{dp_\perp}{dB} > 0 \,. \qquad (5\text{-}7)$$

The Fokker-Planck code calculates $p_\perp(B)$ from the ion and electron distribution functions and determines the maximum values of $p_\perp$ and β allowed by this condition. Since the particle density n is proportional to $p_\perp$, this condition also determines the maximum fusion power, P_F, that the system can produce. Note that for a given β, $P_F \propto n_0^2 \propto B_{vac}^4$ according to Eq. (5-3) and (5-6), where n_0 is the central ion density. An optimum design would maximize the integral in Eq. (5-3) within the limits set by the criteria for stability. For a given vacuum magnetic field, this integral over the plasma volume should be maximized by varying the location, angle, and energy of injection within the available range of each parameter. This optimization will require more work. The parameters arrived at in the present study are tabulated in Table 5-1 and discussed below.

Injection energies $W_{D,\,in} = 100$ keV and $W_{T,\,in} = 150$ keV were chosen to give equal velocities of deuterium and tritium and to try to maximize the reactor efficiency. Since the technology for positive ion acceleration appears closer at hand, we chose this injection method. Q increases with mean energy $\overline{W}$ because $n\tau \propto \overline{W}^{3/2}$, and $\overline{W}$ is roughly equal to the average injection energy (see Fig. 12-1). However, the efficiency of the neutral beam injector decreases when the energy is increased (see Fig. 12-2) because the cross section σ_{10} for neutralization of the accelerated beam of positive ions decreases with an increase in energy. Figure 12-3 shows that the system efficiency reaches a maximum value of 30% for the injection energies chosen. For injection energy greater than about 130 keV, negative ions appear to be more efficient than positive ions.

Another consideration in the choice of energy is the requirement that the injected beams penetrate deeply enough into the plasma to provide the proper rate of trapping on each field line. Not only must the plasma volume be filled to the required density, but also $n_D = n_T$ must be approximately satisfied everywhere. Equal penetration by D and T requires that the velocities be equal and that the energies be in the ratio of the masses of the two species.

The Fokker-Planck calculations were all based on the magnet design described in Section 7. Briefly, the magnet has a length L= 25 m between mirrors, a field at the mirrors $B_m = 6.8$ T, and a vacuum mirror ratio $R_{vac} = 3.5$. The plasma volume has a radius $r_p = 3.5$ m at the midplane as determined by the outermost field lines within the vacuum chamber. Figure 2-6 shows the plasma volume and two of the four spaces available for injectors. The orientation of the injectors inside the available spaces is determined not only for proper penetration of the beams into the plasma, but also for the best angles with respect to the field lines. If trapped at too steep an angle, the plasma density will reach its rather low stability-limited value near the center without properly filling the volume. If the angle is too small (i.e., too close to the loss cone), the plasma is rapidly lost and Q decreases.

The radial density variation at the midplane n(r) is assumed to be of the form

$$n(r) = n_0(1 - r^3/r_p^3) . \qquad (5\text{-}8)$$

This radial variation is consistent with the trapping calculations below. However, the axial variation of density shows considerable peaking near the center, indicating that the average injection angle is too steep.

Because the Fokker-Planck code used has no spatial dimensions, and because the mirror ratio and the injection angles are different on different field lines, the calculations were made for three representative field lines. For each field line, three injection angles represented the angular spread of the injector system.

The input data are listed in Table 5-2. In the table, the field lines are identified by their radial distance r from the axis at the midplane, and the angles θ_0 represent the angles that the ions make with the field line at the minimum-field point when they are injected at the actual angle θ away from the minimum. To try to get equal densities, the injection particle current was chosen to be (2/3)D

Table 5-2. Input data for the Fokker-Planck calculations ($W_D = 100$ keV, $W_T = 150$ keV, $I_D = 2 \times I_T$).

Field line	Midplane radius (m)	θ (degrees)	θ_0 (degrees)	β	R_{vac}
1	0	51, 65, 80°	51, 63, 70°	0.80	3.50
2	1.4	59, 74, 88°	59, 73, 83°	0.72	3.43
3	2.8	72, 85, 83°	72, 85, 83°	0.34	3.25

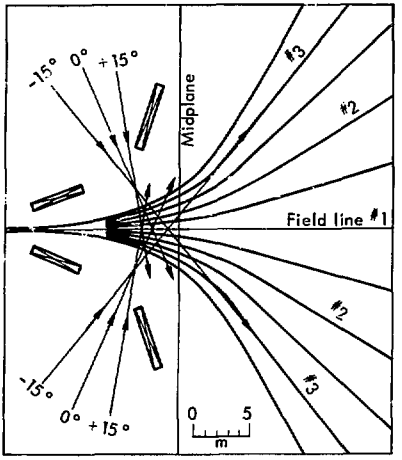

Fig. 5-1. Injection angles and field lines used in the Fokker-Planck calculations.

and (1/3)T. More deuterium than tritium current is needed because deuterium scatters into the loss cone faster than the more massive and more energetic tritium.

The magnitudes of the currents at each field line are finally determined by the densities that give the desired amount of fusion power compatible with the maximum allowed β, as calculated by the code. These currents then must be compared for consistency with the currents on the other two field lines and with the penetration and trapping that the resultant densities give.

Figure 5-1 shows the field lines and injection angles used in the calculations. The figure shows only two of the four injectors located at the four equivalent locations. Azimuthal drift of the trapped ions will ensure uniform density on the flux surfaces.

BEAM PENETRATION

We calculate the current that penetrates to and is trapped on a field line by computing f(x), the fraction of the injected beam that penetrates a distance x into the plasma, where f(x) is given approximately by

$$f(x) = \exp\left\{-\frac{\alpha}{T}\int_0^x ndx\right\}. \qquad (5\text{-}9)$$

T is the "attenuation thickness" ($T = 3.5 \times 10^{15}$ cm^{-2} here) calculated by Riviere.[5-3] Riviere took into account ionization by and charge exchange with each of the various species in the plasma. He did not include the reionization of charge-exchange neutrals. This effect was calculated by Carlson and Hamilton[5-4] and is included in Eq. (5-9) by setting $\alpha = 0.65$ for our energy range.

We calculated f(x) along each of the three injection paths. Then, the fraction of the beam trapped in a given region is given by the drop in f(x) across that region. The appropriate average is calculated for the three paths from all four injector assemblies. When multiplied by the total injection current for each species, this gives the source terms that should be used in the Fokker-Planck calculations on each of the field lines. Since the density on any field line is proportional to the source term on that field line, this calculation of the trapping determines a density that must agree with the density used in the calculation. Figure 5-2 shows the density on the three field lines at the midplane as determined from trapping and also, for comparison, shows a plot of the assumed density variation [Eq. (5-8)]. The values were

normalized to a maximum value of $n = 5.85 \times 10^{13}$ cm^{-3} in both cases to yield a peak fusion power density of 2.2 W/cm^3.

Further work is necessary to determine the proper angles and locations of the injectors in order to avoid the hollow center. Plasma buildup calculations, including the erosion of the plasma surface by the influx of gas, should be done. When these calculations were made for the FERF design,[5-5] it was found that the hollow center can be avoided without excessive penetration of the beam to the walls.

Figure 5-3 shows the variation of the ion density with distance along the axis out to the direct energy converter. To maintain charge neutrality, the electron density is nearly equal to the ion density over the entire distance. At the direct energy converter, where the electrons are repelled by the negative grid, the density is 4×10^6 cm^{-3}. Electron energy is only a few 100 eV here because, to maintain charge neutrality, the mean axial velocity of the electrons must nearly match that of the ions. For these conditions, the Debye shielding distance is only a few centimetres, and this determines the grid spacing and potential at the entrance to the direct energy converter. The direct energy converter is discussed in Section 8.

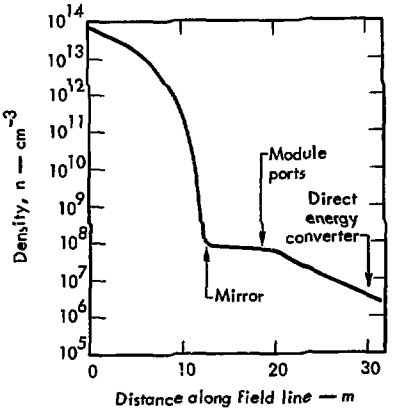

Fig. 5-3. Variation of ion density along the central field line.

CONFINEMENT PARAMETERS

The fusion power produced is proportional to the Q of the system. [See Eq. (5-1) and Fig. 4-1.] The Fokker-Planck calculations yield Q [see Eq. (5-5)] on each field line that is calculated. The results are listed in Table 5-3.

By calculating P_F for the volumes represented by each field line, Q for the entire volume is obtained from the values listed in Table 5-3. To do this, the integral $\int n^2 \, dV$ must be evaluated for each of the three volumes. We numerically evaluated these integrals using the radial density variation from Eq. (5-8) and the

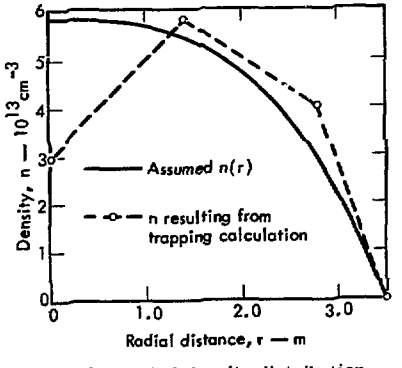

Fig. 5-2. Radial density distribution.

Table 5-3. Parameters obtained from the Fokker-Planck calculations.

Field line	Midplane radius (m)	$(\sigma v)_{DT}$ ($\times 10^{16}$ cm^3/s)	n_D/n_T	Q	$\overline{W}_D$ (keV)	$\overline{W}_T$ (keV)
1	0	9.29	0.95	1.035	113	138
2	1.4	9.23	0.935	0.997	116	143
3	2.8	9.13	0.87	0.827	120	149

longitudinal variation calculated by Moir and Taylor.[5-6]

Table 5-4 gives the values of the various parameters used to evaluate the integrals, including the ranges in radius represented by each of the three field lines. Notice that by using the Moir-Taylor calculations and Eq. (5-8), we are assuming a near-optimum density distribution. Actually, the present injector design produces a radial variation that is low in the center (Fig. 5-2) and a variation along the field lines that is sharply peaked at the center (Fig. 5-3). Experience with the FERF design indicates that the injectors can be adjusted to produce the assumed distribution.

$\overline{(\sigma v)}_{DT}$ is obtained from the calculated Fokker-Planck energy distributions. Then the total fusion power is given by

$$P_F = \frac{1}{4} E_F \sum \overline{(\sigma v)}_{DT} \int n^2 \, dV$$

$$= 16.7 + 124.0 + 70.2 = 210 \text{ MW}$$

From Table 5-3, the Q values corresponding to these volumes are 1.035, 0.997, and 0.827. Summing the ratios $P_{in} = P_F/Q$ for the three volumes gives

$$P_{in} = 16.1 + 124.4 + 84.9 = 225 \text{ MW} .$$

Thus, the overall Q for the system is $Q = P_F/P_{in} = 0.935$. The value of the confinement parameter $(\overline{n\tau})$ can now be obtained from Eq. (5-5). Table 5-3 shows that $\overline{(\sigma v)}_{DT} \approx 9.2 \times 10^{16}$ cm^3/s for all three volumes. Substituting values into Eqs. (5-4) through (5-5) gives $\overline{W}_{in} = 116.7$

Table 5-4. Parameters used to evaluate the integral $V = \frac{1}{n_0^2} \int n^2 \, dV$.

Field line	Radii at midplane		$\tilde{A}$ (m^2)[a]	C[b]	n/n_0[c]	V (m^3)[d]
	Inner (m)	Outer (m)				
1	0	0.7	1.54	0.194	0.999	7.45
2	0.7	2.1	12.3	0.207	0.936	55.77
3	2.1	3.5	24.6	0.218	0.488	31.93

[a] $\tilde{A} = \pi(r^2_{inner} - r^2_{outer})$.

[b] C was calculated in Ref. 5-6 by integrating $(n/n_0)^2$ along a field line and assuming a normal mode distribution. C is a function of the mirror ratio on that field line.

[c] We assume $n = n_0(1 - r^3/r_p^3)$, with $r_p = 3.5$ m.

[d] $V = \tilde{A}$ C L $(n/n_0)^2$, where L = 25 m for each field line.

keV and

$$\overline{(n\tau)} = \frac{4\overline{W}_{in}\, Q}{\overline{(\sigma v)}_{DT}\, E_F} = 2.7 \times 10^{13}\ \mathrm{s/cm^3}\ .$$

Since P_F and P_{in} both depend on ion density in the same way, Q is independent of ion density. Also, because the fission power produced in the blanket is proportional to the fusion power, the entire power flow (see Fig. 4-1) varies as the square of the density n. We can therefore choose n to give any desired electric power output, P_e, by setting the magnetic field strength high enough to satisfy the conditions for stability. Therefore $P_e \propto n^2 \propto B_{vac}^4$, and the output power is seen to increase rapidly with an increase in magnetic field.

ADIABATICITY

Magnetic field strength is also the determining factor for the adiabatic behavior of the various ions. The condition for adiabatic confinement[5-7] is usually assumed to be

$$\frac{1}{\Omega}\frac{\partial \Omega}{\partial t} < \frac{\Omega}{N}\ , \qquad (5\text{-}10)$$

where $\Omega = ZeB/M$ is the cyclotron frequency, and $N \approx 20$ is a dimensionless parameter. We examined the restrictions that this inequality places on both the radial and the longitudinal motion of the ions. Equation (5-10) defines the condition for adiabatic magnetic confinement at low plasma density.[5-7] In our case, the plasma is dense enough ($\beta = 0.8$) to produce gradients in the magnetic field that are much greater than those in the vacuum field. There are as yet no good criteria for adiabatic behavior at high β. Because of the periodic nature of the ion motion in the field, the nonadiabatic transfer of energy between particles and field could cancel out to a large extent.

For this report, we studied the consequences of Eq. (5-10) when Ω is expressed in terms of a smoothly varying approximation to the actual magnetic field. We approximate the magnetic field by

$$B = B_{vac}\left[1 + (R - 1)Z^2/\ell^2\right] \times (1 - \beta)^{1/2}\ ,$$

where $\beta = \beta_0[1 - (r/r_p)^3]$, $\beta_0 = 0.8$, $r_p = 3.5$ m, and ℓ is the value of z at $B = B_m$. Since the magnetic field is constant in time, Eq. (5-10) is equivalent to the two conditions

$$\frac{v_\perp}{\Omega B}\frac{\partial B}{\partial r} < \frac{1}{N}\ , \quad \frac{v_\parallel}{\Omega B}\frac{\partial B}{\partial z} < \frac{1}{N}$$

for transverse and longitudinal motion, respectively. $v_\perp$ and $v_\parallel$ are corresponding velocity components. Because β is large ($\beta = 0.8$), the radial variation dominates and the condition becomes

$$\frac{Mv}{Ze\, B_{vac}} < \frac{r_p}{40} \approx 9\ \mathrm{cm}\ . \qquad (5\text{-}11)$$

Here, M/Ze is the mass-to-charge ratio, v is the ion velocity, B_{vac} is the central vacuum field, and r_p is the plasma radius at the midplane. This gives $W_{D^+} < 700$ keV, $W_{T^+} < 500$ keV, and $W_{He^{++}} < 1500$ keV. Therefore, the 3.52-MeV He^{++} that result from the D-T fusion reactions will not be adiabatically confined. Since their energy per charge is much greater than the potentials used for direct conversion, the fraction of their energy that is directly converted is negligible. The thermal bottoming cycle to the direct energy converter receives most of the He^{++} energy.

Figures 5-4 and 5-5 show the velocity distribution of the contained D^+ and T^+ as determined by the Fokker-Planck calculations. The adiabatic limits are safely beyond even the tails of the distributions.

Equation (5-11) shows that the energy limit for adiabaticity increases as the square of the central field strength for a given β and mirror ratio. Therefore, to confine the α particles the central field would have to be increased from 1.94 T to 3.0 T. If the mirror ratio were maintained, the mirror field would increase to 10 T. Such a 50% increase in field could yield a five-fold increase in fusion power if the injectors and other components are scaled up accordingly. In addition, the confined α's would thermalize in the plasma, raising its mean energy and increasing $n\tau$ and Q. The Fokker-Planck calculations indicate that this would decrease the required injection power by about 10%. The best choice of magnetic field strength will be determined by economic considerations and is discussed in Section 12.

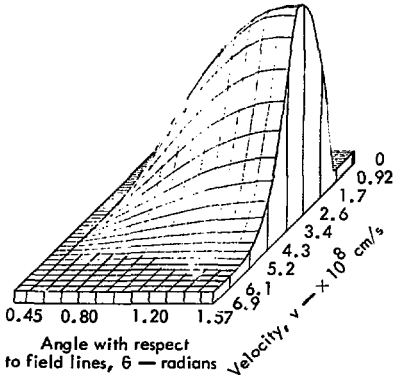

Fig. 5-4. Velocity distribution of confined D^+ ions.

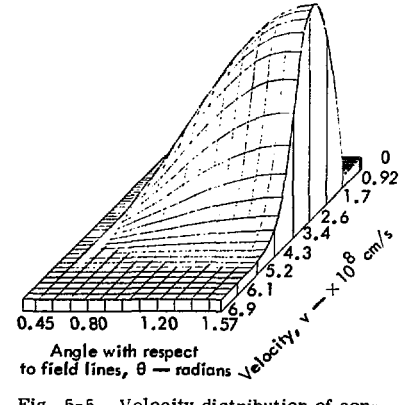

Fig. 5-5. Velocity distribution of confined T^+ ions.

FUSION REACTION PRODUCTS

Each D-T fusion reaction results in a 14.06-MeV neutron* and a 3.52-MeV α-particle for a total of 17.58 MeV. Therefore, the rate of production, S, of neutrons is given directly by P_F divided by 17.58 MeV. Since P_F = 210 MW here, $S = 7.5 \times 10^{19}$ neutrons/s. This is also the rate of production of α particles and the rate of consumption of tritium. Or, stated another way, the tritium consumption rate is 12 kg/yr. The neutrons enter the uranium blanket and release

*Leonard and Wolkenhauer[5-8] have shown that the kinetic energy of the reactant ions results in a spread in the neutron energy. They calculate a full width at half maximum of 1.70 MeV centered at 14.20 MeV for essentially the same ion energy distribution as considered here. The product He^{++} will also have a 1.70-MeV spread and a shift that is four times greater than for neutrons, giving a mean α-energy of about 4.0 MeV.

more power through the resulting fissions. The neutronics are discussed in Section 6, where the production of plutonium through (n,γ) reactions and the breeding of tritium are also discussed.

WALL LOADING DUE TO BEAM PENETRATION

We have already discussed the interaction of the neutral beam and the plasma from the viewpoints of injector design and plasma maintenance against end losses. We must also consider the first-wall power flux due to the penetration and charge exchange of injected energetic neutrals.

The average trapping fraction for the injected power is 94%; therefore, the total power to the first wall due to the injected beams is (1 - 0.94) 239 = 14 MW. The power density on the first wall varies from essentially zero to a maximum which is many times the average. Figure 5-6 shows the geometry of one injector system and the blanket module opposite the injection port. The individual beams of the injector system converge to pass through the injection port and diverge as they pass through the reactor and encounter the first wall. The diverging beam shape is that of a rectangular-based pyramid (apex angles 30° and 60°). The maximum power flux on the first wall occurs at point A for two reasons –

- Point A is the location of the first contact of the wall by the diverging beam, and
- The plasma attenuation is a minimum along the ray leading to point A.

In addition to point A, we calculate the power flux at point B for comparison.

The beam power deposition on the first wall in the absence of plasma attenuation

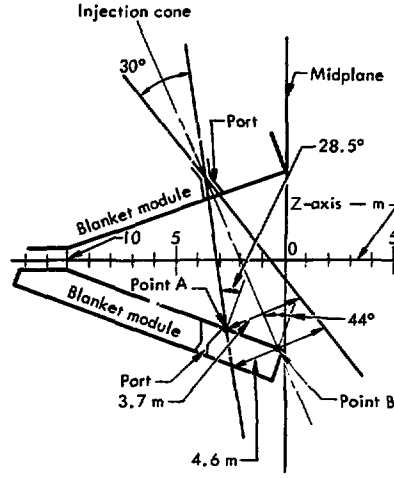

Fig. 5-6. Geometry of injection.

can be calculated from the geometry of Fig. 5-6. The results are

Point A: 180 W/cm^2

Point B: 94 W/cm^2

In the presence of the plasma, the trapping fractions along the rays leading to points A and B are 0.846 and 0.968. We estimate the power density on the wall in the presence of plasma by multiplying the no-attenuation values by 1 minus the trapping fraction. The results are

Point A: 28 W/cm^2

Point B: 3 W/cm^2

These estimated values are somewhat higher than the actual power flux because the charge-exchange neutrals are actually distributed over a larger area about the beam ray.

REFERENCES

5-1. R. W. Moir, in Proc. First Topical Meeting Tech. Contr. Nucl. Fusion, 1974 (San Diego, 1974), 740402-P1, vol. 2, p. 373.

5-2. M. E. Rensink, J. Killeen, and A. A. Mirin, Some Recent Computational Results on Mirror Confinement, Lawrence Livermore Laboratory Rept. UCID-16459 (1974); and J. Killeen, A. A. Mirin, and M. E. Rensink, "The Solution of the Kinetic Equations for a Multi-Species Plasma," in Methods in Computational Physics (Academic Press, New York, 1975) vol. 16, chapter XI.

5-3. A. C. Riviere, Nucl. Fusion 11, 363 (1971).

5-4. G. A. Carlson and G. W. Hamilton, in Proc. First Topical Meeting Tech. Contr. Nucl. Fusion, 1974 (San Diego, 1974), 740402-P1, vol. 1, p. 401.

5-5. T. H. Batzer et al., Conceptual Design of a Mirror Reactor for a Fusion Engineering Research Facility (FERF), Lawrence Livermore Laboratory Rept. UCRL-51617 (1974).

5-6. R. W. Moir and C. E. Taylor, in Proc. Technology of Controlled Thermonuclear Fusion Experiments and the Engineering Aspects of Fusion Reactors, 1972 (Austin, Texas, 1972), CONF-72111, p. 853.

5-7. J. H. Foote, Plasma Phys. 14, 543 (1972).

5-8. B. R. Leonard, Jr. and W. C. Wolkenhauer, in Proc. Plasma Physics and Controlled Nuclear Fusion Research, 1974 (Fifth IAEA Conf., Tokyo, Japan, 1974), IAEA-CN-33/G6-2.

6. Blanket Design

INTRODUCTION

The gross blanket geometry is defined by the plasma and coil geometries for a minimum-B Yin-Yang magnetic mirror. The blanket shown schematically in Fig. 2-4, is constructed from pie-shaped modules whose assembled geometry conforms to the Yin-Yang magnetic field. Each module, in turn, is composed of a collection of domed, cylindrical, pressure vessels (submodules) welded to the module base.

The submodule, the basic component of the blanket, contains an inner fast-fission zone and an outer tritium-breeding zone. These zones are composed of natural uranium carbide and lithium aluminate contained in wire-wrapped pins in a hexagonal array. Helium coolant is supplied to, and removed from, the submodule by plena in the module base. The helium flow within the submodule first cools the pressure vessel wall and then removes the heat from the fuel pins and the heat and tritium from the breeding pins.

A new blanket starts life with natural uranium fuel and has an energy multiplication, M, of 8.1 and a net fissile

breeding ratio (NFBR) of 1.23 atoms/fusion. As the blanket is exposed, it will enrich itself in plutonium, thereby causing M to increase and NFBR to decrease. With the refueling scheme used, the lifetime average M is 12 and the lifetime average NFBR is 0.9 atoms/fusion.

GENERAL OBJECTIVES

A primary objective of this study was to develop a conceptual blanket design with the potential of meeting both the thermomechanical and neutronic requirements in an economic manner. Thus, the blanket must

- Conform to the plasma and coil geometries imposed by the minimum-B Yin-Yang magnetic mirror,
- Be a nearly leak-tight pressure vessel,
- Be capable of being refueled and replaced,
- Be cooled under both normal and abnormal conditions,
- Operate at a high enough power density to be economically interesting, and
- Have attractive neutronic performance.

Areas which must be addressed include the neutronic and thermomechanical considerations listed in Table 6-1. In describing the options we considered and the design choices we made, we shall discuss basic choices, modularization and accessibility, module design, thermal hydraulics, neutronics, blanket and fuel management, and safety.

BASIC CHOICES

Undertaking a point design study forces us to make some rather basic choices regarding the type of blanket we want and the types of materials we will use for fuel, moderator, structure, and coolant.

Table 6-2 lists and compares the three general types of hybrid blanket. In selecting the type of blanket to use, the

Table 6-1. Hybrid blanket considerations.

Neutronic Considerations	Thermomechanical Considerations
Energy multiplication (M)	Structural design
Tritium breeding ratio	Structural lifetime
Fissile breeding ratio	Heat removal:
Fissile inventory	Normal operation
Exposure effects	Normal shutdown
Fissile fuel and tritium doubling times	Abnormal shutdown
	Power density
	Coolant pumping power
	Remote refueling
	Tritium removal
	Tritium containment
	Tritium inventory
	Fission product containment
	Material compatibility

Table 6-2. Types and characteristics of hybrid blankets.

Hybrid blanket	Description	Produced per DT neutron[a, b]
Fertile blanket	Only breeding of tritium to fuel the D-T reactor and breeding of fissile material (^{233}U and/or ^{239}Pu) to fuel separate critical fission reactors takes place. To minimize fission in the blanket, the fertile material must be continuously reprocessed.	~0.3 to 0.6 fissile atoms; ~20 MeV.
Fast-fission blanket	High-energy DT neutrons are used to directly fission a fertile material. Both fission energy and neutrons are produced; the neutrons are used to breed both fusion and fissile fuels.	~1.0 to 2.0 fissile atoms (net); ~100 to 200 MeV.
Thermal fission lattice blanket	A fast-fission inner zone drives a heterogeneous thermal fission lattice that is fueled with natural or slightly enriched uranium or thorium seeded with ^{235}U or ^{233}U.	~0 to 1.0 fissile atoms (net); 300 to 500 MeV.

[a]References 6-1 through 6-8.

[b]The expected effects of tritium breeding and structural requirements are included.

following points were considered:

- A mirror hybrid with a thermal lattice blanket had already been the subject of a point design study undertaken jointly by Battelle Northwest Labs (BNW) and LLL.[6-9, 6-10]
- We wanted to breed significant amounts of excess fissile fuel and to have a high enough M to give a reasonable system efficiency.
- Results from the earlier neutronic studies of fast-fission blankets suggested that a simple fast-fission blanket and a mirror machine might achieve the desired results.

With these considerations in mind, we chose a fast-fission blanket for this study.

The next step was to choose specific materials for the fissile and fertile fuel, tritium breeding material, neutron moderator, coolant, and structure. Table 6-3 lists the blanket materials we considered. For this particular design, the following material choices were made:

- Fissile and fertile fuel: Natural uranium carbide at 85% of theoretical density and clad in stainless steel. Uranium carbide fuel is being developed for the liquid-metal fast breeder reactor (LMFBR).
- Structural material: Stainless steel.
- Coolant: Helium.
- Tritium breeding material: Lithium aluminate ($LiAlO_2$).[6-11]
- Moderator: Graphite (for use in tritium-breeding region).

There is nothing unique about the materials chosen. In future work we shall examine other combinations of materials. For example:

- The high-temperature, high-burnup capabilities of uranium carbide could

be traded for the better neutronic performance of uranium metal.

- Depleted uranium might be economically more attractive than natural uranium.
- Better neutron economy might be achieved by using materials with low absorption cross sections for the structure materials, e.g., alloys of zirconium or aluminum.
- Different tritium breeding materials, such as LiAl, might simplify the tritium-recovery task.
- Natural lithium can be used to eliminate any requirement for isotope separation.

MODULARIZATION AND ACCESSIBILITY

One of the central objectives of this study has been to develop a reactor design in which the blanket could be maintained and replaced. To facilitate the removal of blanket modules with minimum disturbance of either the remainder of the blanket or the other reactor systems (coil winding, coil support structure, or injectors), we developed the modular blanket geometry illustrated in Fig. 6-1. In this design, the blanket is constructed from pie-shaped modules whose assembled topology resembles the Yin-Yang field geometry. A blanket module is removed by moving it linearly and radially outward through the space between the upper and lower winding of each mirror coil until it is clear of the coil and radiation shielding (see Fig. 3-2). After a module is clear of the coil structure, it may be transported circumferentially around the outer perimeter of the coil to a containment cell.

Any module may be removed without disturbing any other modules. The design

Table 6-3. Material choices for the hybrid blanket.

Fissile and fertile fuels	Tritium-breeding materials	Moderators	Coolants	Structural materials
U alloys	Li	None	He	Fe (alloy)
	LiAl			
UO_2	$LiAlO_2$	C	Li	Zr (alloy)
UC	Molten salt	LiH	Na	
UN			Molten salt	Al (alloy)
Molten salt		ZrH		C
U cycle:	(Where the Li can be natural, enriched or depleted in ^6Li)	H_2O	H_2O	
U depleted		Be		
U natural		BeO		
U enriched				
Spent LWR fuel				
U + Pu				
Th-cycle:				
Th + ^{235}U				
Th + ^{233}U				

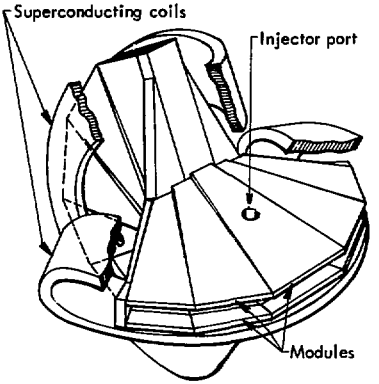

Fig. 6-1. Schematic arrangement of blanket modules.

of the coil support structure allows the removal of any blanket module without either the coil winding or the coil support structure being disturbed. Also, the linear, radially outward motion of blanket modules during removal does not disturb the injector system or its associated pumping ducts.

The small total number of blanket modules in this design (20) and the several different geometries (5) limit the potential economic advantages accompanying mass production of identical modules. However, the constant, standardized thickness of all the modules allows the large number of individual submodules (coolant passage/fuel assemblies) to be geometrically identical, and greatly facilitates the design and production of the blanket submodules.

MODULE DESIGN

As just described, the blanket consists of an assembly of modules that is inside the coils and surrounds the plasma

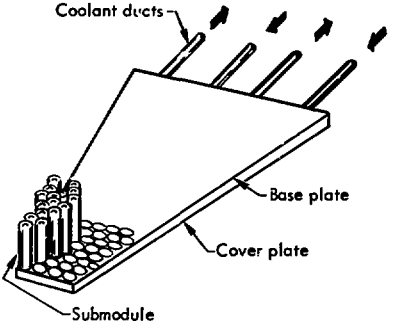

Fig. 6-2. Blanket module layout.

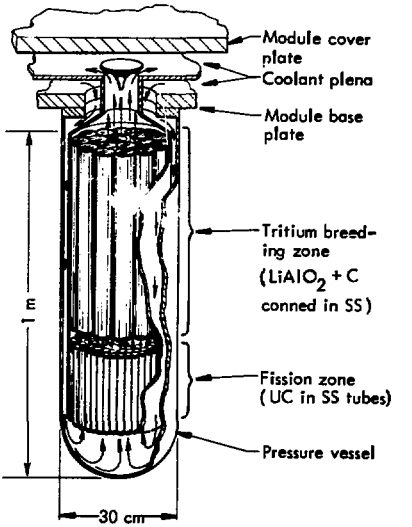

Fig. 6-3. Fast-fission blanket submodule.

(Fig. 6-1). Each module consists of a collection of domes, i.e., of cylindrical pressure vessels (submodules) mounted to a base plate (Fig. 6-2). Coolant manifolds or plena behind the base plate supply and collect helium from the submodules (Fig. 6-3). The submodules are ~30 cm

in diameter, except for some smaller ones needed to fill in gaps at the module edges. There are approximately 400 submodules per module and 20 main modules per blanket. Submodules occupy ~80% of the module surface area. Tie rods located between the submodules connect the base plate to the cover plate. The modules weigh ~100 tonnes; if they prove to be too heavy to handle, the blanket must be subdivided into more modules.

The blanket submodule consists of two zones, an inner fast-fission zone and an outer tritium-breeding zone (Fig. 6-3). Helium (at ~20 atm and ~300°C) supplied to each submodule from the inner manifold (just above the base plate) flows down the annular void between the inner radius of the submodule pressure vessel and the outer radius of the subassembly. This flow configuration keeps the temperature of the pressure vessel close to that of the inlet helium. Stainless steel was chosen as the blanket structural material; however, either zirconium or an aluminum alloy could also be used for the pressure vessel. If a low-temperature tritium-breeding material such as LiAl alloy is used, the inlet helium would also cool it.

At the domed end of the pressure vessel, the helium flow reverses and is directed into the fast-fission zone. The end cap of the submodule (which is the first wall of the blanket) is cooled by the helium flow as it is reversing direction. If the eddying or swirling of the helium as it reverses does not provide a sufficient heat transfer rate to cool the first wall, internal baffles and or fins could be added to increase the heat transfer rate.

Since major first-wall heating is a localized problem caused by the neutral beams, it might be attractive to place thin shields in front of the first wall to radiatively distribute the heat over a larger area of the blanket. Such a shield would also protect the pressure vessels from bombardment by neutral atoms. This shield could also protect the plasma from sputtered blanket material and small gas leaks.

After cooling the first wall, the helium flows up through the fast-fission zone where ~90% of the blanket heat is generated. The fission zone consists of a cylindrical bundle of wire-wrapped, stainless-steel clad natural uranium carbide fuel pins ~20 cm long. The pin bundle is tightly packed, and the pins are in an hexagonal array.

If a low-temperature tritium breeder were used, the hot helium leaving the fission zone would be ducted directly to the return manifold. With the high-temperature tritium breeding material, $LiAlO_2$, some or all of the hot helium flows through the tritium breeding zone before being ducted to the return manifold. The tritium breeding region is kept hot to promote tritium diffusion out of the 50-μm-diam $LiAlO_2$ particles and into the helium coolant stream from which it is removed. Tritium recovery is discussed in Section 10. Alternately, the tritium could be collected in a separate manifold.

The helium now leaves the submodule and enters the return side of the manifold. The hot and cold sides of the manifold are separated by an insulating plate.

A possible refueling sequence for the module-submodule blanket design is as follows:

- Shut down the reactor and allow the afterheat to drop to a small fraction of operating power.

- Remove the desired number of modules, replace them with spares, and renew reactor operation.
- After a suitable cooling-off period, remove the tie-rod nuts and lift the cover plate off the module.
- Remove the nuts securing the manifold separator (which also serves as the submodule hold-down plate). Depending on their exposure, either reposition the submodules in the module or remove them. If any submodule pressure vessels have reached maximum allowable exposure, replace them. Maximum allowable exposure is estimated to be 5 MWY/m^2 (energy fluence of 14-MeV neutrons).[6-12] After the module has been reassembled and tested, it is ready to be placed back into the blanket.

THERMAL HYDRAULICS

The objective of the thermal hydraulics analysis was to determine a submodule configuration that demonstrated acceptable engineering performance (i.e., temperatures, stresses, etc.) within the economic constraints of

- Minimal structural fraction (within mechanical limitations) to obtain good neutronic performance.
- Low pumping power (pumping power/thermal power $\lesssim 4\%$), and
- Coolant temperatures that would yield good efficiency for the thermal energy-conversion system (T_{in} = 300°C, T_{out} = 600°C).

The engineering constraints on the design were fixed at:

- Maximum clad temperature ≈700°C,
- Maximum fuel temperature ≈2200°C,
- Maximum pressure vessel temperature = 550°C,
- Pressure vessel working stress = 10^4 psi.

The material used for the clad is stainless steel, and the maximum clad temperature was selected to be that value used in the proposed gas-cooled fast breeder reactor.[6-13] The fuel is uranium carbide, and its maximum temperature was set a few hundred degrees below melt (a conservative value). The pressure vessel is also stainless steel, with the working stress and maximum temperature set so that the thermal creep strain is small compared to the anticipated irradiation creep strain.[6-12] Also, the plasma conditions fixed the (peak) first-wall thermal loading from the injectors at 28 W/cm^2 and the peak heat generation rate in the uranium carbide and structural materials at 100 W/cm^3 and 10 W/cm^3, respectively.*

To obtain acceptable blanket performance, the following parameters were varied in the thermal hydraulic analysis:

- Core geometry (fuel pin diameter, clad thickness, and fuel pin pitch-to-diameter ratio),
- First-wall coolant passage geometry,
- Coolant pressure.

Also, the heat-generation rate was varied to determine the economic tradeoffs resulting from varying the fusion power density.

The analysis was performed with a code that was written specifically for the steady-state thermal hydraulics of the blanket submodule. The analytical model is described briefly in the next paragraphs.

*Typical of peak values at start of blanket life.

Analytical Model

The numerical scheme for the analytical model is based on the technique of dividing the flow passage into axial sections, or nodes, so that each node has a simply described geometry and a small variation in thermal hydraulic properties (temperatures and fluid properties) between the node inlet and outlet. The axial and radial nodalization technique is shown schematically in Fig. 6-4. Given the inlet fluid conditions to the submodule, the outlet fluid conditions from each node and the material temperatures in the node can be determined as a function of the geometry and heat-generation rate.

The geometry in the code was constrained only by the requirements for downflow in an outer annulus and return upflow through the center of the cylindrical submodule. The location of the various components within the submodule and all dimensions are specified as input.

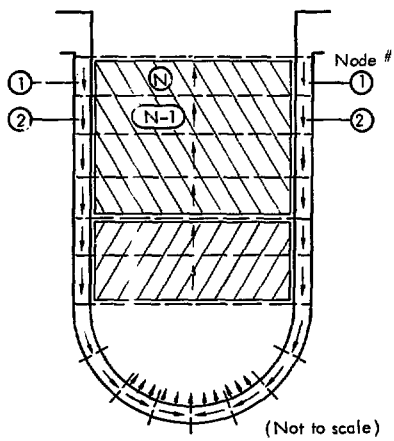

Fig. 6-4. Numerical modulization scheme.

The fuel and breeding material were modeled as a wire-wrapped pin design in a hexagonal array. First-wall cooling was provided by extending the flow baffle around the inside of the first wall to form a first-wall flow annulus. The coolant exits from the annulus through a series of holes in the baffle. The location and size of the flow passages in the baffle were specified as input to the code so that the first-wall flow could be adjusted to provide the required cooling while minimizing the pressure drop in this region.

Thermal energy is assumed to be generated in all solid materials, and the first wall is subjected to a heat flux from the neutral beam injectors. Heat flow is assumed to occur in the radial direction by conduction and convection from the solid materials into the coolant, and it is transported axially by the fluid flow. Axial conduction is neglected. The radial energy transport includes heat transfer across the flow baffle between the cold downflow and hot upflow.

The coolant was treated as a one-dimensional compressible flow, and the effects of friction, heat transfer, and area change were included. The friction factors and heat-transfer coefficients were calculated from standard turbulent-flow correlations[6-13] for the particular flow geometries occurring in the submodule (i.e., the annulus, hexagonal pin array, and circular cylinder). The model for the pressure drop in the hexagonal pin arrays included the effect of wire wraps, but the increase in heat transfer due to the wire wraps was not accounted for. Thus, the values for the heat-transfer coefficients are conservative, and the resulting clad temperatures are somewhat high.

Calculating the flow in the first-wall annulus required some approximations due to the unusual geometry in this region. The friction factors and heat-transfer coefficients evaluated from straight-flow correlations were corrected for flow in a curved duct, [6-14] and the flow as it turned and exited from the annulus through the baffle was assumed to suffer a pressure drop due to turning and orificing.

The temperature distribution in the solid materials was evaluated in each axial section by placing a single node in each of the structural components (pressure vessel, flow baffle, and clad), and two nodes in the fuel and tritium breeding material (average and centerline temperatures). A gap heat-transfer coefficient between the fuel and the clad was used, and constant material properties were assumed. The heat-generation rate, as a function of distance from the first wall, was evaluated from the neutronics calculations (see Table 6-7).

The pumping power required to provide the coolant flow for the submodule was evaluated from the mass flow rate, density, and pressure drop[6-15] calculated in the thermal hydraulic analysis.

Results for the Reference Design

Normal Operating Conditions

Preliminary calculations with the thermal hydraulics code resulted in a submodule configuration that was selected as the reference design. The parameters characterizing the geometry and performance of the reference design are presented in Tables 6-4 and 6-5. This design, which is not optimized, was selected on the basis of being a design that satisfied the economic/engineering constraints discussed previously. A sensitivity study that evaluated the effects of varying some of the parameters listed in Table 6-4 is presented on p. 51. The primary significance of the reference design is that it uses established engineering technology to demonstrate the feasibility of the proposed blanket concept.

Several aspects of the submodule performance that are not evident from Tables 6-4 and 6-5 warrant further discussion and qualification.

Table 6-4. Geometry of reference design submodule.

Pressure vessel:		
Diameter		30 cm
Wall thickness		0.44 cm
Fuel pin:		
Diameter		1.5 cm
Pitch-to-diameter ratio		1.05
Clad thickness		0.02 cm
Length		20 cm
Width of downflow annulus		0.3 cm
Thickness of flow baffle		0.1 cm
Fuel volume fraction	in the fission zone	0.675
Fuel volume/structure volume	in the fission zone	6.29

We found that the majority of the pressure drop (~ 80%) occurs in providing the first-wall cooling, where the flow must be accelerated to high velocities (~ 250 m/s) to maintain the first wall at an acceptable temperature. The pressure loss occurs when this high-velocity flow must be turned and rapidly decelerated at the module centerline. Although the required first-wall cooling can be provided in the present design with an acceptable pressure drop, we are considering several alternate cooling schemes that should significantly decrease the pumping requirements for the first-wall cooling and thus increase the economic performance of the submodule. Approximately 90% of the thermal power generated in the submodule occurs in the fission core, indicating that, for an efficient design, most of the total pressure drop should also occur in this region.

The flow baffle maintains the pressure vessel as near the coolant inlet temperature as possible, because this component of the submodule is highly stressed. Thus, the baffle must serve as a flow divider and thermal insulator between the cold downflow and hot upflow. We found that the baffle itself need not be a good thermal insulator because the fluid boundary layers on either side of the baffle provide sufficient thermal resistance to eliminate significant heating of the downflow. In the reference design, the baffle was constructed from 0.1-cm-thick stainless steel, and the temperature rise of the coolant in the downflow annulus, due to heat transfer from the hot upflow, was ~ 25°C.

Table 6-5. Performance of reference design steady-state submodule.

Thermal power	662 kW
Maximum material temperatures occurring in the submodule:	
Clad	730°C
Fuel	800°C
Pressure vessel	430°C
$LiAlO_2$	615°C
Coolant:	
Mass flow rate	0.424 kg/s
Inlet pressure	20 atm
Pressure drop, $\Delta P/P$	0.042
Pumping power/thermal power	0.037
Fission core velocity	~35 m/s
Inlet temperature	300°C
Outlet temperature	600°C
Temperature rise in downcomer	29°C
Temperature rise along the first wall	24°C
Maximum power density:	
Fuel	100 W/cm^3[a]
Structure	10 W/cm^3
Maximum heat flux:	
Fuel	36 W/cm^2
First wall	28 W/cm^2
Flow baffle	27 W/cm^2

[a] At start of life.

Table 6-6. Performance of reference design submodule when depressurized.

Thermal power	31.4 kW
Maximum material temperatures:	
Clad	700°C
Fuel	703°C
Pressure vessel	175°C
$LiAlO_2$	620°C
Coolant:	
Mass flow rate	0.0121 kg/s
Inlet pressure	1 atm
Pressure drop, $\Delta P/P$	0.0105
Pumping power	0.123 kW
Fission core velocity	~15 m/s
Inlet temperature	100°C
Outlet temperature	600°C
Maximum power density:	
Fuel	5 W/cm^3
Structure	0.5 W/cm^3
Maximum heat flux:	
Fuel	1.8 W/cm^2
First wall	—
Flow baffle	2.6 W/cm^2

In the present submodule design, we did not explicitly include the core support structure. We realize that this structure will cause some degradation of the performance (decreased energy multiplication and increase pressure drop), however, the effect should be minor.

Depressurized Condition

As described earlier, we selected as the design basis accident (DBA) for the hybrid a depressurization of the primary coolant loop and simultaneous loss of the plasma. Thus, the thermal hydraulic conditions in the submodule for a DBA are 1-atm coolant pressure and an afterheat power level (which was taken to be 5% of the normal operating power).[6-16] The submodule performance was evaluated under these circumstances, and the results are presented in Table 6-6. The afterheat can be removed and the blanket operated in a steady-state mode by circulation of helium at 1 atm. The coolant inlet temperature of 100°C assumes that a heat exchanger is incorporated in the emergency cooling loop that transfers the afterheat to an ambient-temperature heat sink. The pumping requirements for the afterheat removal are quite modest. In addition, at least 5 min is available following the loss of flow before auxiliary cooling must commence in order to prevent clad melting.

Sensitivity Study

In examining the effects of varying some of the parameters that characterize the submodule, we used the reference submodule as a base case. The sensitivity study included varying the first-wall cooling geometry, the fission core geometry, the coolant pressure, and the power density. The results of this study

are shown in Fig. 6-5 (a through f) by plots of maximum fuel temperature (T_F), maximum clad temperature (T_{clad}), the ratio of pumping power to thermal power

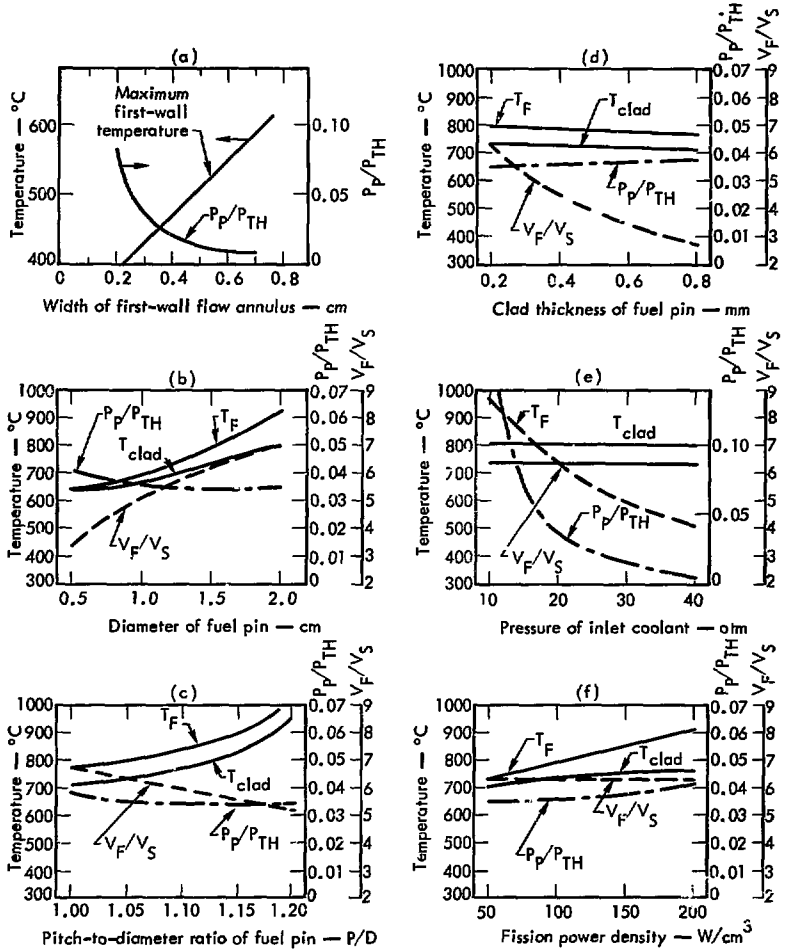

Fig. 6-5. Results of sensitivity study to examine the effects of varying some of the parameters that characterize the submodule: (a) Variation in first-wall cooling geometry; (b) Variation in fuel pin diameter; (c) Variation in fuel pin pitch-to-diameter ratio; (d) Variation in fuel pin clad thickness; (e) Decrease in fuel radius with increase in clad thickness; (f) Inlet coolant pressure.

(P_P/P_{TH}) and the fuel-to-structure-volume ratio (V_F/V_S) in the fission zone.

Figure 6-5(a) shows the results of varying the design of the first-wall flow passage, where the objective was to obtain an acceptable first-wall temperature (< 550°C) within the constraint of a maximum value of 4% for the ratio of pumping to thermal power. We found that a flow-passage width of 0.3 cm satisfied these two criteria. Note that since P_P is the total pumping power for the submodule, the very strong dependence of P_P/P_{TH} on [illegible] of the first-wall flow passage [illegible] pressure drop in the [illegible] by the coolin[illegible]ements of the first wall.

Figur[illegible]s 6-5(b, c, d) show the effects of varying the geometry of the fission core. These calculations were performed while holding a coolant temperature rise of 300°C through the submodule, a constant thermal output of 662 kW per submodule (by varying the fuel pin length), and thus a constant mass-flow rate. To provide high energy multiplication, the fuel-to-structure-volume ratio should be large, a requirement which dictates a large pin diameter, small pitch-to-diameter [illegible] (P/D), and small clad thickness. To yield a satisfactory design, there must be a trade-off between the neutronic performance and the engineering constraints.

The limiting material constraint in the core of the reference design is the clad temperature, which is determined by the temperature of the bulk coolant ($T_{coolant}$) and the coolant film temperature drop (ΔT_{film}),

$$T_{clad} = T_{coolant} + \Delta T_{film} .$$

Since the coolant temperature is fixed between 300°C and 600°C by the thermal energy conversion syste[illegible], ΔT_{film} must be maintained at a low enough value to meet the criteria for the maximum clad temperature. The film drop is determined by the fuel pin heat flux $\dot{q}''_{fp}$, and the coolant transfer coefficient heat, h_c,

$$\Delta T_{film} = \frac{\dot{q}''_{fp}}{h_c} .$$

Figure 6-5(b) shows the variation in clad temperature as a function of the fuel-pin diameter at constant P/D. The heat flux increases in proportion to the pin diameter, and the heat-transfer coefficient decreases slightly, resulting in larger film temperature drops at larger pin diameters. Figure 6-5(c) shows the clad temperature as a function of pitch-to-diameter ratio at constant pin diameter. For this parameter variation, the heat flux remains constant. However, increasing P/D increases the flow area and decreases the coolant velocity, resulting in lower heat transfer coefficients and larger values of ΔT_{film}.

Thus, the neutronics requirement of high V_f/V_s and the material constraint of low T_{clad} can be simultaneously accomodated by using a core with large pin diameters and small pitch-to-diameter ratios. The lower limit on the pitch-to-diameter ratio is determined by the structural requirements of the wire wrap and circumferential temperature variations in the fuel pin, which become severe at low P/D.[6-17] The determination of a minimum P/D has not been addressed in the present study.

As stated previously, most of the pressure drop occurs in the first-wall coolant passage, and thus the pumping power curves are not very sensitive to the core configuration. However, it can still be seen that the pumping requirements decrease with increasing pin size and increasing P/D. A general characteristic of the blanket is that, at the low power density used, the pumping requirements for the submodule (with the exception of the present first wall cooling geometry) are quite low ($P_P/P_{TH} < 1\%$).

In Fig. 6-5(d) the pin diameter was held constant and the fuel radius was decreased as the clad thickness increased, resulting in lower heat fluxes at the larger clad dimensions. Also, the core length was increased as the fuel radius decreased so that a constant thermal output from the submodule was maintained. The primary effect of varying the clad dimension is the variation in the fuel-to-structure volume ratio. The clad thickness has only a minor effect on the clad and fuel temperatures, with these values decreasing slightly with increasing clad thickness. The clad thickness of 0.2 mm used in the reference design (as contrasted to 0.5 mm in a previous hybrid blanket study)[6-18] was considered to be a probable lower limit for this dimension. Future work should evaluate the specific structural requirements of the clad to arrive at a value for the clad thickness.

Figure 6-5(e) illustrates the results of varying the inlet coolant pressure to the submodule. This quantity strongly influences the economics, in that lower pressures result in high pumping power and high V_F/V_S (i.e., high energy multiplication). The decrease in fuel-to-structure ratio with increasing pressure is a result of maintaining a constant working stress in the pressure vessel, thus causing the pressure vessel thickness to increase in proportion to the pressure. There is an optimum coolant pressure that balances pumping power against energy multiplication, this optimum pressure being a function of the overall power plant economics. In the present study, the 20-atm pressure used in the reference design was not an optimum value, but rather was chosen to satisfy the economic constraints of $P_P/P_{TH} \lesssim 4\%$ and $M \geq 8$.

In the present point design study, the fission energy density was fixed at 100 W/cm^3. However, the thermal hydraulic code was used to examine the performance of the reference submodule over a range of power densities (that correspond to different plasma conditions or blanket energy multiplication), and these results are presented in Fig. 6-5(d). In this set of calculations, the mass flow rate was varied to hold a coolant temperature rise of 300°C through the submodule and the width of the first-wall flow annulus was varied with the mass flow to yield a constant first-wall temperature and, therefore, a constant first-wall pressure drop. The first-wall heat flux was held constant at 28 W/cm^2, although the value of this quantity may be expected to vary somewhat with the plasma conditions and, therefore, with the fission power density. The clad temperature (the limiting material constraint) increases only mildly with increasing power density as the heat transfer coefficient of the film increases with the mass flow rate. The pumping power remains

below the prescribed maximum value of 4% at twice the reference value of the power density. (Neglecting the first-wall pressure drop, it was found the P_P/P_{TH} is linearly increasing with the power density.) This result indicates an economic incentive to employ higher power densities, because the output from the module per unit of capital cost can be increased while acceptable pumping requirements are maintained.

We also evaluated the submodule performance as a function of pressure vessel radius. These calculations indicated improved economics (larger V_F/V_S and smaller P_P/P_{TH}) for the submodule as the radius of the pressure vessel increased. However, as can be seen in Fig. 6-2, as the diameter of the submodule increases, the ratio of the cross-sectional area of the submodule to the surface area of the module decreases, resulting in more void area between the submodules and therefore decreased neutronics performance. The reference value of 30 cm for the submodule diameter was chosen as a maximum value that permitted good coverage of the available module surface by the individual submodules.

This improved submodule economic performance as the pressure vessel radius increases does not take into account the effect on neutronics of an increase in first-wall thickness. The increased first-wall thickness causes degradation of the fusion neutron current and thus decreases M. However, we have not yet made neutronic calculations to assess the sensitivity of the blanket multiplication to first-wall thickness.

Summary and Recommendations

The analysis and results described in this section have demonstrated that a submodule design incorporating the important characteristics of a fast-fission hybrid blanket is feasible within the economic and engineering constraints previously outlined. In the present study, it has not been possible to fully optimize this design nor to treat it in complete engineering detail. However, the analysis was treated at a level of sophistication that included all of the significant thermal hydraulic effects in the submodule, so that further refinements of the model will not result in gross changes in the parameters characterizing the blanket performance.

The present study has indicated areas where more detailed analysis and/or design is warranted:

- We found that the proposed first-wall cooling scheme resulted in large pressure drops. The required pumping power was acceptable, but preliminary calculations have indicated that alternate designs can accomplish the cooling with a significantly smaller pumping requirement. These alternatives for first-wall cooling include use of a graphite shield in front of the submodules to intercept the beam heat load and to radiate this power to cooler regions of the blanket, and alternate first-wall cooling passages that result in lower pressure drops than the presently proposed scheme.
- Some details of the fission core design, such as minimum fuel pin pitch-to-diameter ratio and minimum clad thickness should be evaluated. Also, the core support structure requires design and inclusion in the model.

NEUTRONICS

Introduction

The neutronic design of the fast-fission blanket chosen for this mirror hybrid study is the outgrowth of a more general neutronics study of fast-fission blankets published in 1974.[6-2] The blanket model used in this earlier study had a fission zone containing 69% uranium fuel, 16% lithium and 10% structure (vol %), and a tritium breeding zone containing 86% lithium and 9% structure. Natural isotopic mixtures were used for all elements and the lithium was in the liquid form. Four forms of uranium fuels were examined: uranium metal, UO_2, UC, and UN. The best neutronic performance, independent of fuel type, was achieved with the uranium fuel zone between the tritium-breeding zone and the plasma. For blankets that produce 1.1 tritons, energy and net fissile atom production per 14.1-MeV neutron for each fuel type was: uranium metal ~ 200 MeV + ~ 2.2 atoms, UO_2 ~100 MeV + ~ 1.1 atoms, UC ~130 MeV + 1.4 atoms, UN ~120 MeV + ~ 1.2 atoms. In each case, producing the required tritium limited the fast-fission zone thickness to ~ 20 cm.

The procedure used to arrive at a consistent blanket design was:

- Assume that the nuclear performance of the blanket would be similar to the UC-fueled, lithium-cooled blanket model discussed in Ref. 6-2,
- Determine blanket material fractions by performing a thermal hydraulic and structural analysis of the blanket submodule,
- Calculate nuclear performance using the material fractions resulting from the thermal hydraulic and structural analysis.

The assumed nuclear parameters of the UC zone used to perform the submodule thermal hydraulic and structural analysis are summarized in Table 6-7.

Blanket Model and Calculational Method

The model used to calculate neutronic performance of the blanket is a three-zone spherical annulus surrounding a spherical volume source of isotropic 14-MeV neutrons. The spherical source has a radius of 3.2 m and the inner blanket radius is 4 m.

The three blanket zones consist of a structural first wall (0.5 cm) followed by the fission zone and then by the tritium breeding zone. The present reference blanket has the material volume fractions listed in Table 6-8.

The atom (or molecular) densities for each material (at 10 vol%) is listed in Table 6-9.

The nuclear performance of the reference blanket was calculated with the same Monte Carlo neutron transport code (TART)[6-19] and cross-section library (ENDL)[6-20] that were used in the blanket study quoted earlier. The TART calculations were run with a sample size of 2500 source neutrons, and resulted in standard deviations between 1 and 2%.

Performance of Reference Blanket

With the type and vol% of materials in the fission and tritium-breeding zones specified, the thickness of these zones was varied to achieve the required tritium breeding ratio of 1.1 tritons per DT neutron. Leakage of DT neutrons out injection and direct energy converter

Table 6-7. Nuclear parameters used in thermal hydraulic and structural analysis of submodule.

Blanket energy multiplication	9.2 (130/14.1-MeV neutron)
Net fissile atom production	1.4 atoms/14-MeV neutron
Product of UC volume fraction (V_f) times thickness (t)	13.8 cm
Power profile P (t)	$\sim P_{MAX} \quad 1 - \frac{V_f \cdot t}{18.3}$
Peak to average power density	1.8
Maximum power density in UC	$\sim 1.1\ (m^{-1}) \times WL$, where WL = wall loading (energy current (MW/m^2) of D-T neutrons through first wall (14.1 MeV per neutron))
Power density in structure	.5 to 10% of UC power density.
Neutron multiplication of blanket without fusion source (K)	0.28

Table 6-8. Materials in reference blanket zones (vol%).

Material	First-wall zone	Fission zone	Tritium-breeding zone
Stainless steel	100	8.6	8.6
UC		54	
C			45
$^6LiAlO_2$			10

Table 6-9. Atom (or molecular) densities for each material (at a volume fraction of 1.0) (cm^{-3}).

SS	UC	C and $^6LiAlO_2$
$N(Fe) = 6.04 \times 10^{22}$	$N(^{235}U) = 0.0202 \times 10^{22}$	$N(C) = 8.02 \times 10^{22}$
$N(Ni) = 0.081$	$N(^{238}U) = 2.79$	$N(^6LiAlO_2) = 2.33$
$N(Cr) = 1.76$	$N(C) = 2.81$	

ports is estimated to be 5%; therefore, the tritium-breeding ratio drops to 1.05. This tritium-breeding ratio is achieved with a fission-zone thickness of 20 cm and a tritium-breeding zone thickness of 60 cm. The neutronic parameters for this blanket are given in Table 6-10.

The local nuclear performance of the blanket, namely, energy multiplication of the DT neutron energy (M), tritium breeding (T) and net fissile breeding (Pu) reactions per DT neutron, is quite sensitive to both the thickness of the fission zone and the ratio of fuel to structural

Table 6-10. Neutronic parameters for reference blanket.

Energy multiplication (M)	8.51 (120 MeV per 14.1-MeV neutron)
Tritium-breeding ratio (T)	1.11 tritons per 14.1-MeV neutron
Net fissile breeding ratio (Pu)	1.29 [$^{238}U(n,\gamma)$ - $^{235}U(n,f)$ - $^{235}U(n,\gamma)$] per 14.1-MeV neutron
Ratio of ^{238}U fission to total fission	0.857
Peak to average fuel power density	~1.5
Fission neutron multiplication with no source (k)	~0.28

material (V_f/V_s). The dependence of performance on these two blanket parameters is shown in Fig. 6-6. Note that as the fuel-to-structure ratio is varied, the thickness of the fission zone must also be varied to maintain the desired tritium-breeding ratio. This optimization was only done for the reference case (V_F/V_S = 6.29), and resulted in requiring a fission-zone thickness of 20 cm.

Operating Parameters of Reference Blanket

The maximum energy current of fusion neutrons crossing the first wall (referred to as a wall loading) is estimated to be 84 W/cm^2. This estimate is based on a fusion power level of 210 MW and a first-wall radius at 4 m. For a wall loading of 84 W/cm^2, the operating parameters of the reference blanket are listed in Table 6-11.

The average blanket wall loading is ~21 W/cm^2. Therefore, the blanket average operating parameters for the blanket are one-fourth those listed above.

After allowing for a 5% neutron streaming loss, blanket output at start of life is:

- Thermal power = 1360 MW
- Net fissile production rate = 1140 kg(Pu)/year

Exposure Effects

The nuclear and operating parameters of the reference blanket just discussed are for a new blanket. While no exposure-dependent calculations were made for this reference blanket, the analysis of its predecessor[6-2] was used to make an estimate of how this blanket's performance will change with exposure. The estimate is graphically displayed in Fig. 6-7.

At start of life, the ratio of fissile production [$^{238}U(n,\gamma)$] to fissile-consumption [$^{235}U(n,f+n,\gamma)$] is 14 to 1. The initial buildup rate of fissile material is 0.005 atoms per year. In response to the buildup of fissile material, blanket energy multiplication (M) and tritium breeding (T) increase while net fissile breeding declines. If the fuel is left in place, both M and T peak at an integrated wall loading of ~20 MW-years/m^2, with M at about 4 times its initial value and T at about 2 times its initial value. At this point, net fissile fuel production has dropped to nearly zero (a fissile breeding ratio near 1.0). The ratio of plutonium to the initial number of uranium atoms also peaks at about this exposure and is ~7.5%. Even at this point, the blanket is still very subcritical; the fission neutron multiplication (K) is estimated to be 0.73.

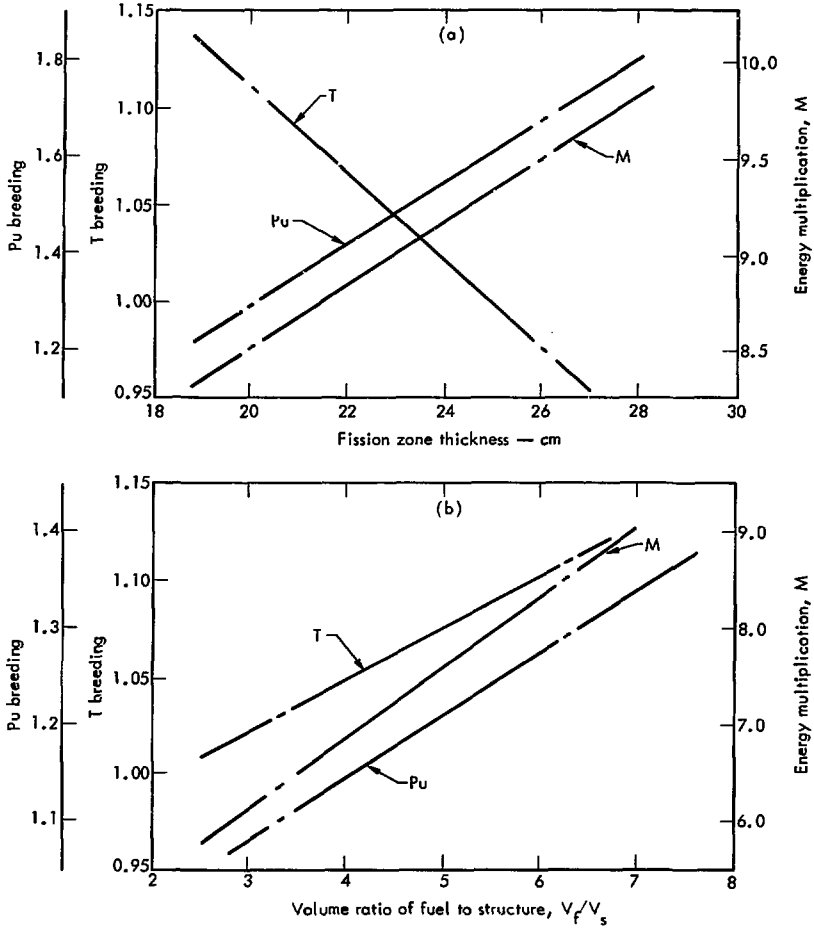

Fig. 6-6. Blanket nuclear performance vs (a) fission zone thickness (V_F/V_S = 6.29) and (b) volume ratio of fuel to structure (20-cm fission-zone thickness).

The equilibrium average enrichment and initial zone enrichments that are best for a fast-fission blanket are still open questions. Before such questions can be answered, we must make detailed analyses of the fuel cycle. The costs of reprocessing and refabrication as well as the values of electric power and fissile fuel will affect how best to manage the blanket.

Table 6-11. Operating parameters for reference blanket (wall loading = 84 W/cm^2).

UC zone average power density	34 W/cm^3
UC fuel average power density	64 W/cm^3
UC fuel peak power density	96 W/cm^3
Average fractional fission rate	0.0022 fissions per U atom per year
Peak fractional fission rate	0.0032 fissions per U atom per year
Average fractional buildup rate of fissile atoms	0.0049 ($^{238}U(n,\gamma)$ - $^{235}U(n, \text{fission}) + n\gamma$) reactions per U atom per year
First-wall 14-MeV neutron current	3.7×10^{13} $n/cm^2 \cdot s$
First-wall neutron flux	7.9×10^{14} $n/cm^2 \cdot s$ (2.1×10^{14} > 1 MeV)

This blanket is by no means optimized. For example, the thickness of the fission zone was fixed by the requirement to breed 1.1 tritons per fusion at start of life. However, as shown in Fig. 6-7, the tritium breeding ratio increases with exposure. We can trade excess tritium breeding for higher fissile breeding and energy multiplication by making the fission zone thicker. Referring to Fig. 6-6, we see that increasing the fission-zone thickness from 20 cm to 26 cm increases energy multiplication by 12% and fissile breeding by about 30%, while reducing tritium breeding by about 12%.

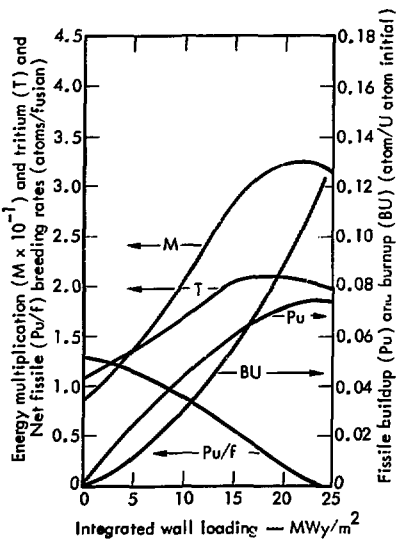

Fig. 6-7. Blanket performance vs exposure.

More neutronic analyses of this blanket are needed to optimize its performance and to examine the effects of the reduction of effective ^{238}U capture cross section due to resonance effects, nonspherical geometry, source neutron energy spread, DD fusion neutrons, and uncertainty in nuclear data. None of these is expected to have a large effect, but they should be checked. New and more detailed exposure analyses are also needed. Shielding calculations must be performed so that optimum shield designs can be developed. Accident analysis must also be performed to determine if accidental reconfiguration is ever a potential problem.

BLANKET AND FUEL MANAGEMENT

The blanket consists of four identical quadrants, each quadrant being composed of a group of individual modules. The

blanket management scheme selected in the present study is based on the use of five quadrants of modules, where at any given time four quadrants would be in the blanket, and the fifth quadrant would be out of the blanket for servicing and refueling. A 1-year interval was selected as the blanket cycle time; that is, once every year the plant would be shut down and a quadrant would be removed from the blanket and replaced by the quadrant that had been out of the blanket the previous year. In this fashion, each quadrant of modules would undergo a cycle consisting of 4 years in and 1 year out of the blanket.

Another important consideration in the blanket analysis is the fact that the neutron current from the plasma varies along the length of the module because of the varying distance from the blanket to the plasma. Thus, the exposure (integrated 14-MeV neutron current) of any given module is not only a function of the time it has been in the reactor but also varies spatially within the module. The exposure effect has important consequences, in that the energy multiplication, burnup, and enrichment (which are functions of exposure, as explained previously) become spatially dependent quantities. It is therefore possible to conceive of various fuel management schemes (moving of fuel bundles within the module during the time that the module is out of the blanket) that achieve different types of exposure-dependent performance from the blanket.

The fuel management scheme chosen for the present study is as follows: During the 1-year interval that a given quadrant is out of the blanket, the bundles that have reached maximum exposure are removed and reprocessed. The remaining bundles are repositioned in the module so that those with the highest exposure are in the region of largest neutron current. The fuel load is then completed by adding new, unexposed bundles to replace those that were removed. This particular scheme minimizes the time required to extract plutonium from the blanket because the highest-exposure (highest-enrichment) bundles are always placed in the position where they will reach maximum exposure in a minimum length of time. The penalty paid in this scheme is that a power gradient is present along the length of the module (peak to average power ~6), a circumstance which could be avoided with other management schemes.

For the blanket and fuel management analysis, the plasma was assumed to be a point neutron source, and each blanket quadrant a half cone. The geometry is shown in Fig. 6-8. The 14-MeV neutron current perpendicular to the blanket ($J_\perp$) then varies inversely as the cube of the distance from the source (see Fig. 6-8),

$$J_\perp \sim \frac{1}{\rho^3} .$$

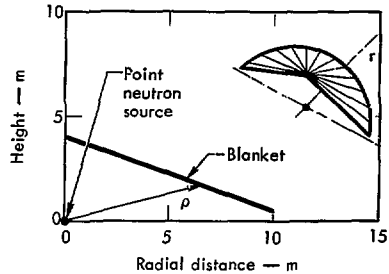

Fig. 6-8. Plasma blanket geometry for the fuel-management model.

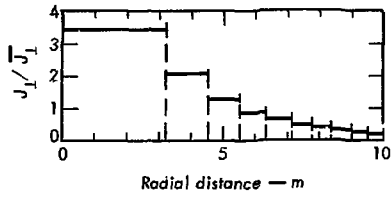

Fig. 6-9. 14-MeV neutron current distribution.

Each blanket quadrant was divided into 10 radial regions of equal area, and each region was characterized by an average neutron current, as shown in Fig. 6-9. The analysis was performed with a code that was written to evaluate the important blanket parameters as a function of time using the blanket-fuel management scheme described above.

The blanket multiplication, $\overline{M}$, is defined as

$$\overline{M}(t) = \int \frac{M(r, t)\ \left[J_\perp(\vec{r})/\bar{J}_\perp\right]\ dA_{BL}}{A_{BL}},$$

such that $P_{BL} = \overline{M} \cdot P^0_{FUS}$,

where P^0_{FUS} is the fusion neutron power, P_{BL} is the blanket power, $M(r, t)$ is the time (t) and spatially (r) dependent energy multiplication, $\bar{J}$ is the average neutron current, and A_{BL} is the blanket area.

As an example calculation, we use a maximum burnup of 3%, a blanket cycle time of 1 year, and a peak fusion-neutron current of 4.4×10^{13} n/cm^2/s (1 MW/m^2). The resulting history of the blanket multiplication for a 40-year plant lifetime is shown in Fig. 6-10. The blanket is started at time zero with all fuel bundles unexposed, having a (local) multiplication of 8.5 as stated previously. The blanket multiplication of 8.1 at start of life results

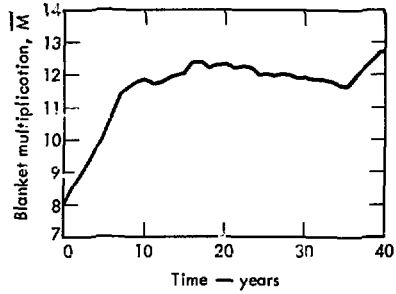

Fig. 6-10. Blanket energy multiplication.

from source neutron losses through the mirrors and injector ports. The multiplication increases monotonically for about 10 years as the blanket enriches in plutonium, and then comes to an approximate steady state as exposed bundles are removed from the blanket and new bundles are introduced. The blanket has a time-averaged multiplication of 11.6 over the 40-year plant lifetime.

The plutonium production rate is shown in Fig. 6-11. The plutonium production is evaluated from the enrichment of the bundles that have reached maximum burnup when they are removed from

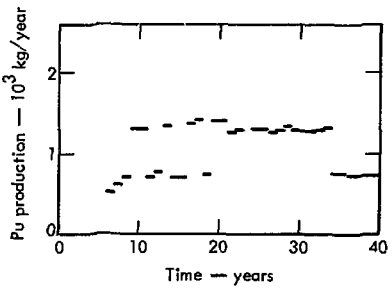

Fig. 6-11. Plutonium production rate (peak first-wall loading = 1 MW/m^2.

the module for reprocessing. During the plant lifetime, the blanket produces an average of ~ 1200 kg of plutonium per year. Over the 40-year plant lifetime, the net production is 4.7×10^4 kg of plutonium, a quantity that includes all of the plutonium in the blanket at the end of the plant life.

The blanket reprocessing schedule is shown in Fig. 6-12. The first bundles are removed after 4 years of plant operation. After the initial enrichment period, approximately 5% of the blanket fuel bundles are reprocessed each year, with the result being an average bundle lifetime of about 20 years.

The final plasma calculations resulted in a peak fusion-neutron wall loading of 0.84 MW/m^2. By combining this wall loading with a 0.8 plant duty factor and a recommended plant lifetime of 30 years, we found that the time-average blanket multiplication of 12 would be obtainable with a 5% burnup and a 1-year blanket cycle time. The plutonium production was calculated to be 2.09×10^4 kg in the 30-year plant lifetime, or an average of 690 kg/yr.

The peak bundles reach maximum exposure after 15 years, and 17.5% of the blanket requires reprocessing before the end of the plant life. The average UC burnup when removed for reprocessing was calculated to be 4.0%. Although the maximum burnup was set at 5%, a lower attained value results because a bundle must be removed from the module if its burnup will be greater than 5% at the next time the module is removed from the blanket. The average attained burnup can be increased by decreasing the blanket cycle time; however, decreasing the

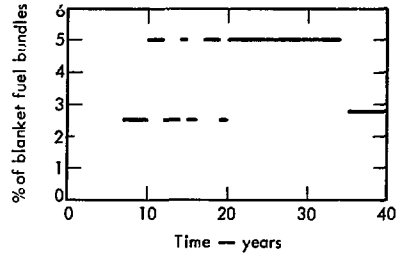

Fig. 6-12. Reprocessing schedule for blanket fuel bundles.

blanket cycle time results in a lower duty factor for the power plant. The trade-off between attained burnup and blanket cycle time has not been evaluated. A cycle time of 1.0 years was chosen as being an (apparently) reasonable value.

Cost Analysis of Fuel Cycle

The fuel cycle analysis was conducted using the methodology presented in Ref. 6-20 and using fuel cycle data from Refs. 6-21, 6-22, and 6-23. The fuel cycle analysis is divided into the 11 components listed in Table 6-12. These components are classified as

- Direct costs (expenses for materials and services to put the fuel into a form from which energy can be extracted from it), and
- Indirect costs, (the time value of money, i.e., interest, taxes, profits).

The direct costs, Components 1-7 in Table 6-12, are evaluated in terms of cost per kg of material for component j from the equation

$$(\$/\text{kg of mat'l})_j = f_j w_j c_j, \quad j = 1, 7,$$

where f_j is the process loss factor, w_j is the nuclear weight factor which represents

the net consumption or production of nuclear material, and c_j is the cost factor in dollars per kg of material.

The indirect costs, Components 8-11 in Table 6-12, are evaluated from the equation

$$J_j = Y_j it, \qquad j = 8, 11,$$

where J_j is the indirect cost of component j, Y_j is the debt of component j, i is the interest rate, and t is the time interval.

The parameters that characterize the present blanket, and that are needed for the fuel cycle analysis, are shown in Table 6-13. The uranium load is 8.2×10^5 kg in the reactor plus 2.05×10^5 kg for the blanket quadrant that is out of the reactor for servicing. The peak fusion neutron wall loading of .84 MW/m^2 and a 0.8 plant duty factor for 30 years results in a net energy output of 1.29×10^{11} kWh. The plutonium production and average uranium carbide burnup values were obtained from the fuel management calculation described earlier.

The fuel cycle costs, by component, are presented in Table 6-14. The

Table 6-12. Components of fuel cost.

Component	Direct costs	Indirect costs
1. {Natural U, D_2, Li^6AlO_2}	Initial ^{235}U, ^{238}U, D_2, Li	
2. {Depleted U, D_2, Depleted Li^6AlO_2}	Recovered ^{235}U, ^{238}U, D_2, Li	
3. {Pu, T_2}	Initial Pu, T_2	
4. Pu	Recovered Pu, T_2	
5. {T_2, UC, Li^6AlO_2}	Fabrication costs	
6. UC	Reprocessing costs	
7. Depleted UC	Shipping costs	
8. {UC, D_2, Li^6AlO_2}		Those associated with ^{235}U, ^{238}U, D_2, Li
9. T_2 (initial)		Those associated with Pu, T_2
10. {UC, Li^6AlO_2}		Those associated with fabrication costs
11. Depleted UC		Those associated with reprocessing and shipping

Table 6-13. Power plant parameters for the fuel cycle analysis.

Uranium load	1.03×10^6 kg initial
^6Li load	1.13×10^4 kg
D_2 consumption	6.23 kg/yr
Excess T_2 breeding	1.9 kg/yr
Average UC burnup	1.2%
Average ^6Li burnup	4.6%
Blanket lifetime	30 years
Average Pu enrichment at end of blanket life	0.0203 atom Pu/atom U initial
Plant electrical output: 30 years; 0.8 duty factor	1.29×10^{11} kWh

Table 6-14. Fuel cycle costs.

Component	Cost (mills/kWh)
1. {Natural U, D_2, Li^6AlO_2}	0.213
2. {Depleted U, D_2, Depleted Li^6AlO_2}	-0.098
3. {Pu, T_2}	0.105
4. {Pu, T_2}	-3.740
5. {UC, Li^6AlO_2}	0.400
6. UC	0.310
7. Depleted UC	0.039
8. {UC, D_2, Li^6AlO_2}	0.891
9. T_2 (initially)	0.002
10. {UC, Li^6AlO_2}	1.258
11. Depleted UC	0
Total:	-0.62

analysis resulted in a net fuel cycle cost of -0.62 mills/kWh, the negative value resulting from the large revenues generated by the plutonium breeding. The breakdown of the component costs is presented, with comments, in Table 6-15.

The blanket serves two purposes: energy multiplication and plutonium production. The fuel management scheme can be chosen to emphasize one or the other, or possibly a compromise between these two extremes. In the present point design study, the management schedule selected is a compromise between the two. The merits of various fuel management schemes are areas for future analysis.

SAFETY DISCUSSION

The present preliminary design has demonstrated encouraging results for a fusion-fission hybrid reactor from the standpoint of engineering feasibility and economics. The third important aspect of a nuclear power plant that must be evaluated is the environmental/safety question associated with the possible release of radioactive materials.

The release of significant amounts of radioactivity from a fission core is generally acknowledged to occur through melting of the core when the energy generated in the fuel exceeds the heat-removal capacity of the core cooling

Table 6-15. Breakdown of unit fuel cycle costs and nuclear parameters.

Component		Process loss factor, f_j	Nuclear weight factor, w_j	Cost factor, c_j ($/kg)	Debt of component, Y_j ($\times 10^{-6}$)	Interest rate, i	Time interval, t (yrs)	Comments
1.	Natural U	1.015	1.0	23.46				1.5% for fabrication
	D_2	1.0	1.0	60				D_2 consumption of 6.23 kg/yr.
	Li^6AlO_2	1.015	1.000	1000				1.5% for fabrication
2.	Depleted U	0.99	0.988	9.86				U is 0.51% in ^{235}U when removed at 1.8% burnup; 1% reprocessing loss
	D_2	1.0	0					
	Depleted Li^6AlO_2	0.99	0.954	1000				
3.	P_u	1.0	0					No initial P_u enrichment
	T_2	1.0	1.0	1.20				Initial T_2 load of 2.32 kg
4.	Pu	0.99	0.0203	0.20				Value chosen as typical of a power reactor economy where P_u used to fuel light-water reactors (LWR's)
	T_2	1.0	1.87 kg/yr	1.20				Excess T_2 production at breeding ratio of 1.2
5.	UC	1.0	1.0	50				Typical of gas-cooled fast reactor (GCFR) carbide blanket
	Li^6AlO_2	1.0	1.0	10				Assumed cost
6.	UC	0.99	0.882	$40/kg				Typical of GCFR carbide blanket: 1% loss; 1.8% burnup
7.	Depleted UC	1.0	0.882	$5/kg				
8.	UC	24.65	0.10	30				
	D_2			0				Paid out of current revenues
	Li^6AlO_2	13.50	0.10	30				
9.	T_2(initial)	2.78	0.10	1				Assume 1 yr to retire debt
10.	UC	52.02	0.10	30				
	Li^6AlO_2	1.88	0.10	30				Includes 3.5×10^5 kg C @ $5/kg
11.	Depleted UC			0				Paid out of current Pu revenues

system. In pure-fission reactors, this thermal overload occurs primarily via reactivity insertion or loss of coolant. The approach taken to prevent core melting has been to engineer safety systems into the reactor that will prevent thermal overload, i.e., scram and emergency core-cooling systems.

Preserving the structural integrity of the hybrid blanket during an abnormal operating situation may be a less severe problem than in a pure-fission reactor because

- The hybrid blanket is designed to be subcritical,
- The power density in the fission zone of the blanket of the present point design is an order of magnitude lower than in proposed fast-breeder reactors.

There is no possibility of a thermal overload due to a criticality accident. Therefore, the primary safety consideration is the loss of coolant accident (LOCA).

The design basis accident (DBA) selected for the hybrid blanket was a helium depressurization of 1 atm and loss of flow with a simultaneous loss of the neutron source from the plasma. (It is felt that any major disturbance in the normal plant operating conditions, such as an LOCA, will or can be made to quench the plasma.) Thus, insuring blanket integrity in a hybrid LOCA requires the removal of fission-product afterheat.

In the present study, we rely on engineering safeguards to remove afterheat from the blanket in the event of a DBA. Calculations have shown (p. 49ff.) that the 5-W/cm^3 afterheat power in the fuel can be removed and acceptable temperatures can be maintained in the blanket by circulating helium at 1 atm through the modules. In addition, after a loss of coolant, at least 5 min is available before the emergency cooling must commence to prevent clad melting.

The emergency blanket cooling would be provided by redundant or auxiliary cooling equipment, although a specific hardware configuration has not been proposed in the present study. We anticipate that the operation of the emergency coolant circulator system can be insured with the degree of reliability necessary to license the plant, because the requirement for ambient helium delivery to the blanket within 5 min following loss of coolant does not place stringent performance characteristics on the emergency cooling system.

While our preliminary LOCA analysis indicates that the conceptual blanket design developed for the hybrid mirror reactor can be safe under accident conditions, no definitive conclusions can be drawn until an in-depth safety analysis is performed. Part of our future work on hybrids will be to address in detail the major safety questions of this and other, future conceptual designs.

The low afterheat power levels present in the hybrid blanket suggest that a blanket configuration could be devised that would be passively cooled (i.e., via conduction, free convection, and radiation) in the event of a LOCA. A design of this type would preclude thermal overload of the blanket and thus would significantly reduce the possibility of a radioactive release. The result would be a much more environmentally attractive power plant than one that relies on active systems to prevent thermal overload of the core.

We feel that the advantages of a blanket that can passively remove its afterheat are so significant that a major thrust of the conceptual hybrid study should be towards examining the performance of pas. ively cooled blanket designs. This may well mean a major reconfiguration of the presently proposed submodule design; inevitably, some economic penalty will be paid to incorporate the passive-cooling capability into the blanket. A hybrid reactor that is nearly free from the possibility of a radioactive release would overcome many of the technical problems that have delayed the introduction of the fast-breeder reactor into the power economy. The feasibility of passive cooling will depend on the economic and environmental tradeoffs involved.

CONCLUSIONS

The conceptual blanket developed for this mirror hybrid reactor study appears capable of meeting the thermomechanical and nuclear requirements in a compatible manner. This blanket conforms to the plasma and coil geometries, can be routinely replaced, contains necessary structure, can be cooled, and gives acceptable nuclear performance.

The major features of this blanket are:

- Modularization for accessibility
- Ceramic fuels (UC and $LiAlO_2$)
- Natural uranium fuel
- Helium cooling
- Stainless steel structure and cladding
- Maximum of ^{238}U fission.

While we believe this blanket to be viable, it is by no means a complete design, nor has it been optimized.

The blanket chosen for this study uses only one of the many possible combinations of materials and geometric configurations deserving investigation. For example, a fast-fission blanket utilizing the same configuration could have metallic uranium instead of uranium carbide and a liquid-metal coolant instead of helium. The module-submodule blanket arrangement can also be applied to a thermal fission blanket. Figure 6-13 depicts one such application – the hydride-moderated, fission-lattice concept developed by Maniscalco.[6-5] The graphite-moderated lattice developed by Leonard and Wolkenhauer could also be used.[6-3] Fissile and/or fertile molten salt blankets are also being investigated (Fig. 6-14).

In addition to the material and neutronic options, different overall blanket configurations should also be investigated. One such alternative blanket configuration, consisting of many tubes surrounding the

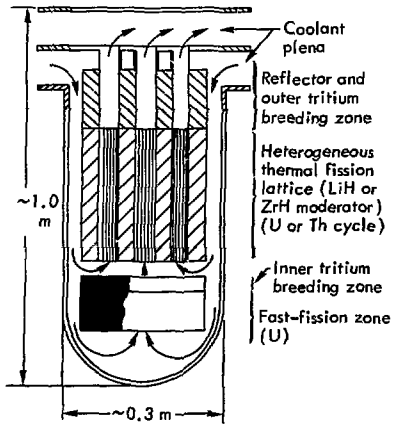

Fig. 6-13. Thermal fission blanket submodule.

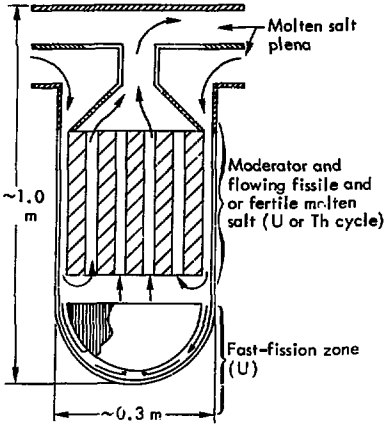

Fig. 6-14. Molten salt blanket module.

plasma, could make on-line refueling possible. Figures 6-15 and 6-16 show two possible tubular-blanket arrangements. The first (Fig. 6-15) shows schematically how a tubular blanket might conform to the Yin-Yang minimum-B coil geometry. By comparison, the second (Fig. 6-16) shows how a much simpler tubular-blanket arrangement could be achieved by using

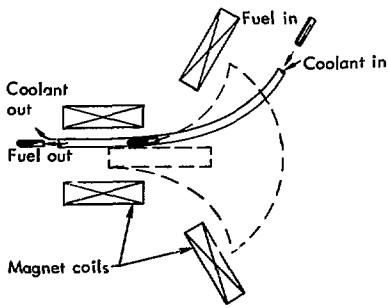

Fig. 6-15. Tubular hybrid blanket surrounding a minimum-B mirror plasma.

the simple mirror geometry. Unfortunately, a plasma confined in a simple mirror is MHD unstable; therefore, a stablizing mechanism must be invented before the simple mirror could be used.

We plan to continue our work on these and other conceptual hybrid blanket designs so we may develop a better understanding of the options and tradeoffs available to us.

REFERENCES

6-1. J. D. Lee, "Neutronics of Sub-Critical Fast Fission Blankets for D-T Fusion Reactors," in Proc. 7th Conf. Intersociety Energy Conversion Engineering, 1972 (American Chemical Society, 1972), p. 1294.

6-2. J. D. Lee, "Neutronic Analysis of a 2500 MW_{th} Fast Fission Natural Uranium Blanket for a DT Fusion Reactor," in Proc. First Topical Meeting on the Technology of Controlled Nuclear Fusion, 1974 (San Diego, CA, 1974), CONF-740402-P1, vol. 1, p. 233; also Lawrence Livermore Laboratory Rept. UCRL-75304 (1974).

6-3. B. R. Leonard, Jr. and W. C. Wolkenhauer, "Fusion-Fission Hybrids: A Subcritical Thermal Fission Lattice for a DT Reactor," in Proc. on Technology of Controlled Thermonuclear Fusion, 1972 (Univ. of Texas, 1972); also, Pacific Northwest Laboratories Rept. BNWL-SA-4390 (1972).

6-4. B. R. Leonard, Nucl. Technol. 20 (1973).

6-5. J. A. Maniscalco and L. L. Wood, Advanced Concepts in Fusion-Fission

Hybrid Reactors, Lawrence Livermore Laboratory Rept. UCRL-75835 (1974).

6-6. Laszlo N. Lontai, Study of A Thermonuclear Reactor Blanket with Fissile Nuclides, MS thesis, Technical Report No. 436, Massachusetts Institute of Technology (1965).

6-7. T. A. Parish and E. L. Draper, "Neutronic and Photonic Analysis of Fusion Reactor Blankets Containing Natural Uranium," in Proc. First Topical Meeting on Technology of Controlled Nuclear Fusion, 1974 (San Diego, CA, 1974), CONF-740402-P1, vol. 1, p. 256.

6-8. L. M. Lidsky, "Fission-Fusion Symbiosis; General Considerations and a Specific Example," in Proc. Nuclear Fusion Reactors Conference, 1969 (Culham, England, 1969), paper 1.2.

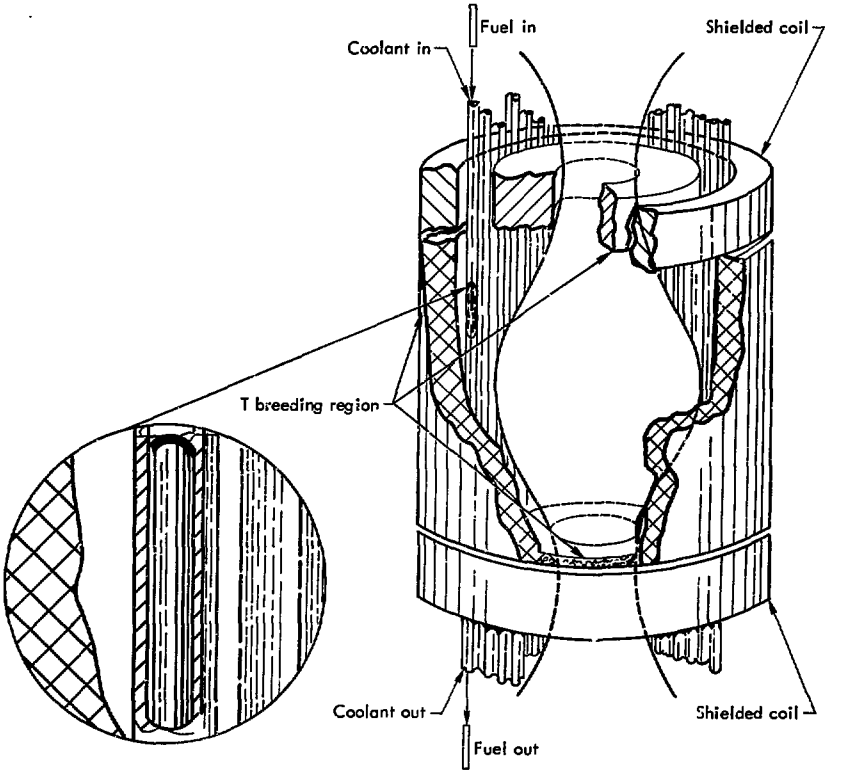

Fig. 6-16. Tubular blanket around a simple mirror plasma.

6-9. W. C. Wolkenhauer, B. R. Leonard, Jr., A. M. Sutey, and R. W. Moir, "Conceptual Design of a Fusion-Fission Hybrid Reactor Based on a Mirror Fusion Reactor with a Subcritical Gas Cooled Fission Blanket," in Proc. First Topical Meeting on the Technology of Controlled Nuclear Fusion, 1974 (San Diego, CA, 1974), CONF-740402-P1, vol. 1, p 238.

6-10. W. C. Wolkenhauer, C. W. Stewart, R. W. Werner, and J. D. Lee, "Some Safety Considerations of Hybrid Reactors in Comparison with Fission and Fusion Reactors," in Proc. First Topical Meeting on the Technology of Controlled Nuclear Fusion, 1974 (San Diego, CA, 1974), CONF-740402-P1, vol. 1, p. 588.

6-11. R. W. Conn et al., "Major Design Features of the Conceptual DT Tokamak Power Reactor, UNMAK-II," in Proc. Fifth Conf. Plasma Physics and Controlled Nuclear Fusion, 1974 (IAEA, Tokyo, Japan, 1974), IAEA-CN-33/GI-2 (also UWFDM-114).

6-12. J. R. Stanbridge, H. M. Carruthers, B. A. Keen, and H. A. Shotter, Design of Stainless Steel Blanket Cells for a Fusion Reactor, Culham Laboratory Rept. No. CLM-R127 (1974).

6-13. R. H. Simon, J. B. Dee, and W. I. Morita, "Gas-Cooled Fast Breeder Reactor Demonstration Plant," in Proc. ANS Topical Meeting on Gas Cooled Reactors: HTGR and GCFBR, 1974 (Gatlinburg, TN, 1974), CONF-740501, p. 336.

6-14. W. M. Rohsenow and J. P. Hartnett (Eds.), Handbook of Heat Transfer (McGraw-Hill, 1973), Chapter 7.

6-15. M. M. El-Wakil, Nuclear Energy Conversion (International Textbook, 1971), Chapter 7-4.

6-16. S. Glasstone and A. Sesonske, Nuclear Reactor Engineering, (D. Van Nostrand Co., 1963), p. 101.

6-17. V. E. Schrock (Ed.), "Heat Transfer in Rod Bundles," in Proc. Winter Annual Meeting of the ASME, 1968.

6-18. A. M. Sutey and C. W. Stewart, A Thermal Hydraulic Analysis of the Pacific Northwest Laboratory Fusion-Fission Hybrid Reactor Concept, Battelle Pacific Northwest Laboratories Rept. BNWL-B-283 (1973).

6-19. E. Plechaty and J. Kimlinger, Lawrence Livermore Laboratory, Internal document UCIR-522 (1971). Readers outside the Laboratory who desire further information on LLL internal documents should address their inquiries to the Technical Information Department, Lawrence Livermore Laboratory, Livermore, California 94550.

6-20. R. J. Howerton, R. J. Doyas, T. C. Michels, and S. T. Perkins, An Integrated System for Production of Neutronics and Photonics Calculational Constants, Lawrence Livermore Laboratory Rept. UCRL-50400, vol. 4 (1971).

6-21. Guide for Economic Evaluation of Nuclear Reactor Plant Designs, NUS Corp. Rept. NUS-531 (1969).

6-22. Reactor Fuel Cycle Costs for Nuclear Power Evaluation, AEC Rept. WASH-1099 (1971).

6-23. A. L. Lotts, T. N. Washburn, and F. J. Homan, FABCOST9, A Computer Code for Estimating Costs for Rod-Bundle Fuel Elements, Oak Ridge National Laboratory Rept. ORNL-4287 (1972).

7. Magnet Design

SUPERCONDUCTING COILS

The basic requirement for the coil design for the minor hybrid fusion-fission reactor is that it produce a minimum-|B| field configuration throughout the plasma volume. It must also provide vacuum mirror ratio $R_{vac} = 3.5$ and a nearly circular plasma cross section at the midplane with a radius $r_p = 3.5$ m. A Yin-Yang coil configuration (see Fig. 2-1) was chosen over a Baseball coil for two reasons: it affords superior access to the plasma region for fuel injection, and it produces the mirror field with much less wasted magnetic field. The coil is similar to the design of Moir and Taylor.[7-1]

Since the relative separation between arcs at the mirrors is nearly the same here as in the FERF coil,[7-2] we use the same factor as in that design to estimate the ratio of the maximum field strength at the conductor to that at the mirror. Thus, because the field at the mirror in the present design is $B_m = 6.8$ T, we expect a maximum of $B_{cond} = 8.1$ T at the conductor. This maximum field is well within the range where niobium-titanium superconductor can be used. However, to insure complete coil safety, the superconductor current density must be limited to allow operation within the cryostatic stability regime. The superconductor must also be high current, perhaps 20,000 A or more, to reduce inductance and thereby limit coil voltage and stored energy. A high-current conductor will also simplify coil construction. An effort is now underway at LLL to produce a fully stabilized superconductor similar to that needed for the hybrid magnet system.

The coil conductor is made up entirely of arcs of circles, all lying in either a vertical or a horizontal plane, and each with an included angle of 180°. The cross section of the coil is tailored to allow extraction of the blanket modules. At the turnarounds, the cross section is elongated to avoid an unnecessarily high field at the conductor.

The magnetic induction, B, was calculated using the computer code MAFCO.[7-3] Each of the Yin-Yang pair of coils was simulated by 50 filaments in the main coil and 14 filaments in the auxiliary coils. [The auxiliary coils guide the field lines (and the escaping plasma) out through the narrow slot in the shielding and into the direct energy converter.] Figure 7-1 shows the filaments and a cross section of the main coil. The maximum B at the conductor, $B_{cond} = 8.1$ T, occurs at the conductors on the face of the coil nearest the plasma at the mirror. When $B_m = 6.8$ T

at the mirror, and B_{vac} = 1.94 T at the center, the total current in each half coil is 6.41×10^7 A-turns. The average length per turn is 84.1 m; therefore, the product of current times length is 1.08×10^{10} A·m for the complete coil assembly.

Figure 7-2 shows some magnetic field lines and the locations and values of the maximum (mirror) and minimum field strengths. By symmetry, the right-hand half of the figure gives the top view of the left-hand half, and vice versa. The mirror ratio in the field direction, $R_{\parallel}$, varies from $R_{\parallel}$ = 3.50 on the central line to $R_{\parallel}$ = 3.15 on the outermost line through the plasma. The radial well depth is $R_{\perp}$ = 1.09.

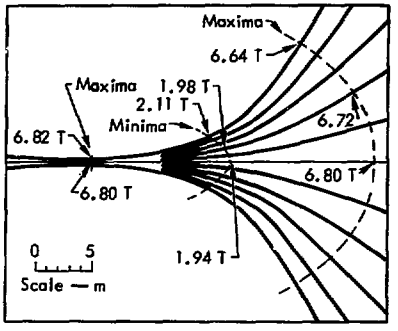

Fig. 7-2. Maximum and minimum B-values on the magnetic field lines.

STRUCTURE

The coil support structure for the Yin-Yang coil pair used in this hybrid design differs in several ways from the coil structures developed in previous mirror fusion design studies. The hybrid reactor concept permits much lower (~1/2 to 1/3) magnetic field strengths because the fusion power density in the plasma, which is proportional to B^4, is much less than could be used in an economically viable pure-fusion reactor. Since the magnetic forces scale approximately with the second power of the magnetic field strength, the hybrid concept greatly reduces (~1/4 to 1/9) the magnitude of the forces that the coil support structure must contain.

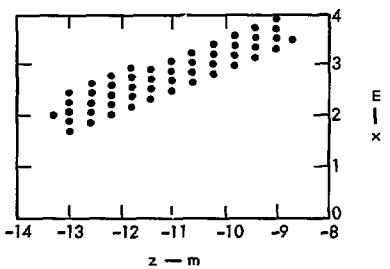

Fig. 7-1. Section through main coil, showing the conductors used in calculating the magnetic field, for B_{cond} = 8.1 T, B_m = 6.8 T.

The use of selective leakage* could further simplify design of the coil structure. In the present design, the entire volume — defined by the extension of all the field lines in the plasma confinement volume through the mirror, magnetic expander, and direct energy converter regions — must be totally devoid of any structural members. This "open mirror" design reduces plasma physics

*By selective leakage, we mean that the plasma that leaks out the ends of the magnetic mirror can be biased by weakening the magnetic field locally so as to make the leakage spatially "selective".

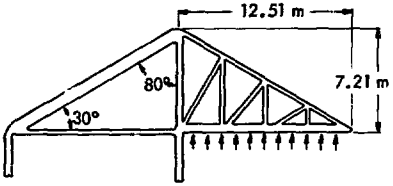

Largest truss subassembly

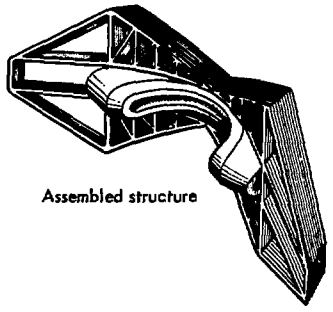

Assembled structure

Fig. 7-3. Coil support structure.

uncertainties; however, it greatly increases the cost and complexity of the coil support structure.

For this study, we developed a laminated clamp structure to support the coils. This structure consists of a large number of separately designed truss subassemblies that together form the laminated clamp shown in Fig. 7-3. This structure contains the magnetic forces by balancing the repulsive forces distributed across the upper and lower winding of each mirror coil against one another. (These primary magnetic forces are the only ones considered in detail in this study.)

A first-order structural analysis of the coil support structure was developed in order to determine its structural feasibility and cost. Because of the preliminary nature of this study, the structural model was not developed with the intention of providing a detailed analysis of a "real" structure, but rather to provide an approximate indication of what a carefully designed structure (with optimized geometry and structural members) might achieve. Each truss subassembly was separately designe fit on a simplified model of the coil windings. Each structural member of the truss subassembly was individually designed, whether in tension, compression, or supporting lateral loads. A design stress of $7 \times 10^8 \frac{N}{m^2}$ (10^5 psi) was used, and buckling design was based on two-thirds of the critical Euler stress. (The Euler stress is the critical stress a beam can support *in compression before* it becomes unstable.) The torsional stresses induced by the curvature of the subassemblies has been ignored. For details of the analysis and design, see Ref. 7-4.

For the hybrid reactor with a maximum magnetic field strength at the conductor of 8.1 T (6.8 T at the mirror), the analysis resulted in a total structural volume of 1.75×10^3 m^3 and a total structural mass of 1.4×10^7 kg.

Some general considerations discussed in Ref. 7-5 suggest that the structural mass could be reduced about 30% or more by inserting structure into part of the space between the large flat faces of the coils.

LIQUID-HELIUM REFRIGERATION SYSTEM

The helium refrigeration system must cool the superconducting magnets and associated retaining structure from room temperature down to the magnet operating

temperature of 4.5 K. After initial cool-down, the refrigerators must remove heat at a sufficient rate to balance the total heat load on the system when the reactor is operational. Some excess in capacity is required to maintain a reserve of liquid helium and also to allow time for maintenance of the refrigeration equipment. Generally, if a system is designed for steady-state operation, the cool-down time will be acceptable.

We did not make a detailed analysis of the heat load on the system because a more complete engineering design is first required. Instead, all heat-load values were scaled from the FERF design study[7-2] with the exception of the neutron heating in the coil structure and superconductor. Table 7-1 contains a breakdown of the heat loads used to size the refrigeration equipment.

Large refrigeration machines operating between room temperature and liquid-helium temperature and utilizing both liquid-nitrogen precooling and expansion engines at several temperature levels generally consume about 500 W per watt of refrigeration at 4.5 K. The calculated input is then 30,160 hp for steady-state operation; however, this would not provide the required redundant capacity. If the compressors were installed in modules of 8000 hp, and if each module operated a separate refrigerator, four refrigerators would be adequate for normal operation. A fifth unit and its compressor module would provide the redundancy for maintenance down-time. Additional refrigeration capacity in the form of liquid-helium storage would serve as a thermal flywheel for the entire system and would also sustain operation for short periods of time if two refrigerators were down.

The helium inventory for the reactor would include both the liquid- and gas-storage volumes, the circulating gas in the refrigeration circuits, and the volume of liquid in the superconducting magnet cases and associated Dewars. An estimate of the total required for continuous operation would be 350,000 ℓ or about 9×10^6 standard ft^3.

Cool-down time from room temperature to 4.5 K for the magnet and cold structure will be approximately 42 days. This

Table 7-1. Mirror hybrid heat loads at 4.5 K.

Heat Source	Heat Load (W)
Neutron heating in coil structure and superconductor	20,000
Conduction to coil and structure	8,400
Radiation to coil and structure	2,250
Superconducting joints	10,000
Current leads	100
Cryopanels	550
Transfer lines	250
Total heat load:	41,550 W[a]

[a]We shall use a design figure of 45 kW to size the refrigeration equipment.

figure is based on a total cold weight of 27,000 tons and all of the 40,000 hp in refrigeration equipment in operation. It also assumes that the low-temperature expanders are turbines and that there is no limitation on liquid-nitrogen consumption. The results of a detailed analysis of the thermal stress problem could substantially increase the cool-down time required.

REFERENCES

7-1. R. W. Moir and C. E. Taylor, Magnets for Open-Ended Fusion Reactors, Lawrence Livermore Laboratory Rept. UCRL-72399 (1970).

7-2. T. H. Batzer, et al., Conceptual Design of a Mirror Reactor for a Fusion Engineering Research Facility (FERF), Lawrence Livermore Laboratory Rept. UCRL-71567 (1974).

7-3. W. A. Perkins and J. C. Brown, J. Appl. Phys. 35, 3337 (1964).

7-4. C. J. Schwer, Lawrence Livermore Laboratory report in progress.

7-5. M. A. Peterson, R. W. Werner, M. A. Hoffman, and G. A. Carlson, A Modularized Mirror Fusion Reactor Concept with Emphasis on Fabricability, Assembly, and Disassembly, Lawrence Livermore Laboratory Rept. UCRL-75236, Rev. 1 (1974).

8. Direct Energy Converter

Most of the trapped, injected neutral beam is scattered into the loss cone (defined by the magnetic field) and lost before it can react. The fraction of the injected current that is consumed in fusion reactions is given by

$$\frac{\Delta I_{in}}{I_{in}} = \frac{2P_F/E_F}{P_{in}/\overline{W}_{in}}$$

$$= 2Q\overline{W}_{in}/E_F = 0.013 \qquad (8\text{-}1)$$

The unburned 98.7% of the current, plus the α-particle current, is scattered into the velocity-space loss cone and escapes through the magnetic mirrors. This loss current must be disposed of, and a direct energy converter offers a practical way to do that besides directly recovering the energy of the escaping particles.

MAGNETIC EXPANDER

The total current into the direct energy converters is I_{DC} = 1900 A (I_{D^+} = 1270 A; I_{T^+} = 630 A) and the total power is P_{DC} = 264 MW, of which 24 A and 40 MW is carried by the α particles. All of P_{DC} is carried by ions which are guided by the magnetic field. The average power per unit area varies inversely with cross-sectional area along a flux tube - just as field strength B does. Therefore, the power per unit area is proportional to B. At the midplane, B = 0.87 T, and the cross-sectional area is $A = \pi r_p^2 = 38.5\ m^2$; therefore, at a mirror where B = 6.8 T, the area is A = 2.5 m^2 (0.1 m thick) at each end. The power flux at each mirror is then $P_{DC}/2A = 5370\ W/cm^2$. To prevent the grid wires from being heated to

temperatures where thermionic emission is important, this average power flux must be reduced to about 50 W/cm^2 before it enters the direct energy converter. A power flux value of 50 W/cm^2 is conservative and allows for some non-uniformity in the flux distribution. Therefore, the field at the direct energy converter is 0.063 T, giving a required area of 270 m^2 for each direct energy converter. Auxiliary superconducting coils outside the main Yin-Yang coils produce the desired field. The field lines guide the escaping plasma out through the rather narrow passage between the structure used to remove the blanket modules (see Fig. 2-6). Because of this restriction, the required area is reached at a distance of 30 m from the center of the reactor.

The reduction in magnetic field from 6.8 T at a mirror to 0.063 T at the direct energy converter also results in a reduction in the perpendicular energy of the escaping ions (and electrons) in the same ratio. Thus, more than 99% of the ion energy will be directed along the field lines and therefore will be available for direct energy conversion.

Note that the present design does not have a neutron trap between the plasma region and the expander of the direct energy converter. Previous designs have included either a 90° bend[8-1] or an S-bend[8-2, 3] for the escaping ions in order to minimize neutron activation of the direct energy converter. The absence of a neutron trap in the hybrid may preclude hands-on maintenance of the components of the direct energy converter. If an activation analysis indicates that this is the case, then a cost-benefit study must be made to determine if the added

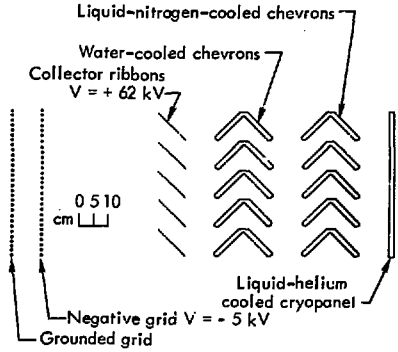

Fig. 8-1. The one-stage direct energy converter and vacuum system for leakage plasma.

structural cost of a neutron trap is justified by the reduced neutron activation in the direct energy converter.

ELECTRODE

We consider a very simple direct energy converter[8-4] consisting of two grids and a single ion collector (see Fig. 8-1). The first grid is held at ground potential and is about 1% opaque to the flow of plasma. The second grid is held negative to repel electrons and to prevent them from reaching the ion collector, which is positive. Electrons reflected by the negative grid pass through the confined plasma (where they may be scattered and heated by the plasma) and out through a mirror to a direct energy converter again. On the average, these electrons will be reflected 50 times by the negative grid before being collected on the grounded grid through which they pass twice for each reflection. The reflecting grid must be held at a high enough negative potential to prevent any appreciable

electron current from reaching the ion collector. A theoretical study using a Fokker-Planck computer code is in progress now to determine the rate of electron heating and hence the voltage to be applied to the negative grid.

For the grid potential to be effective, the spacing between grid wires must be less than a distance of the order of a Debye shielding distance in the plasma near the grid. The shielding distance λ in cm is given by

$$\lambda = 743(T_e/n_e)^{1/2} ,$$

where T_e is the electron temperature in eV and n_e is the electron density in cm^{-3} at the entrance to the direct energy converter. Electron density is equal to ion density, which is about 4×10^6 cm^{-3} here. The electron temperature is more difficult to estimate. In the contained plasma, the Fokker-Planck calculations indicate $T_e = 10$ keV. However, because the ambipolar potential of the plasma is +54 kV* at the center, only those electrons in the tail of the distribution can reach the direct converter, and they will have given up keV. The directed energy of the electrons will be reduced to about 100 eV in the expander in order to match the ion velocity and maintain charge neutrality. Also, the perpendicular energy is converted into directed motion by the magnetic expansion. We assume $T \gtrsim 300$ eV; therefore, $\lambda > 6$ cm, and the grids are made of 0.02-cm-diameter wires with 2-cm spacing between wires. The potential is set at -5 kV to penetrate the plasma and to ensure the reflection of all but the most energetic electrons.

The equilibrium temperature of the tungsten wires will be about 1900 K, resulting in a thermionic emission current of about one electron per ion intercepted. Electrons originating at the grounded grid are repelled by the negative grid and therefore behave similarly to the primary electrons discussed above. About half of the thermionic electrons and most of the secondary electrons originating at the negative grid also behave in the same way. The other half of the thermionic electrons from the negative grid (i.e., about 20 A total for both direct energy converters) come from the side facing the positive electrode and are accelerated into it. This electron current reduces the efficiency of the direct energy converter, although some (35%) of that power is recovered thermally.

After passing through the grids, the ions are collected on an electrode that is held at a positive potential V_{col}. The output from this collector provides a source of positive current at a positive voltage, and so constitutes a source of power. The value of $V_{col} = 62$ kV is chosen to maximize the recovered power.

Optimizing V_{col} depends on the energy distribution of the D^+ and T^+ ions entering the direct energy converter. The energy distribution of these ions is not calculated in the version of the Fokker-Planck code that was used here. However, we know enough about the distribution to set V_{col} and even to make a good approximation to the efficiency of energy recovery.

In steady state, the current I_{loss} of ions escaping from the plasma is just

*When the energy electrons have in the perpendicular direction at the mirrors is taken into account, the ambipolar drop in the expander (~ 10 kV) will add to the 54 kV from the center to the mirror point.

equal to the current I_{in} injected, minus that part ΔI_{in} that is used up in the fusion reactions.

$$I_{loss} = I_{in} - 2P_F/E_F$$

or

$$I_{loss} = I_{in}(1 - 2Q\overline{W}_{in}/E_F) .$$

Here, $\Delta I_{in} = 2P_F/E_F = 24$ A as compared to the total $I_{in} = 1900$ A. The total power leaving the plasma in all forms is

$$P_{out} = P_F + P_{in} .$$

Since the α particles are not adiabatically confined, they escape without sharing their 3.52 MeV per α with the confined D^+ and T^+. Therefore, P_F is carried away entirely by the primary neutrons and α's, so that the power $P_{out}(D, T)$ carried away by the escaping D^+, T^+, and $P_{out}(e)$ carried by the electrons is just equal to that part of the injected power not contributing to P_F. That is:

$$P_{out}(D, T) + P_{out}(e) = P_{in} - \overline{W}_{in}\Delta I_{in}$$

$$= \overline{W}_{in} I_{in}(1 - 2Q\overline{W}_{in}/E_F)$$

$$= \overline{W}_{in} I_{loss};$$

or

$$\overline{W}_{loss}(D, T)\, I_{loss} + \overline{W}_{loss}(e)\, I_{in} = \overline{W}_{in} I_{loss} . \quad (8\text{-}2)$$

Equation (8-2) states a general and useful fact that is true whenever the fusion α particles do not thermalize in the confined plasma. Equation (8-2) becomes even more simple when we require that the electron energy be converted to directed motion by the magnetic expansion and that the directed motion match the mean velocity of the ions to preserve charge neutrality everywhere in the expander. Then $\overline{W}_{loss}(e) \approx 300$ eV and can be neglected in Eq. (8-2); therefore, to a good approximation

$$\overline{W}_{loss}(D, T) = \overline{W}_{in} . \quad (8\text{-}3)$$

Equation (8-3) gives $\overline{W}_{loss} = \overline{W}_{in} = 117$ keV. The distribution function for the loss energy will have a form similar to that calculated for FERF: that distribution decreased almost linearly to zero above a certain minimum energy. The minimum is calculated using the conservation of total energy W:

$$W = W_{\parallel} + W_{\perp} + qV , \quad (8\text{-}4)$$

where $W_{\parallel}$ and $W_{\perp}$ are the energies due to motion parallel to and perpendicular to the magnetic field, and qV is the potential energy of the ion of charge q. The conservation of magnetic moment μ requires that $W_{\perp} = \mu B$, so for those ions that just barely get past the magnetic mirror ($W_{\parallel, m} \approx 0$ there),

$$W = W_{\perp, m} + qV_m ,$$

where subscript m refers to the mirror. Using this to evaluate μ, we can write

$$W_{\perp} = \mu B = W_{\perp, m} B/B_m$$

$$= (W - qV_m) B/B_m .$$

When substituted into Eq. (8-4) and rearranged, this gives

$$W(1 - B/B_m) = W_{\parallel} + qV - qV_m B/B_m .$$

At the center of the plasma, this becomes

$$W(1 - 1/R) = W_{,0} + qV_0 - qV_m/R, \tag{8-5}$$

where subscript 0 refers to the center, and $R = B_m/B_0$. From Eq. (8-5), we see that the minimum energy that an escaping ion can have is when $W_{,0} = 0$. Then

$$W_{min} = \frac{q(RV_0 - V_m)}{R - 1} .$$

The Fokker-Planck calculations yielded $V_0 - V_m = 54$ kV; we have $R = 7.83$. Therefore,

$$W_{min} = qV_m + 62 \text{ keV} .$$

For lack of a better estimate, we assume the plasma potential is zero at the mirror (although, as noted earlier, V_m should be of order kT_e), $V_m = 0$, and set the voltage of the ion collector $V_{col} = 62$ kV. Choosing $V_{col} > W_{min}/q$ would lose more power by reflecting low-energy ions than would be gained by collecting the remaining ions at higher potential. Since V_m is probably a few kV positive, V_{col} could probably be set higher than 62 kV without losing any ions. This would raise the direct energy conversion efficiency.

The ion collector not only must collect the ions at the optimum potential, but also must allow the resulting gas to be removed. For this reason, the collector is constructed of ribbons, each mounted at a 45° angle in venetian-blind fashion (see Fig. 8-1), to present a solid barrier to the directed ions but only slight impedence to the gas. These ribbons will be heated by the excess power from the ions that is not directly converted. Since the mean input power flux is 50 W/cm^2 (about 100 W/cm^2 on central flux lines), and $\eta_{DC} = 50\%$, the mean heat load is 25 W/cm^2. The 45° angle of the ribbons reduces this to 18 W/cm^2 on the faces of the ribbons.

The heat deposited on the ribbon grids is radiatively transferred to high-temperature (≈600°C), water-cooled surfaces behind the ribbon grid and also lining the expander walls. The water-cooled surfaces behind the ribbon grids are arranged in a chevron configuration to permit gas flow to the vacuum system (see Fig. 8-1). The high-temperature water transports the energy to the thermal conversion system.

The spacing between the grounded and the negative grid must be at least a few times larger than the 2-cm spacing between the wires in either grid. It was therefore set at 10 cm. The spacing between the negative grid and the positive collector electrode must be at least a few times larger than the 10-cm spacing between ribbons in the collector in order to produce a uniform electric field to retard the ions without scattering them. However, the spacing must not be greater than the limit set by space charge. The space-charge limit was calculated, assuming an energy distribution given by a Maxwellian distribution that is displaced by an amount equal to the mean energy. This is similar to the distribution at the direct energy converter where the minimum ion energy (62 keV) is roughly half of the mean (117 keV). For our average current density, $J = 3.5$ A/m^2, the maximum spacing is 2.0 m. We chose a 0.40-m spacing to be well within the space-charge limit but sufficiently greater than the 10-cm ribbon spacing.

VACUUM SYSTEM

The gas load resulting from the mirror leakage of energetic D^+ and T^+ ions must be vacuum-pumped, both to limit the back flow of cold gas into the reactor and to limit charge-exchange losses in the expander region. (An energetic ion which charge exchanges in the expander flies to the wall on the tangent of its original helical trajectory. The energy of such an ion is not directly converted.) The ion current escaping from each mirror is approximately 640 A of D^+ and 320 A of T^+. These ions pass through the expander region, are decelerated in the direct energy converter region, and impact the ribbon grid of the collector with some residual energy. The deuterium and tritium refluxes from the collector surfaces as molecular gas. The gas load in each direct energy converter region is 91 Torr·ℓ/s.

The ribbon grid of the collector is opaque to the ion leakage current but presents only a modest impedance to the molecular flow of the refluxed gas. Behind the ribbon grid is a large area of liquid-helium-cooled cryopanel, thermally shielded by an array of liquid-nitrogen-cooled chevrons and an array of high temperature (≈600°C) water-cooled chevrons (see Fig. 8-1).

The available area for cryopanel on the end wall behind the ribbon grid is about 550 m^2. The stacked combination of ribbon grid, water-cooled chevrons, nitrogen-cooled chevrons, and cryopanel was assumed to have 1/11 the pumping speed of a "black hole" of equal area. (A discussion of the factor 1/11 is given in a later paragraph.) The impedance to gas flow from the expander-collector region back into the reactor consists of two slit-like ducts in series, one at the entrance to the expander and one at the mirror region.

A first design utilizing just the cryopanel pumping behind the ribbon grid resulted in a 4.5% loss of ions due to charge exchange and a back flow into the reactor of 4.4% of the refluxed gas. A second design which added 25 m^2 of cryopanel pumping in the volume between the two gas flow impedances reduced the charge-exchange loss to 4.0% and the back flow to 2.9%. The calculated chamber pressures for the second design were 6.1×10^{-6} Torr in the expander and 2.8×10^{-6} Torr in the volume between the two gas flow impedances. Either of these designs is probably adequate. However, verification will require a complete, self-consistent analysis of the gas problem that includes all gas sources and sinks and the dynamics of gas-plasma interaction.

The 1/11 factor used above to relate the pumping speed of the ribbon-grid, water-chevron, nitrogen-chevron, cryopanel combination to a "black hole" was derived by assuming that the four components were separated by volumes containing isotropic distributions of gas in the free molecular flow regime. Then, the pumping speed of the combination (normalized to the "black hole" speed) may be calculated as the reciprocal of the sum of the reciprocals of the normalized speeds of the four components; i.e.,

$$\frac{S}{S_{\text{black hole}}} = \frac{1}{\frac{1}{C_S} + \frac{1}{S_N} + \frac{1}{S_W} + \frac{1}{S_{RG}}} ,$$

where C_S is the sticking coefficient of the cryopanel, S_N is the normalized speed of the nitrogen chevrons, S_W is the normalized speed of the water chevrons, and S_{RG} is the normalized speed of the ribbon grid. For the estimated values $C_S \approx 1$, $S_N = S_W = 0.25$, and $S_{RG} = 0.5$, the result for $S/S_{black\ hole}$ is 1/11. This value is somewhat conservative because for C_S near unity, the gas in the chamber between the chevron and the nitrogen cryopanel is clearly non-isotropic. In the limit where C_S is exactly unity and the final "chamber" is completely lined by cryopanel, every gas molecule which passes through the chevrons is pumped on first impact. Therefore, the normalized speed of the combination becomes

$$1/(4 + 4 + 2) = 1/10.$$

The cryopanels will require periodic "defrosting" so that the condensed gas may be collected through a mechanical pumping system. Two possible designs have been proposed that would allow cryopanel sections to be sequentially isolated and "defrosted" during reactor operation. The first would use a "jalousie" type valve in front of the cryopanel as in the FERF design.[8-5] A disadvantage of this design is the introduction of another impedance to gas flow. The second design[8-6] would use rectangular cryopanel sections of large aspect ratio which would be rotated 180° about their long axes of symmetry to expose the loaded cryosurface to the mechanical pumping system. This design does not introduce another impedance to gas flow and does not appear to involve any more sealing edges than the first design. However, the plumbing for the liquid-helium coolant is more complex than in the first design. Neither design has received more than cursory consideration. It is assumed that each cryopanel will be cycled through its "defrost" condition every hour, or at least every few hours. The total mass of tritium condensed on the cryopanels is 72 g/h.

Modifications to the vacuum system just described will be required in order to handle the helium gas load in each direct energy converter that results from the reflux of the α particles (1.1 Torr·ℓ/s in each direct energy converter). Because the liquid-helium-cooled cryopanels will not pump helium, auxiliary pumps (diffusion type or perhaps cryosorption) will be required to handle the helium. The design speed for the auxiliary pumps will depend on the permissible helium pressure in the direct energy converter. If we assume that hydrogen and helium will compete equally for the auxiliary pumping, but that the cryopanels pump only hydrogen, then

$$\frac{P_{He}}{P_H} = \frac{Q_{He}/S_{aux}}{Q_H/(S_{cryo} + S_{aux})}$$

$$= 0.012 \left(1 + \frac{S_{cryo}}{S_{aux}}\right) .$$

PERFORMANCE

The efficiency of direct energy conversion η_{DC} is just the ratio of the power recovered to the power available for recovery. Since V_{col} is set low enough that all 1900 A of the ion current is collected, the recovered power is 1.90 kA × 62 kV = 118 MW. The available D^+ and T^+

power is 1.90 kA × 117 kV = 222 MW, so that the efficiency is

$$\eta_{DC} = 118/222 = 0.532.$$

This efficiency is reduced by two effects. First, 20 A of thermionic electrons (T_{grid} = 1900 K) flow from the negative grids at -5 kV to the collector at +62 kV, resulting in a power loss of 1.3 MW. To this must be added the loss due to the 1% interception of ions on each grid: 2.2 MW to the grounded grids and 2.3 MW to the negative grids. The combined losses due to grids is 5.86 MW, and this reduces the efficiency to $\eta_{DC} = 0.505$. The second effect is the loss of ion current by charge exchange with background gas. Charge exchange results in the electrical neutralization of an ion, with the result that the ion energy is lost from the direct energy converter, but is still recovered thermally with an efficiency $\eta_{Th2} = 0.35$. With the design gas pressure of 6×10^{-6} Torr in the expander, charge exchange results in a loss of 76 A or 8.5 MW of ions from the direct energy converter. This effect further reduces the efficiency to $\eta_{DC} = 0.467$.

These are the only serious losses to this simple, direct energy converter. Since all magnetic flux lines from the plasma lead to a direct energy converter with no obstructions, there is no interception by support structures or loss due to imperfect coupling to the plasma. There is a slight gain from the α-particle current. The 24 A of α-particles contribute 1.5 MW of electric power at the 62-kV collector. The remaining 40 MW of α-particles is converted to heat and recovered thermally. A larger gain can probably be made by determining more accurately the minimum energy of the ions entering the direct energy converter. Since the plasma potential at the mirror is probably about 10 kV or so positive, the minimum energy and therefore the collector potential will also be greater by the same amount. The efficiency η_{DC} will increase in proportion to the collector potential. We therefore assume that η_{DC} will be greater than the calculated 47%, and for this study we shall assume $\eta_{DC} = 50\%$.

REFERENCES

8-1. R. W. Werner, G. A. Carlson, J. Hovingh, J. D. Lee, and M. A. Peterson, Progress Report #2 on the Design Considerations for a Low Power Experimental Mirror Fusion Reactor, Lawrence Livermore Laboratory Rept. UCRL-74054-2 (1972).

8-2. B. H. Smith, R. J. Burleigh, W. L. Dexter, and L. L. Reginato, An Engineering Study of Electrical Design of a 1000 Megawatt Direct Converter for Mirror Reactors, Lawrence Livermore Laboratory Rept. UCRL-74047 (1972).

8-3. W. L. Barr, R. J. Burleigh, W. L. Dexter, R. W. Moir, and R. R. Smith, IEEE Trans. Plasma Sci. PS-2 71 (1974).

8-4. R. W. Moir and W. L. Barr, Nucl. Fusion 13 (1973).

8-5. T. H. Batzer, et al., Conceptual Design of a Mirror Reactor for a Fusion Engineering Research Facility (FERF), Lawrence Livermore Laboratory Rept. UCRL-51617 (1974).

8-6. L. Pittenger, Lawrence Livermore Laboratory. Private communication.

9. Neutral Beam Injectors

GENERAL DISCUSSION

It is required that 225 MW of neutral beam power be continuously injected and trapped in the plasma. The neutral beam current should be made up of approximately two parts deuterium atoms and one part tritium atoms in order to result in nearly equal densities of trapped D^+ and T^+ ions. Furthermore, to obtain equal penetration depth (and consequently equal densities) of both species, they must be injected with equal velocities and hence unequal energies. The overall system efficiency is found to maximize for a deuterium injection energy of 100 keV with a corresponding tritium energy of 150 keV. This results primarily because the efficiency of neutralizing the beam decreases with an increase in energy in this range while the fractional burnup of the injected beam goes down (see Section 13). Also, the depth of penetration of the beam into the plasma increases with energy, whereby the chosen energy is capable of properly filling the volume.

To allow for a trapping efficiency of 94%, the injector system is designed to produce 1500 A of atomic deuterium at 100 keV and 550 A of atomic tritium at 150 keV. Actually, the preferred ratio of currents required to give equal densities is closer to 2 to 1 rather than the 2.7 to 1 used here.

Although injectors of such magnitudes are beyond the current state of the art, they do not necessarily constitute an unrealistic objective. In the following discussion, we present specific recommendations for design approaches to the more critical problems encountered in any neutral beam system: i.e., provision for a long-lived arc cathode for a reliable grid acceleration system, for the recovery of the unneutralized beam, energy for effective pumping of the vast quantity of gas from the many ion sources, and for adequate shielding to protect the sources from the plasma-confining magnetic fields. These features are applicable to smaller units and to other types of reactors as well.

LAYOUT OF INJECTION SYSTEMS

Figure 2-6, an overall view of the mirror fusion-fission hybrid reactor in vertical cross-section, shows two injector assemblies. Neutral beams will be introduced into the fusion-fission reactor via four separate injectors of two types (see Fig. 2-2). Each injector will consist of 70 ion sources mounted in five rows of 14 units each. The two Type A injectors will have three rows of 100-keV deuterium sources (42 units) along with two rows of 150-keV tritium sources (28 units), while the Type B injectors are composed of two rows of deuterium sources (28 units) and three rows of tritium sources (42 units). In all, there will be 140 ion sources of each type. The desired total of 1500 A of neutral atomic deuterium will require each deuterium source to deliver 10.8 A, while the desired 550 A of tritium will require 3.9 A from each tritium source.

Because the atomic species of ions emitted from each source will be about 75% of the total ion current, and the

neutralizing efficiencies of the deuterium and tritium beams at the respective desired energies will be about 49%, each deuterium source must deliver a total ion current of 29.4 A and each tritium source 10.5 A. Meanwhile, the molecular species D_2^+ and T_2^+ represent about 15% of the beam with currents of 4.4 A and 1.6 A, while the D_3^+ and T_3^+ comprise the remaining 10% at currents of 2.9 A and 1.0 A, respectively. The emitting area (exposed plasma surface) of a Berkeley-type source is about 140 cm^2; hence, the extracted current density of deuterium and tritium ions must be 0.21 A/cm^2 and 0.075 A/cm^2.

The neutral gas efficiency η_s should be at least 30%; and if X^+, X_2^+, and X_3^+ represent the atomic and molecular components of a deuterium or tritium ion beam, Q_{in}, the total gas flow of X_2^0 molecules into each source must be:

$$Q_{in} = (0.19/\eta_s)(1/2X^+ + X_2^+ + 3/2X_3^+) \text{ Torr} \cdot \ell/s \ ,$$

while the low-energy neutral gas flowing out of the source is

$$Q_S = (1 - \eta_s)Q_{in} \text{ Torr} \cdot \ell/s \ .$$

ION SOURCE DESIGN

Arc Cathode

To provide a long-time, continuously operative arc cathode for the ion source, we propose to build a gas tube filament of the "Hull" type.[9-1] This entails three important design features: a large area source operating at a conservative emission current density to assure a potentially long active life; parallel emitting surfaces mounted close to each other so that any active emission material sputtered away from one cathode face will have a high probability of landing on another; and a plasma potential low enough (less than 25 V) to minimize the harmful effects of back ion bombardment.

The first design feature can be achieved with a directly heated ribbon made up of nickel-wire mesh impregnated with a matrix of barium and strontium oxide mixed with a fine, manganese-free, nickel powder. When operated at about 1100 K, such cathodes can easily deliver 0.4 $A \cdot cm^{-2}$ for over 5000 h.[9-2] In addition, they can be opened to air without their emissive properties being destroyed.

The spacing between the parallel emitting surfaces, the second important design feature, must be at least several times larger then the Debye length of the surrounding plasma. Gas tube cathodes have been made of star-shaped structures or by folding an emitting ribbon back and forth, many times.[9-3] However, in the ion source we propose to use six parallel, closely spaced ribbons, mounted along the perimeter of the back side of the ion source. Each adjacent pair of ribbons will be heated by currents flowing in opposite directions from one phase of a three-phase, 400-Hz transformer. The large thermal mass of the emitters will eliminate the need for filamentary rectifiers, while the opposing currents will cancel any undesirable magnetic fields.

The third important design feature, a low plasma potential, is not difficult to achieve, providing the pressure is adequate. However, because the ion source requires an arc voltage of approximately

40 V,[9-4] the plasma in the region of the emitters must be isolated from the arc by a physical restriction that sets up a potential sheath to accelerate the electrons from one region to another. For thermal efficiency, a heat shield can be used for this purpose (see Fig. 9-1).

Typically, for an arc current of 2400 A, 16 strands of 0.16-cm-diam. wire will be required, resulting in a filament width of 3 cm and a current of 400 A at 5.5 V. The ion source filament and arc supplies are shown in Fig. 9-2.

By mounting the rectifiers and transformers directly behind each source, it is possible to control each unit individually at a remote location, via the primary circuit, with a minimum of I^2R power loss. The total filament power is 13.2 kW with an arc power of 0.1 MW.

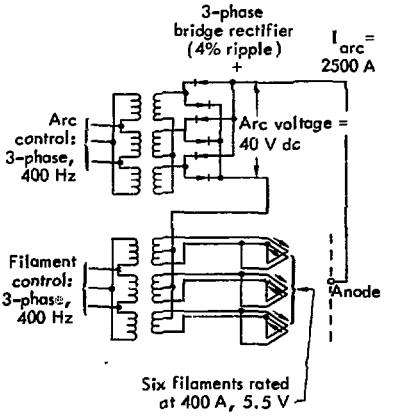

Fig. 9-2. Ion source filament and arc power supplies.

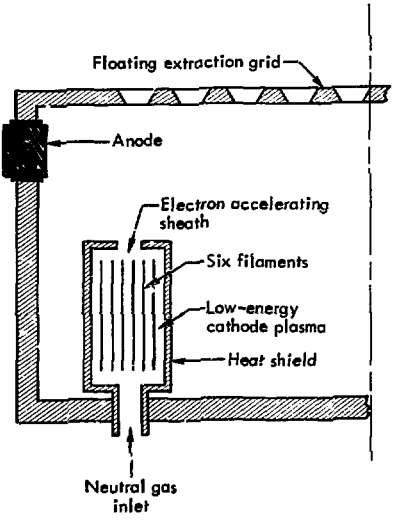

Fig. 9-1. Ion source schematic.

Ion Extraction and Acceleration

General Discussion

The critical features of a high-power, high-current, continuously operating ion extractor are the accelerating grids. Whether they melt in a high-voltage arc, sputter away from ion bombardment, or deform by thermal expansion, their flimsy structure permits damage that can interfere with the operation of the entire source. Therefore, a successful extractor design minimizes the probability of arcing and keeps the grids out of the paths of the charged particles.

To permit high-temperature operation, we consider here only slit grids with laterals transverse to the beam. Such grids are advantageous over those with multiple apertures in that precise alignment from grid to grid is required in only one direction. In this way, allowance for longitudinal expansion of

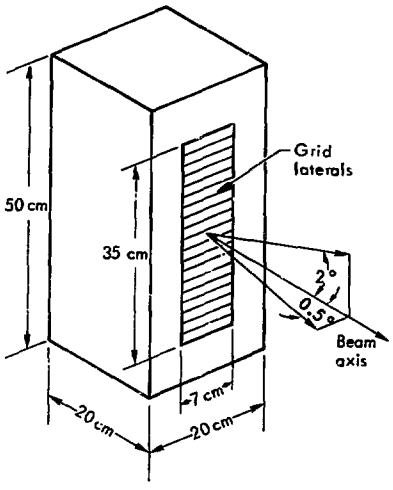

Fig. 9-3. Characteristic dimensions of a Berkeley-type ion source.

the laterals can be made irrespective of the operating temperature. Nevertheless, it is not certain if this configuration permits a greater overall heat dissipation than a multiaperture grid.[9-5]

Beam Contours

Studies of the 15-keV Berkeley source have shown that when slit grids are suitably curved and properly displaced to obtain a reasonable focus, the beam divergence corresponding to 1/e value of current density is approximately 0.5 degrees parallel and 2 degrees perpendicular to the grid laterals.[9-4] Theoretically, because these angles are inversely proportional to the square root of the beam voltage, at 100 keV they should be about 2.5 times smaller. Therefore, a beam spread equal to the original values of 0.5 degrees and 2 degrees, when applied to a 100-kV beam or a 150-kV beam should encompass over 99.8% of the total beam current (see Fig. 9-3). Accordingly, these values have been used in the subsequent calculations.

As shown in Fig. 9-4, the lateral wires of the source grids will be displaced so as to establish a focus, in the plane transverse to the grids, at the blanket wall 700 cm away from the grid face. Meanwhile, no effort will be made to focus the beam in the plane parallel to the laterals. While such a focus could be accomplished by bowing the laterals, in this geometry the consequent reduction in the beam aperture would not warrant the difficulties of fabrication. Particularly

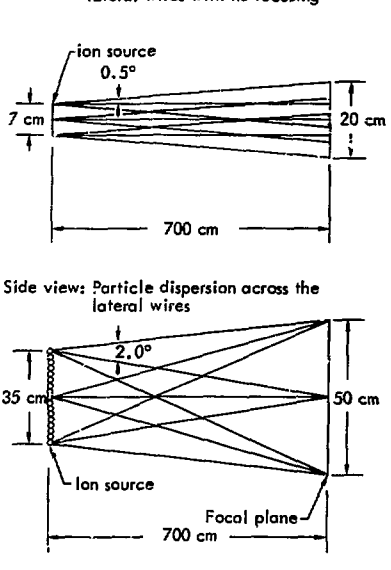

Fig. 9-4. Beam spread diagrams (not to scale).

for a continuously operated beam with grids running hot, the curvature would make precise alignment difficult to maintain. Although the beam is designed to pass through a 20 × 50 cm aperture, some form of skimmer must be included along the injector walls, near the focus, to accommodate the small percentage of the beam that may intercept the reactor wall.

Elementary Extraction

Although all efforts consistent with good high-voltage practice should be made to prevent arcing, it is impossible to obtain a conservative design with a high current density. This has been shown many times to be the consequence of the assumption that the critical voltage, prior to breakdown across a gap, is proportional to the square root of the gap spacing[9-6]; i.e.,

$$V = Cx^{1/2}, \qquad (9\text{-}1)$$

where the proportionality constant C is a function of the electrode material and finish as well as the ambient conditions of temperature, pressure, etc.[9-7]

Introducing this relationship into the Child-Langmuir Equation for beam current density; i.e.,

$$J = q\, V^{3/2}/x^2 \ \mathrm{A/cm^2}, \qquad (9\text{-}2)$$

there results,

$$J = qC^4\, V^{-5/2} \ \mathrm{A/cm^2}, \qquad (9\text{-}3)$$

where for a planar structure,

$$q = (4\epsilon_0/9)(2e/m)^{1/2}. \qquad (9\text{-}3a)$$

Thus, the highest extraction voltage, when applied to a conservative design, will result in the lowest current density. If a Berkeley source delivering 0.5 A/cm^2 at 20 kV is considered typical, the corresponding current density is only 0.01 A/cm^2 at 100 kV if a single accelerator stage is used to extract the beam.

Beam space charge introduces other design restrictions. Whereas an accelerating grid acts as a divergent lens to the individual beamlets passing between the laterals, these beamlets must be initially convergent in order to achieve nearly parallel paths on the far side of the grid.[9-8] To form initial beamlet convergence, the most critical factor is the bevel angle of the laterals constituting the first extracting grid.[9-9] However, this convergence can be seriously impeded by space charge in the beam. Thus, the initial beam current density as well as the slit width between the laterals that control the total charge in the beam can have a marked effect on source performance. These factors, however, are normally resolved by computer studies.[9-10]

To obtain high-energy beams of relatively high current density, it is necessary to introduce post-acceleration stages.[9-8] There are several ways to do this. For convenience, consider the current density to be constant, neglecting the initial convergence previously discussed and noting that the 4/3 power of the spacing varies with the voltage in accordance with Child's Law.

Under these conditions, let V_2, x_2 and V_3, x_3 be the potential and spacing of grids two and three with respect to the first extractor grid at the plasma surface (see Fig. 9-5). Then, for the case where the grids do not disturb the potential distribution along the beam,

$$V_2^{3/2}/x_2^2 = V_3^{3/2}/x_3^2. \qquad (9\text{-}4)$$

If V_{23} and x_{23} represent the voltage and spacing between the second and third grids, then, in accordance with the condition of voltage breakdown,

$$V_2 = C_{12}x_2^{1/2}, \qquad (9\text{-}5)$$

$$V_{23} = C_{23}x_{23}^{1/2}, \qquad (9\text{-}6)$$

where C_{12} is the breakdown proportionality constant between grids one and two, and C_{23} is the corresponding constant between grids two and three. Thus, it is found that:

$$x_{23}/x_2 = \eta^2(C_{12}/C_{23})^2, \qquad (9\text{-}7)$$

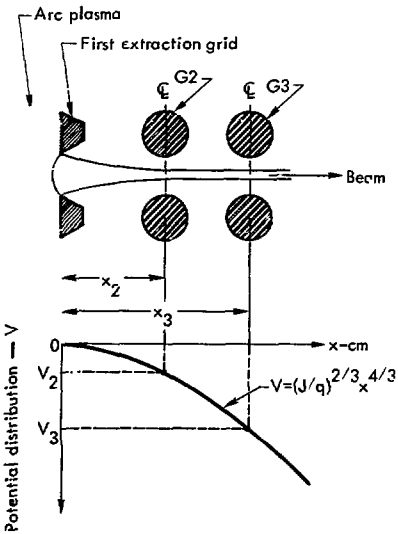

Fig. 9-5. Beam extraction with grids located per Child's Law.

where,

$$\eta = (V_{23}/V_2). \qquad (9\text{-}8)$$

Expanding terms,

$$V_3 = V_2(1 + V_{23}/V_2), \qquad (9\text{-}9)$$

$$x_3 = x_2(1 + x_{23}/x_2), \qquad (9\text{-}10)$$

so that,

$$V_3^{3/2}/x_3^2 = V_2^{3/2}/x_2^2\left[(1+\eta)^{3/4}/(1+\eta^2)(C_{12}/C_{23})^2\right]^2, \qquad (9\text{-}11)$$

whereby,

$$(C_{23}/C_{12}) = \frac{\eta}{[(1+\eta)^{3/4} - 1]^{1/2}}. \qquad (9\text{-}12)$$

For $C_{12} = C_{23}$, $\eta = 0.7$, albeit $V_3 = 1.7\,V_2$. Thus, for a first extractor stage of the Berkeley type, the current density would be 0.5 A/cm^{-2}, with V_2 equal to 20 kV, whereas the corresponding final beam voltage of a single post-acceleration stage would be only 34 kV.

It is possible to add successive stages, requiring five grids to obtain 100 keV. However, we expect that the voltage-holding properties in the post-acceleration gap will be better than those in the initial extraction region. Thus, it is reasonable to allow $C_{23} = 1.5\,C_{12}$, $\eta = 1.5$, and $V_3 = 50$ kV, etc.

Proposed Extraction

An important feature of the following extraction design is the consideration given to the shape of the field lines and to the trajectories of the new-formed,

low-energy ions originating along the primary beam path that may ultimately bombard the grids.

To inhibit the movement of secondary electrons, the ions are first accelerated with an initial set of accel grids and then subjected to a decel grid at a somewhat more positive potential. In this way, secondary electrons emitted from the decel grid can be prevented from being accelerated toward the ion source, although those coming from the accel grid are not suppressed at all. However, it is possible to reduce the ion bombardment of the accel grid and thereby the secondary electron flow, if only by reducing its diameter or by changing the relative potential of the decel grid.

Actually, in the initial extraction gap the decel grid has little affect upon the original ion beam, so that Child's Law applies as before:

$$J = qV_2^{3/2}/x_2^2, \qquad (9\text{-}13)$$

where V_2 and x_2 are the potential and spacing of the first accel grid, G2.

In the post-acceleration region beyond x_3, the potential no longer builds up in accordance with $x^{4/3}$ because of the initial ion velocity. Therefore, a different solution of Poisson's equation is required. Thus, in general,

$$\frac{\partial^2 V}{\partial x^2} = J/\epsilon_0 \left(\frac{m_0}{2e}\right)^{1/2} V^{-1/2}, \qquad (9\text{-}14)$$

which can be rearranged to give,

$$\int_{\left(\frac{\partial V}{\partial x}\right)^2_{x_3}}^{\left(\frac{\partial V}{\partial x}\right)^2_{x}} \frac{\partial}{\partial x}\left(\frac{\partial V}{\partial x}\right)^2 \partial x = \frac{2J}{\epsilon_0}\left(\frac{m_0}{2e}\right)^{1/2} \int_{V_3}^{V} V^{-1/2} \frac{\partial V}{\partial x} dx \qquad (9\text{-}15)$$

The limits of integration are determined by the boundary conditions. Thus, for a simple space charge limited beam as before,

$$\left(\frac{\partial V}{\partial x}\right)_x = \frac{4V}{3x}. \qquad (9\text{-}16)$$

In this case, however, the decel grid reduces the accelerating field in the region of x_2 and x_3 almost to zero, hence:

$$\left(\frac{\partial V}{\partial x}\right)_{x_3} = 0. \qquad (9\text{-}17)$$

Assuming $V_2 \sim V_3$, there results from Eq. (9-15)

$$J = q\left\{\frac{V_4^{3/2} + 3V_3^{1/2}V_4 - 4V_3^{3/2}}{x_{34}}\right\}. \qquad (9\text{-}18)$$

If we allow

$$\xi = (V_3/V_4), \qquad (9\text{-}19)$$

and solve for the value of ξ which results in a maximum J for any given spacing x_{34}, we find at maximum J,

$$\xi = 1/4, \qquad (9\text{-}20)$$

or

$$V_4 = 4V_3. \qquad (9\text{-}21)$$

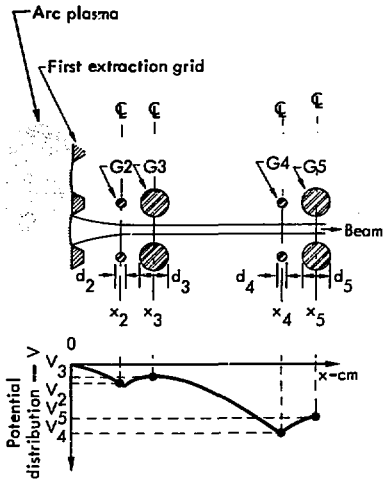

Fig. 9-6. Grid layout and potential profile for a proposed two-stage, five-grid (accel-decel, accel-decel) extractor.

Introducing this into Eq. (9-18),

$$\text{Maximum } J = q\,\frac{16V_3^{3/2}}{(x_{34})^2}\,. \qquad (9\text{-}22)$$

To inhibit breakdown as before, let

$$(V_4 - V_3) = C_{34}x_{34}^{1/2}, \qquad (9\text{-}23)$$

then

$$x_{34} = 9(V_3/C_{34})^2, \qquad (9\text{-}24)$$

and

$$\text{Maximum } J = q\left(\frac{16}{81}\right) C_{34}^4\, V_3^{-5/2}. \qquad (9\text{-}25)$$

But, in the initial extraction gap,

$$J = qC_{12}^4\, V_2^{-5/2}. \qquad (9\text{-}26)$$

Therefore, equating J with the maximum J in the post acceleration gap, and assuming $V_2 \approx V_3$, we find that

$$(C_{34}/C_{12}) = 1.5, \qquad (9\text{-}27)$$

a circumstance that, as noted before, may not be too unfavorable. The potential distribution along the accelerating beam is shown in Fig. 9-6.

Values estimated from these elementary relationships were introduced into the DART computer code[9-11] to calculate the ion beam trajectories. While the results were not perfect, they were close enough to show that satisfactory results could be had with a few more iterations. Typical dimensions are shown in Table 9-1. In this table, the finite thicknesses of electrodes are neglected in the definition of the effective gaps x_{12}, ..., x_{45}.

Gas Flow Through Grids

Neutral gas flowing out of the ion source passes through the various grids, establishing some ambient background density. As a result, some percentage of the accelerating ions suffer charge exchange. While the newly formed neutrals continue with the momentum they had as ions, the new low-energy ions follow field gradients that may be too weak to perturb the original ion beam. Thus, a new ion can be drawn out of the beam to collide with a grid, thereby creating secondary electrons that bombard other more positive grids. Unfortunately, there is always a significant background gas density because most ion sources have inherently poor gas efficiencies. For example, the Berkeley source, with a 50% grid transparency, has a gas efficiency of about 38%.

To minimize grid damage, the background gas density must be reduced. However, the grids act as flow impedances which establish pressure gradients much as a resistor divider string divides the voltage across it. Provided the pressure beyond the grids is low enough, the pressure between them is predominantly a function of the gas flow from the source. Thus, at higher extraction voltages, where grid damage due to ion bombardment is likely to be more severe, the ion beam density must be reduced so that, assuming a constant gas efficiency, the background gas density and the incidence of charge exchange are also reduced.

In these considerations, we have assumed the pressure beyond the grids to be 2×10^{-3} Torr. Whereas the Berkeley source delivers 0.5 A/cm^2 at 20 kV with a gas flow of 21 Torr·ℓ/s, operating at about 2×10^{-2} Torr, the 100-kV deuterium source is presumed to deliver 0.2 A/cm^2 with a gas flow of 12.6 Torr·ℓ/s, operating at a pressure of 10^{-2} Torr. The 150-keV tritium source meanwhile

Table 9-1. Various extractor designs.

	Berkeley Source	LLL Design	
Ions	D^+	D^+	T^+
First accel stage:			
V_1 (kV)	20	100	150
V_2 (kV)	-1	75	112.5
J (A/cm^2)	0.50	0.20	0.075
x_{12} (cm)	0.39	0.60	1.2
$q_{12} = jx_{12}^2 V_2^{-3/2}$ (A·V$^{-3/2}$)	2.7×10^{-8}	1.8×10^{-8}	1.5×10^{-8}
$C_{12} = V_2 x_{12}^{-1/2}$ (V·cm$^{-1/2}$)	3.2×10^4	3.2×10^4	3.4×10^4
First decel stage:			
G2 diam., d_2 (cm)	0.20	0.05	0.05
G3 diam., d_3 (cm)	0.20	0.20	0.20
x_{23} (cm)		0.20	0.20
V_3 (kV)	0	83.0	120.5
Second accel stage:			
V_4 (kV)		-8	-8
V_{34} (kV)		75	112.5
x_{34} (cm)		2.3	4.6
$C_{34} = V_{34} x_{34}^{-1/2}$ (V·cm$^{-1/2}$)		4.9×10^4	5.2×10^4
Second decel stage:			
G4 diam., d_4 (cm)		0.05	0.05
G5 diam., d_5 (cm)		0.20	0.20
x_{45} (cm)		0.20	0.20
V_5 (kV)		0	0

operates at 0.075 A/cm^2 with 4.5 Torr·ℓ/s flow of gas, operating at 5×10^{-3} Torr. Various pressures as calculated for the regions between the grids are shown in Fig. 9-7.

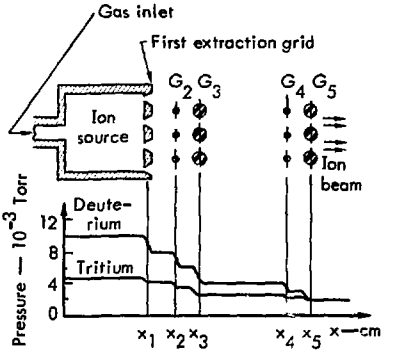

Fig. 9-7. Pressure profile in the proposed extractor.

Charge Exchange and Ionization in the Extractor

The important advantage of the design of the proposed extractor is the prospect of controlling the trajectories of the newly formed ions and secondary electrons. Assuming a neutral gas temperature of 1000 K, the fraction of an ion beam that charge-exchanges or ionizes the background gas over a short path length Δx can be approximated by

$$F_0 = 10^{16} P_x \sigma_i \Delta x, \qquad (9\text{-}28)$$

where P_x is the neutral gas pressure in Torr, and σ_i is the cross section for production of ions by charge exchange and ionization. Because σ_i is a function of the ion velocity, and because the potential distribution from which the ion velocity can be evaluated is known along the acceleration gap length, it is possible to determine the cross section as a function of the ion path. Such values are shown in Fig. 9-8 for the Berkeley source as well as for the 100-kV deuterium and 150-kV tritium sources described here.

Using the potential distribution in the acceleration gaps as calculated by the DART code when determining the primary ion beam contours, it was possible to establish the path of any ion starting out with zero energy anywhere along the beam, and to learn which grid, if any, it would strike and with what energy. Furthermore, from a knowledge of the region where this ion originated, i.e., some Δx of the beam length, using the previously calculated cross-section curves, it is possible to estimate the bombarding ion current, as it is equal to the fraction of the original ion beam neutralized along Δx. The percent of the beam which was neutralized is equal to the area subtended by the appropriate curve in Fig. 9-8, over the length Δx (in units of cm) multiplied by the background gas density ($10^{16} P_x \text{cm}^{-3}$). The pressures in the various gaps, as previously discussed, are shown in Fig. 9-7.

A rough evaluation of the 100-kV deuterium source was made this way, using 60 low-energy ions starting, slightly off axis, at uniform intervals along the beam path. Again with the aid of the DART code, the trajectories of secondary electrons were evaluated. These electrons originated on the surface of the grids at the site of an impact of a bombarding ion. It was assumed that two electrons were emitted for every incident ion.

Preliminary results of these calculations are shown in Table 9-2. Sputtering will be a serious problem. As originally designed, ion bombardment of G5 is excessive. However, by reducing the diameter of the grid from 0.2 to 0.08 cm, most of the ions can be induced to miss it, and the grid dissipation can be markedly reduced as indicated in the table by G5a.

Because of the high bias between G2 and G3, as well as between G4 and G5, almost no electrons emitted from G3 and G5 can escape. In fact, electrons emitted from G1 can only go into the plasma because of the negative field in front of

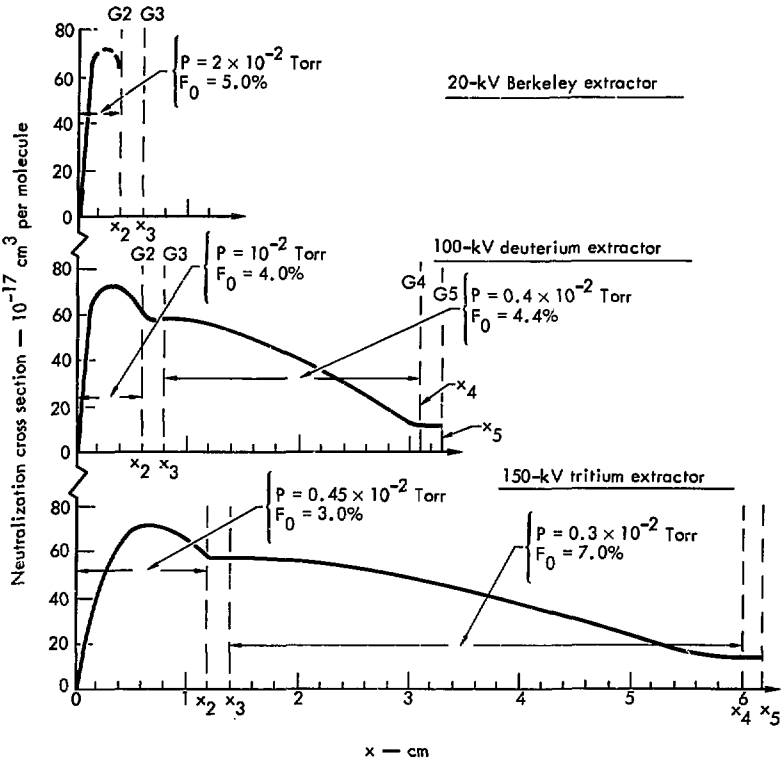

Fig. 9-8. Neutralizing cross sections in various extractors. If the background gas temperature is 1000 K, the fraction of charge-exchange events occurring over a beam length x becomes

$$F_0 = 10^{16} \int_0^x P_{Torr}\, \sigma_{10}\, dx.$$

Table 9-2. Grid bombardment by ions produced by charge exchange and by the secondary electrons produced on the grid surfaces.

Test grid	Design feature: No. of laterals[a]	Design feature: Lateral circumference (cm)	Ion bombardment: Current (A)	Ion bombardment: Energy (keV)	Ion bombardment: Power (kW)	Electron bombardment: Source of secondary electrons	Electron bombardment: Current (A)	Electron bombardment: Energy (keV)	Electron bombardment: Power (kW)	Total power (kW)	Total power density
G5	105	0.20-	0.33	93	30.7	G4	0.04	8	0.3		
			0.13	81	10.5						
			0.07	65	4.6						
			0.07	5	0.4					46.5	100.7
G5a	105	0.08-	0.04	81	3.2	G4	0.04	8	0.3		
			0.04	3	0.1					3.6	19.5
G4	105	0.05-	0.04	8	0.3					0.3	2.6
G3	105	0.20-	0.33	4	1.3	G2	0.12	8	1.0		
						G4	0.02	90	1.8	4.1	8.9
G2	105	0.05-	0.19	8	1.5					1.5	13.0
G1	105	0.5				G2	0.16	26	4.2		
						G4	0.02	108	2.2	6.4	17.4

[a]All grid laterals are 7 cm long.

that grid. Only G2 and G4 then act as sources of electrons which might do damage to other grids. As a result, all grids but G2 and G4 can be operated at temperatures high enough to support electron emission. However, allowance must be made for thermal expansion of the laterals without disturbing the grid alignment.

Obviously, there are many design options available, such as the lateral wire diameter, grid location and potential, to establish secondary fields which will guide newly-formed ions into regions where they do the least damage. Only the most cursory attempt to optimize these designs has been made to date, and much work is yet to be done to analyze the power flow.

EJECTOR PUMPS

Each ion source operates at a high positive potential relative to ground, and it is packaged, with its own filament and arc supply, inside a grounded electrostatic shield of which the final decel grid forms a part. Through this grid, the high energy ions travel toward the neutralization cell along with the low-energy neutral gas Q_S which flows from the ion source. Actually, only a limited quantity of low-energy gas Q_N will proceed into the neutralizer. The remainder $(Q_S - Q_N)$ flows back between the shielded ion sources and into a large pumping chamber that is roughly 2 × 4 m in cross section and possibly 5 m deep (see Fig. 9-9).

The gas flow through the neutralizer Q_N can be evaluated by assuming that the pressure P_0 between the ion source and the neutralizer cell is maintained by the pumps at 2×10^{-3} Torr. The neutralizer, 1 m long, has two liquid-nitrogen-cooled walls. The 10-cm separation between these walls is just enough to clear the beam. At the neutralizer output, the ambient pressure P_R is kept at less than 2×10^{-4} Torr by cryopanels mounted on each side of the beam.

From a calculation of the conductance of the neutralizer cell, the flow of gas

Q_N is determined to be 3.0 and 2.4 Torr·ℓ/s for deuterium and tritium. These data are arranged in Table 9-3 to allow evaluation of the total gas flow in both the Type A and Type B injectors.

Because a 120-cm mercury ejector pump is capable of pumping 5×10^4 ℓ/s of hydrogen, four fully baffled pumps should be more than capable of handling the 1.33×10^5 ℓ/s required for a Type A injector and the 0.98×10^5 ℓ/s required for a Type B injector.

NEUTRALIZER CELL

The neutralizer thickness π is defined as:

$$\pi = \int n dx \ cm^{-2}, \qquad (9\text{-}29)$$

where x is the neutralizer length, and n, the background gas density, can be expressed by

$$n = P_x/\underline{k}T \ cm^{-3}. \qquad (9\text{-}30)$$

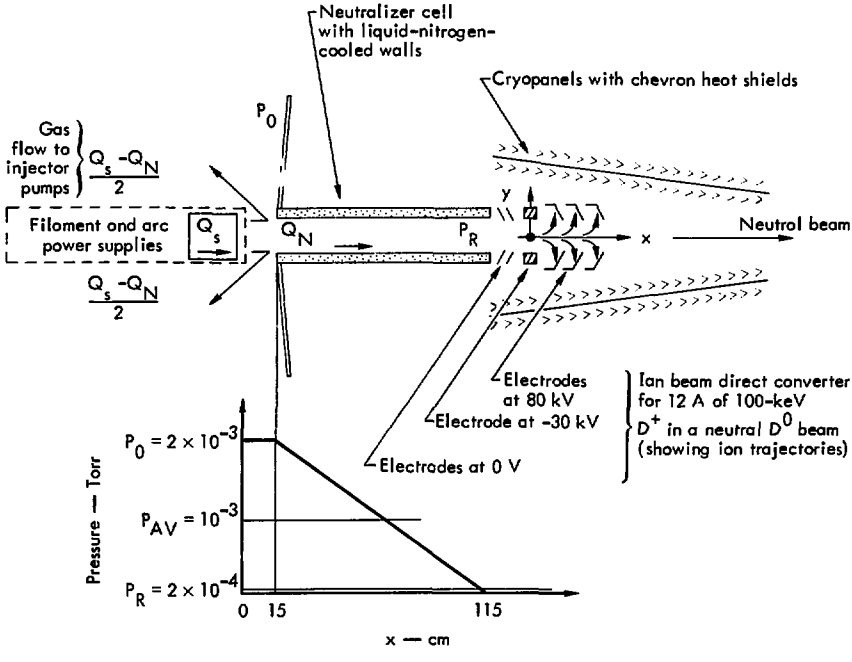

Fig. 9-9. Beam line schematic and pressure profile through the neutralizer cell, including the beam direct-energy recovery system.

Table 9-3. Gas pumping requirements.

	Type A injector		Type B injector	
	Deuterium	Tritium	Deuterium	Tritium
No. of sources, N	42	28	28	42
Gas efficiency, η_s	0.3	0.3	0.3	0.3
Gas flow per source (Torr·ℓ/s)				
Q_{in}	12.6	4.5	12.6	4.5
$Q_s = (1 - \eta_s)Q_{in}$	8.8	3.2	8.8	3.2
Q_N	3.0	2.4	3.0	2.4
$(Q_s - Q_N)$	5.8	0.8	5.8	0.8
Total flow, (Torr·ℓ/s)				
$N(Q_s - Q_N)$	244	22	162	34
Total ΣQ	266		196	
Pump pressure, P_0 (Torr)	2×10^{-3}		2×10^{-3}	
Pumping speed, $S = \frac{\Sigma Q}{P_0}$ (ℓ/s)	$1.33 \times 10^{+5}$		$0.98 \times 10^{+5}$	

In Eq. (9-30), P is the background pressure in Torr, T the gas temperature in K, and $\underline{k}$ the Boltzman constant in these units, i.e., 1.04×10^{-19} Torr·cm^3/K.

Per Fig. 9-9, the neutralizer thickness can be calculated from:

$$\pi = (P_0/\underline{k}T)x_1 + (1/2P_0/\underline{k}T)x_2 \text{ cm}^2. \quad (9\text{-}31)$$

In Eq. (9-31), it is assumed that the neutralizer walls are liquid-nitrogen cooled, thus the gas temperature T is about 77 K. Allowing for the space between the ion source and the neutralizer, x_1 is 15 cm and P_0 is 2×10^{-3} Torr. Meanwhile, the average pressure in the neutralizer cell is about 1/2 P_0 and its length x_2 is 100 cm. Thus, π equals 1.5×10^{16} cm^2.

The neutralizer efficiency is

$$F = F_{0\infty}\left[1 - \exp\left\{-\pi(\sigma_{10} + \sigma_{01})\right\}\right], \quad (9\text{-}32)$$

where $F_{0\infty}$ is the efficiency of an ideal neutralizer of infinite length, and σ_{10} and σ_{01} are the ion-neutralization and the neutral-ionization cross sections at the beam energy under consideration.

Both the 100-keV deuterium and the 150-keV tritium beams travel at the same speed; therefore, their neutralization efficiencies and cross sections are equal, albeit

$$F_{0\infty} = 0.53, \quad (9\text{-}33)$$

and

$$(\sigma_{10} + \sigma_{01}) = 1.68 \times 10^{-16} \text{ cm}^2 \quad (9\text{-}34)$$

for the neutralizer cell described here.

Then,

$$\pi(\sigma_{10} + \sigma_{01}) = 2.5, \qquad (9\text{-}35)$$

and

$$F \approx 49\%. \qquad (9\text{-}36)$$

Similarly, for D_2^+ and T_2^+, F is 72%; and for D_3^+ and T_3^+, F is 78%.

ION ENERGY RECOVERY

Exiting from the neutralizer cell is a flow of low-energy neutral gas (Q_N per source), a beam of high-energy neutrals with components of either 100-, 50-, and 33-keV D^0 or 150-, 75-, and 50-keV T^0, and the remainder of the high-energy ion beam which did not become neutralized. This mixture enters the ion energy recovery system where negatively biased electrodes, located on both sides of the beam, hold back any electrons which would otherwise be extracted from the neutralizer by the positive potential of the ion-collector electrodes. Figure 9-10 shows the electrode configuration in the direct converter for a deuterium source.

This electrode configuration was developed using the DART code. However, the space-charge blowup of the beam beyond the negative stage (where the neutralizing electrons are stopped) can be approximated by making a few simplifying assumptions. The analytic solution gives the dependence on the various parameters, and in particular, shows how to adapt the deuterium energy converter design to tritium beams.

Consider a sheet beam of ions of thickness h flowing in the x direction (see Fig. 9-10). The ion charge density ρ is approximately uniform across the beam and is proportional to the current density j divided by the directed ion velocity v_x. The velocity v_x depends on initial energy W_0 and on the potential ϕ, which is assumed to increase linearly with x. That is, for motion in the x-direction we ignore space charge and assume a uniform applied field E_x in the negative x direction. We define distance L by setting $E_x = -W_0/eL$, where e is the charge on the ion. Electrons are stopped at x = 0 with the result that the space charge of the ions will cause the beam to expand beyond this point. By Gauss' Law, the space-charge field outside the beam is given by (neglecting the x-component of space-charge field)

$$E_y = \rho h/2\epsilon_0,$$

where $\epsilon_0 = 8.85 \times 10^{-12}$ f/m. We express ρ in terms of the total ion current I which is assumed to be constant.

$$\rho = I/\ell h v_x,$$

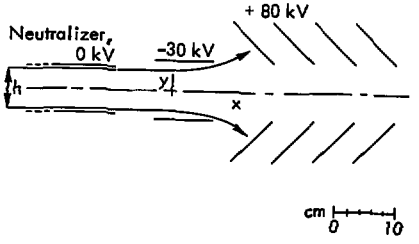

Fig. 9-10. Beam direct converter for 12 A of 100-keV D^+ in the presence of a neutral D^0 beam.

where ℓ is the width of the beam (measured into the paper in Fig. 9-10). Then, the outward acceleration of the ions at the edge of the beam is

$$\frac{dv_y}{dt} = eE_y/M = eI/2\epsilon_0 M\ell v_x .$$

Divide this by the longitudinal acceleration,

$$\frac{dv_x}{dt} = eE_x/M = -W_0/ML,$$

to obtain

$$\frac{dv_y}{dv_x} = -eIL/2\epsilon_0 W_0 \ell v_x .$$

This can be integrated to give

$$v_y = (eIL/2\epsilon_0 W_0)\ln(v_0/v_x), \qquad (9\text{-}37)$$

where $v_0 = (2W_0/M)^{1/2}$ is the initial value of v_x. The conservation of energy requires that

$$\frac{1}{2}M\left(v_x^2 + v_y^2\right) + e\phi = W_0,$$

We assume $v_y^2 \approx v_x^2$ when the ions contact the walls, so that

$$v_y^2 \approx v_x^2 \approx (W_0/M)(1 - e\phi/W_0).$$

Finally, we can solve Eq. (9-37) for I/ℓ and substitute in for v_x and v_y to get

$$\frac{I}{\ell} \approx \frac{2\epsilon_0}{eL}\sqrt{\frac{2}{M}}\, W_0^{3/2}\left(\frac{v_x/v_0}{\ell n\, v_0/v_x}\right), \qquad (9\text{-}38)$$

where $v_x/v_0 = \left[\frac{1}{2}(1 - e\phi/W_0)\right]^{1/2}$.

Eq. (9-38) is not exact, but it does give the functional dependence of the space-charge limited current I on ionic charge e, ionic mass M, initial ion energy W_0, scale-length L, and on the approximate efficiency of energy recovery

$$\eta_{BDC} \approx e\phi/W_0 .$$

For example, Eq. (9-38) indicates that to collect 100-keV D^+ at 80 kV, (if all of the ion current were collected, this operation would be ideally 80% efficient) $v_x/v_0 \approx 0.32$, and (with ℓ = 35 cm, L = 10 cm) I = 5.3 A. With the recovery electrode at 70 kV, I = 7.8 A. These currents are low by a factor more than two from the more accurate values obtained numerically from the computer code. Thus, Eq. (9-38) is useful to show the functional dependence of current on the other parameters.

Detailed numerical calculations were done with the DART code and the geometry shown in Fig. 9-10. The results were that 6.7 A of a 7.0-A beam of 100-keV D^+ is collected on the 90-kV electrodes. The central 0.3 A of the beam is either reflected back into the neutralizer or passes on through the direct converter toward confined plasma. Whether the central part is reflected or transmitted, and just what fraction of the beam does one or the other, depends critically on the current I. Equation (9-38) shows that if the collector voltage is decreased from 90 to 83 kV, the current can be increased to 12 A with an efficiency of 78% for collection of the full energy D^+.

However, the 10.8 A of 100-keV D^0 are accompanied by not only 12.0 A of

100-keV D^+, but also by 6.4 A of 50-keV and 7.1 A of 33-keV D^0, 2.3 A of 50-keV and 1.4 A of 33-keV D^+, plus insignificant currents of D_2^0, D_2^+, and D_3^+. The power carried by the fractional energy ions is only 12% of the total unneutralized beam power. The simple direct converter considered here is not capable of recovering power from fractional energy ions. Simply inserting a low-voltage electrode, to intercept low-energy ions as they leave the beam, does not work if it requires an increase in the length. It may be possible to insert scraper electrodes along some existing equipotential surface to recover some low-energy power without sacrificing many of the full-energy ions as indicated in Ref. 9-12. For the present, we assume that the fractional-energy ions are recovered at zero net efficiency. This assumption requires a balance between those that strike the negative electrode releasing secondary electrons and those caught on a scraper electrode. That leaves only the 88% of the beam power that is carried by full-energy ions, and they are collected with 78% efficiency. The net efficiency of the beam direct converter is then $\eta_{BDC} = 69\%$.

The other 31% of the unneutralized beam power will appear as heat and will require cooling. This heat could be converted to electricity in a thermal bottoming cycle to the direct converter. For example, if the thermal efficiency is limited to 35% (because of the different high voltages), the net direct converter efficiency would be $\eta_{BDC} = 0.80$. A more satisfactory solution would be to avoid the molecular ions and prevent the fractional energy ions and neutrals from being produced. In fact, the fractional energy neutrals may present an even more serious problem than the fractional-energy ions do, because the low-energy neutrals do not penetrate deeply into the plasma, and may even produce a net power loss from the plasma by charge exchange with trapped full-energy ions.

So far, the direct converter discussion has focused on the deuterium injectors. For tritium, the efficiency is higher because the lower current and higher energy (4.3 A of 150-keV T^+ instead of 12 A of 100-keV D^+) more than offsets the effect of the increased mass of the ions. We again use Eq. (38) to scale the computer results and find that the collector voltage should be set at 143 kV to collect 95% of the full-energy tritons at 95% of full voltage. This would give $\eta_{BDC} = 0.91$ if no fractional-energy T^+ were present. Including them reduces the efficiency to $\eta_{BDC} = 0.81$, with the same assumptions as for deuterium.

The collected ions become a gas load in the direct converter, and result (see below) in a gas pressure of 2×10^{-4} Torr. To hold the voltages at this pressure, the Paschen curve for hydrogen shows that the interelectrode spacing must be less than about 0.5 m. Since the overall length of the direct converter is 0.5 m, the condition is satisfied.

The collected ions constitute a gas load (Q_B per source) that must be pumped away along with the gas Q_N that flows out of the neutralizer. The gas flow Q_B can be calculated as

$$Q_B = (0.19)(1/2X^+ + X_2^+ + 3/2X_3^+) \text{ Torr} \cdot \ell/s \quad . \quad (9\text{-}39)$$

where X_1^+, X_2^+, X_3^+ represent the atomic and molecular ion components of the beam.

Thus, it is determined that Q_B is 1.5 Torr·ℓ/s and 0.5 Torr·ℓ/s for the deuterium and tritium beams, whereas the sum $(Q_B + Q_N)$ is 4.5 and 2.9 Torr·ℓ/s, respectively. To maintain a pressure P_R of 2×10^{-4} Torr in this region, the pumping speed S_p must be such that

$$S_p = \frac{Q_B + Q_N}{P_R} \text{ ℓ/s}, \qquad (9\text{-}40)$$

from which it is determined to be 2.3×10^4 ℓ/s for a deuterium beam and 1.5×10^4 ℓ/s for tritium.

Because a baffled cryopanel can cope with 7 ℓ/s per cm^2, approximately 3300 cm^2 and 2100 cm^2 of cryopanel surface are needed in the ion energy recovery system region to maintain the desired pressure.

It has been assumed, however, that the ion energy recovery system will require about 50 cm of beam line with an average height of 60 cm reserved for the output of each ion source. Thus, allowing for two cryopanel surfaces, one on each side of the beam, there will be approximately 6000 cm^2 of cryopanel surface available.

PRE-INJECTION PUMPING

Beyond the energy recovery unit, another 100 cm length of cryopanel is planned. This far down along the beam, these panels must be separated by about 27 cm to minimize beam interception, and the average ratio of panel length to half width of separation becomes 7.4.

According to Smith and Lewin's study,[9-13] a corresponding ratio of length to radius of a cylindrical pumping system results in a pressure drop to about one two-hundreth of the original value. If this value is applied to this planar parallel case, the pressure at the blanket window should be of the order of 4×10^{-6} Torr.

MAGNETIC SHIELDING

The injectors, neutralizing cells, and beam energy recovery systems must be shielded from the fringing portion of the reactor magnetic field. The volume to be shielded, indicated by Fig. 9-11 is a truncated pyramid for each injector assembly, with a base of dimensions 7×3.5 m and with an altitude of 3 m. In principle, it is possible either to shield the entire assembly or to shield each individual module.

The fringing magnetic field is two dimensional on its plane of symmetry, which includes the centerline of each injector assembly. The fringing field is roughly parallel to the reactor containment field within the magnetic coils, and is anti-parallel to the containment field outside the coils in the flux-return region. A region of minimum field intensity exists where the field reverses its direction. Fortunately, the injector assemblies are located in this region of minimum flux intensity, where the magnetic shielding requirements are least severe.

Figure 9-11 shows the magnetic field intensities along the beam line axis, where $B_\parallel$ and $B_\perp$ are the field components parallel to and perpendicular to the beam-line axis. The portion of the injector

assemblies requiring magnetic shielding extends for about 3 m. Note that this region includes the points of field reversal and the minima of $B_{\parallel}$ and $B_{\perp}$.

The maximum fringing fields to be excluded are $B_{\parallel\,max}$ = 2.3 kG and $B_{\perp max}$ = 4.2 kG. Magnetic shields for such

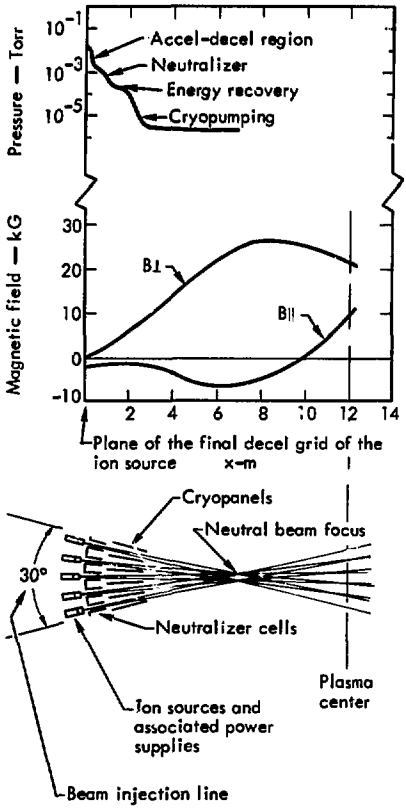

Fig. 9-11. Beam convergence and profiles of pressure and fringing magnetic fields, where $B_{\perp}$ and $B_{\parallel}$ are the components of the field perpendicular and parallel to the beam axis.

field intensities are feasible but are not trivial for large volumes. In this design, we shall take advantage of experience and computations arising from design and operation of the injection systems for Baseball and for 2XII.[9-14]

Experience is available on operation of a superconducting magnetic field which successfully excluded a kilogauss magnetic field from a volume comparable to the size of one injector module. An iron shield was also required to reduce the field below 10 G because of openings in the superconductor. It can be stated with a high level of assurance that similar techniques will fulfill the shielding requirements of the fusion-fission reactor. Engineering development is required to determine the best design for the purpose, but is not required to demonstrate feasibility. A superconducting shield for each module can be installed in thermal contact with the cryogenic gas-pumping surfaces required for each module.

INJECTOR EFFICIENCY

The overall efficiency of the injector system is important in any application. On mirror-type fusion reactors, the injector efficiency must be high because of the large recirculated power. Typically, only a few percent of the injected current (1.3% in the present hybrid design) results in fusion reactions, and the remainder must be recovered and reinjected with good efficiency. This is why direct conversion of both the unused beam and the escaping plasma is so important.

We evaluate the overall injector efficiency by analyzing each process separately. Various injector performance

Table 9-4. Injector performance.

	Berkeley design	LLL Fusion-fission design	
Gas	Deuterium	Deuterium	Tritium
Beam energy (keV)	20	100	150
Operation	Pulsed	Continuous	Continuous
Filament power/source (kW)	34	13.2	13.2
Arc power source (MW)	0.20	0.10	0.10
Extractor power/source (MW)	1.4	2.94	1.6
Source pressure (Torr)	2×10^{-2}	1×10^{-2}	0.5×10^{-2}
Gas efficiency (η)[a]	33	30	30
Total gas flow source (Torr·ℓ/s)	21.0	12.6	4.5
Emission current density (A·cm^2)	0.50	0.21	0.075
Total ion current source (A)	70.0	29.4	10.5
Beam components (A)[b]			
X^+ (75%)	52.5	22.1	7.9
X_2^+ (15%)	10.5	4.4	1.6
X_3^+ (10%)	7.0	2.9	1.0
Neutral beam output source (A)[c]			
X^0 (E = 49%)		10.8	3.9
X_2^0 (E = 72%)		3.2	1.2
X_3^0 (E = 78%)		2.3	0.8
Unneutralized out source (A)[c]			
X^+		11.3	4.0
X_2^+		1.2	0.4
X_3^+		0.6	0.2
Equivalent gas flow of unneutralized output source (Torr·ℓ/s)[d]		1.5	0.5
Total number of sources		140	140
Total x^0 (A)		1500	550
Injected neutral beam power (MW)			
At full energy		150	82.5
At half energy		44.4	25.4
At third energy		31.9	16.9

[a]Gas efficiency = equivalent gas flow/total gas flow.

[b]X^+, X_2^+, X_3^+ represent the atomic and molecular flow in amperes.

[c]Molecular ions X_2^+ and X_3^+ will be dissociated by collisions in the neutralizer, but in this table they are computed as if they were not dissociated.

[d]Equivalent gas flow = $0.19\ (1/2X^+ + X_2^+ + 3/2X_3)$ Torr·ℓ/s .

parameters are summarized in Table 9-4. In the diagram (Fig. 4-2) of the flow of power through the injector system, η_{ac} is the efficiency of producing and accelerating the ions. Earlier in this section, we determined that 13.2 kW are used by the filaments and 100 kW by the arc in one 29.4-A deuterium source

(see Table 9-4). This amounts to 3.8 keV per deuteron and a 3.6% loss of energy for 100-keV ions. Less arc power is required in a 10.5-A tritium source, but will probably amount to slightly more than 3.8 keV per triton. We assume a 3.8% loss for 150-keV tritons, the same as for the 100-keV deuterons.

Losses during acceleration result from secondary ions which result from charge exchange and ionization of background gas. These ions are accelerated in the electric field and may strike a grid, giving up energy and releasing secondary electrons. These processes are discussed on p. 93, and the results are tabulated in Table 9-2. The total loss due to grid bombardment is 16 kW for the case with reduced size for G5. Secondary ions which escape without striking a grid probably account for another 16-kW loss, making a total loss of about 30 kW in accelerating 29.4 A of ions. This amounts to a 1% loss for a deuterium source, and we assume the same for tritium. When combined with the 3.6% loss in creating the ions, the total loss is about 4.6%. Therefore, η_{ac} = 95% for both deuterium and tritium.

The neutralizer efficiency F was shown above to be F = 0.49 for D^+ and T^+, F = 0.72 for D_2^+ and T_2^+, and F = 0.78 for D_3^+ and T_3^+. For the entire beam (which was measured in a Berkeley source to consist of 75% D^+, 15% D_2^+, and 10% D_3^+), the net efficiency of the neutralizer is F = 0.55 for both deuterium and tritium.

The net efficiency of the direct converter for recovering power from the unneutralized ions was shown to be η_{BDC} = 0.69 for deuterium and η_{BDC} = 0.81 for tritium, assuming the fractional-energy ions are caught at zero efficiency. A thermal bottoming cycle could increase this to 0.80 and 0.88, respectively. If the fractional-energy ions are eliminated, the direct converter efficiencies without a thermal cycle increase to 0.78 for the 12 A of 100-keV D^+ and 0.91 for the 4.3 A of 150-keV T^+.

Overall injector efficiency is defined here as the ratio of the neutral beam power that is injected and trapped (P_{in} = 225 MW) to the total power consumed by the injector system. Figure 4-2 shows the power flow through the injector system for the case where fractional-energy ions are present and taking η_{BDC} = 0.69 and F = 0.55. No thermal cycle is assumed for the injector, but that part of the neutral beam power that is not trapped in the plasma is assumed to be recovered in a thermal cycle with efficiency η_{Thl} = 0.38. The calculations of the beam penetration were described in Section 5. It appears that 94 to 96% of the beam power is trapped. We assume here that f_T = 0.94. The result is (see Fig. 4-1) that the injector system consumes 318 MW in injecting 225 MW, giving for the injector efficiency η_i = 0.71.

REFERENCES

9-1. A. W. Hull, Trans. AIEE 47, 753 (1928).

9-2. M. Von Ardenne, VEB Deutscher Verlag der Wissenschaften, Band I, 84 (Berlin, 1962).

9-3. E. F. Lowry, Electronics 6, 280 (1933).

9-4. K. H. Berkner, W. R. Baker, W. S. Cooper, K. W. Ehlers, W. B. Kunkel, R. V. Pyle, and

J. W. Stearns, in Proc. Second Symp. Ion Sources and Formation of Ion Beams, 1974 (Berkeley, CA, 1974), paper VI-12.

9-5. H. C. Cole, D. P. Hammond, E. M. Jones, A. C. Riviere, and J. Sheffield, in Proc. Second International Ion Source Conference, 1972 (Vienna, 1972), paper d-4, p. 271.

9-6. D. R. Sweetman, in Varenna Symp. on Plasma Heating, 1972, p. 117.

9-7. R. Hawley and A. A. Zaky, Progress in Dielectrics 7, 200 (1967).

9-8. E. Thompson, in Proc. Second Symp. on Ion Sources and Formation of Ion Beams, 1974 (Berkeley, CA, 1974), papers II-3, II-7.

9-9. W. S. Cooper. Private communication (1974).

9-10. W. S. Cooper, K. Halbach, and S. B. Magyary, in Proc. Second Symp. on Ion Sources and Formation of Ion Beams, 1974 (Berkeley, CA, 1974), paper II-1.

9-11. B. C. Howard, W. L. Barr, and R. W. Moir, Lawrence Livermore Laboratory Rept. UCRL-51557 (1974).

9-12. R. W. Moir, W. L. Barr, and G. A. Carlson, in Proc. Fifth Conf. on Plasma Physics and Controlled Nuclear Fusion Research, 1974 (Tokyo, Japan, 1974), IAEA-CN-33/106-G3-1.

9-13. C. G. Smith and G. Lewin, Vac. Sci. Technol. 3, 92 (1966).

9-14. A. K. Chargin and C. J. Anderson, in Proc. Fifth Symp. on Engineering Problems of Fusion Research, 1973 (Princeton, NJ, 1973), p. 421.

10. Tritium-Handling System

INTRODUCTION

The tritium systems described here for the hybrid fusion-fission reactor represent both new and expanded approaches when compared to those developed for the FERF reactor.[10-1] The major differences between the two sets of systems have evolved from the choice of a solid blanket breeding material for the hybrid reactor.

Most of the considerations discussed in this section are part of one of the three major areas of interest:

- Recovering fuel from the blanket material,
- Processing fuel for recycling to the reactor by means of a purification and isotopic separation system, and
- Containing tritium for environmental and personnel protection.

All systems designed to achieve these ends are provided in duplicate in order to insure a high degree of reliability and to permit repairs without shutting down the reactor. The total comprises a complete system for the recovery and processing of tritium. A new possibility, a vanadium diffuser, permits direct recovery of tritium from the blanket coolant. The largest uncertainties in the tritium-handling system relate to the physical-chemical properties of the blanket material.

Blanket Characteristics

As described in Section 6, lithium aluminate ($LiAlO_2$) was chosen as the blanket material for breeding tritium. The blanket contains 1.23×10^5 kg of $LiAlO_2$ with the lithium being enriched in ^6Li. The breeding ratio varies from 1.05 at start-up to 1.30 after 20 years; we used the latter value for designing the fuel-recovery system.

The lithium aluminate is contained as a powder clad in stainless steel cans, with high-velocity helium flow on the outside of the cans for cooling and low-velocity helium flow through the powder to pick up and carry away tritium. In the present design, both helium flows are later combined into a single coolant flow. The blanket also contains as a neutron moderator graphite at 4.5 to 1 volume ratio with the lithium aluminate. The graphite is also clad in stainless steel. Helium coolant will exit the blanket modules at 600°C and at a pressure of 20 atm (2.0 MPa).

Lithium aluminate is a stable ceramic with a melting point of ~1900°C. To reduce the blanket inventory of tritium and to enhance its diffusion into the helium stream, the lithium aluminate particles must be about 0.44 mm in diameter.[10-2]

The tritium inventory in the blanket depends upon the diffusion coefficient of tritium in lithium aluminate and on the partial pressure at which we are able to recover tritium from helium. This partial pressure, in turn, is related to the concentration of tritium at the lithium aluminate surface by Sievert's constant

$$k_s = \frac{N}{(P)^{1/2}} ,$$

where N = atom fraction of T in $LiAlO_2$

P = partial pressure of T_2, Torr.

Estimates of the partial pressure and inventory of the blanket tritium for one reactor design, UWMAK-II,[10-3] are 13.3 mPa (10^{-4} Torr) and 42.0 g, respectively. These values yield a Sievert's constant, $k_s = 1.07 \times 10^{-4}$ atom fraction $Torr^{1/2}$ on a lithium basis.

Because oxygen is available from AlO_2^- radicals remaining after lithium transmutation, i.e., part of the tritium will be released as T_2O.

$$^6LiAlO_2 + n \longrightarrow {}^3H^+ + {}^4He + AlO_2^-$$

$$2\ AlO_2^- \longrightarrow Al_2O_3 + O^= .$$

Wittenberg[10-4] has estimated that about 10% of the tritium will be present as T_2O. Tritium must be recovered at a rate of 81 μmol/s (the breeding rate). Hence, 73 μmol/s of T_2 and 8 μmol/s of T_2O will constitute the steady-state recovery rates.

We will design our recovery system to extract 22% of the T_2 gas and nearly all of the T_2O passing through it. We will process ~0.5% (6 kg/s) of the total helium flow, and we will allow the blanket inventory to increase until the T_2 partial pressure becomes 0.45 Pa. Because water will inhibit the diffusion of T_2 into our vanadium diffusion membrane, we must first remove nearly all of the T_2O.

If we assume that temperatures are similar to those in UWMAK-II, the blanket tritium inventory can now be calculated. To compensate for the portion of tritium

as T_2O, the T_2 pressure is taken as 0.51 Pa. Using the Sievert's constant given above, the blanket contains an atom fraction of 6.6×10^{-6} T in lithium, giving a blanket inventory of 37 g, which in turn reflects a hold-up time in the blanket of ~24 hours.[10-2] The tritium inventory in the helium coolant is less than 0.1 g.

These figures are only estimates; however, it is worth noting, if necessary, we could increase the blanket inventory over an order of magnitude in order to maintain our tritium partial pressure at our design assumption. This tritium would be tightly held when the reactor is cold. We could also redesign the fuel-recovery system to operate at a tritium partial pressure as low as one-fifth of that assumed here, but at increased cost. The graphite portion of the blanket has the advantage of providing a relatively low fire hazard compared to blankets materials such as liquid lithium.

Fuel-Recovery System

A schematic diagram of the fuel-recovery system is shown in Fig. 10-1. The system will proceed as follows, helium taken downstream of the power cycle heat exchanger at ~300°C:

- The gas is cooled to -20°C by a regenerative heat exchanger and refrigerator.
- Essentially all T_2O is removed by a molecular sieve bed.
- The gas is then reheated to 600°C.
- Part of the T_2 diffuses through a bank of permeable vanadium tubes.
- The final effluent is returned to the main helium stream.

To prevent fluidization and attrition of the sieve material,[10-5] the molecular sieve bed requires an area of 5.2 m^2. The bed contains 720 kg of type 5A sieve, giving a depth of 20 cm. In this short depth, gas flow is still highly turbulent, and good drying is insured. By operating at -20°C up to a maximum T_2O loading equivalent to 0.5 wt% H_2O, the bed will dry to an exit partial pressure of ~0.2 mPa of T_2O. Recovering 8 μmol/s of T_2O requires an inlet partial pressure of ~11 mPa of T_2O.

The bed can be regenerated to a residual loading that is equivalent to ~0.2

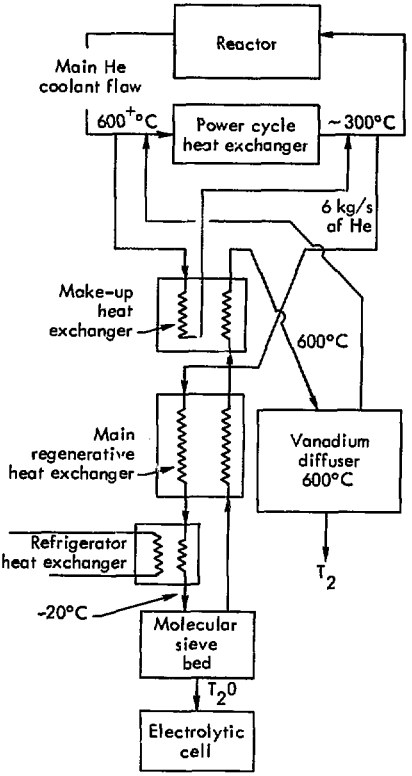

Fig. 10-1. Fuel recovery system.

wt% H_2O. The bed will have a total T_2O inventory equivalent to 1200 g of T_2, of which 720 g can be recovered and 480 g always stays on the sieve (residual). The bed capacity is equal to 172 days recovery of T_2O.

To regenerate this molecular sieve bed to a 0.2 wt% residual loading, a second molecular sieve bed must be used. Helium effluent at 315°C from the primary bed is cooled to 25°C and passed through the auxiliary bed. The latter contains 20 kg of 5A molecular sieve, and the loading is allowed to rise to ~12 wt% This bed, in turn, is regenerated at 315°C, and its effluent chilled to -25°C to collect the T_2O. When the auxiliary bed is not in use, its residual T_2 content will be 33 g.

Finally, the T_2O is decomposed, and T_2 gas is recovered for use. The T_2O recovered from the auxiliary molecular sieve bed is either sent to an electrolytic cell for electrolysis or reacted with a metal to release T_2.

A vanadium diffuser operating at 600°C separates T_2 gas from the reheated helium process stream. The diffuser contains a bank of vanadium tubes through which the helium passes. Tritium that diffuses through the tube walls is collected by pumps.

Vanadium was chosen over niobium for the diffusion medium because it is less subject to surface degradation by oxides.[10-6, 7] The vanadium surfaces can be also protected by a thin coating of palladium,[10-8] which is both very permeable to tritium and relatively insensitive to the presence of oxygen. Solid palladium tubes are prohibitively expensive in the sizes required.

The diffusion coefficient of tritium in vanadium was taken from Steward[10-8] for deuterium in vanadium:

$$D = D_0 \exp \frac{-E}{RT}$$

where: $D_0 = 3.3 \times 10^{-4}$ cm^2/s

$E = 7.1$ kJ/mol

$R = 8.314$ J/mol K

At 600°C, D equals 1.25×10^{-4} cm^2/s.

The solubility of tritium in vanadium was taken as the same as for hydrogen.[10-9] These data were extrapolated to 600°C and converted to a value for Sievert's constant k_s of 1.37×10^{-3} atom fraction/Torr$^{1/2}$. Tritium concentrations in vanadium tube walls were then calculated by assuming partial pressure values on each side of the wall. Tritium concentrations for any given partial pressures as calculated from data by Veleckis and Edwards[10-10] are slightly higher than those given above. Thus, the values arrived at here will be the more conservative.

With a helium flow of 6 kg/s and an entering tritium partial pressure of 0.45 Pa, a mass balance sets the tritium partial pressure at exit at 0.35 Pa to recover 73 μmol/s of T_2. This gives an average tritium pressure $\overline{P}_1$ in the diffuser of 0.40 Pa. Tritium passing through the vanadium tubes is pumped away at a pressure P_2 of 0.13 Pa. The corresponding concentrations, $\overline{C}_1$ and C_2, in the metal, as in Fig. 10-2, are 0.098 and 0.056 cm^{3}atm T_2/cm^{3}V, respectively. Embrittlement of vanadium does not occur until the hydrogen concentration is at least 18 times that experienced here.[10-11]

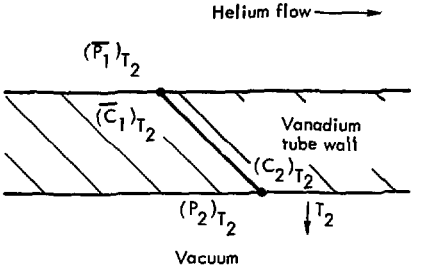

Fig. 10-2. Tritium diffusion through vanadium tube wall.

The problem is now to determine the area necessary to diffuse the required quantity of tritium.

We will plan on 14 60-mm-inside-diam vanadium tubes to handle the helium flow. Using an allowable stress of one-eighth of the rupture stress of vanadium at 600°C,[10-12] 31 MPa, the wall thickness, t, becomes 2 mm. The diffusion flow was approximated by the solution for a flat plate:

$$n = \frac{D(\overline{C}_1 - C_2)A}{t},$$

where $n = 1.63$ cm^3·atm/s of T_2 (73 μmol/s).

Solving for area A and converting area into tubes, the diffuser becomes an array of 14 2.4-m long tubes. Our computer code, DEMON-II, could be used to obtain a more detailed calculation of the permeation process, but this seems unwarranted at the present time.

The tritium pressure, P_2 is maintained at 0.13 Pa by pumping the tritium with two 10-inch mercury diffusion pumps equipped with cryotraps. For a cross section as shown in Fig. 10-3, the pumps need a speed of about 1000 ℓ/s each. The output is staged up to ~4.0 kPa using a mercury ejector pump,* followed by two valve-less "wabble-movement" pumps in series, to give a final P ~ 67 kPa.

This diffuser was designed as a simplified form of a separation process described by Hickman for a liquid-lithium blanket.[10-13] However, its final form is remarkably similar to that described by Watson,[10-14] and its performance principle is that suggested by Werner.[10-15]

The total drop in helium pressure within the fuel-recovery system is less than 20 kPa (~1%).

*Similar to Edwards Model 2M4B or XME3.

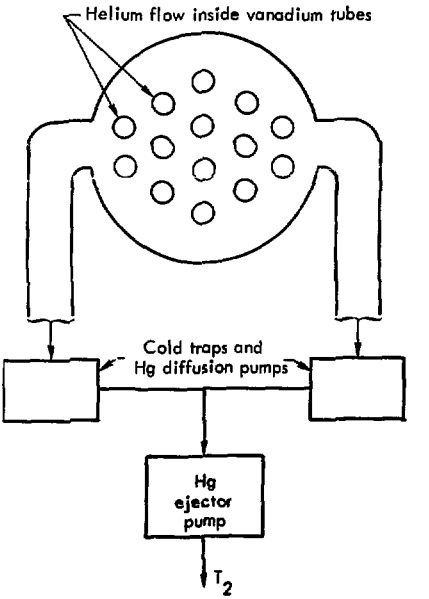

Fig. 10-3. Vanadium diffuser cross section.

The major cost of the fuel recovery system is the regenerative heat exchanger, which has a refrigerator and a make-up heat exchanger. These are conventional components, with each complete heat exchanger estimated at $1.3 million. Costs of the vanadium tubes for the diffuser are based on costs for stainless steel tubes certified for tritium use, much of the cost is for certification. The 25-mm-diam. stainless steel tubes cost ~$100/m of length. We estimate that 60-mm-diam. vanadium tubes will cost ~$330/m; when they have a palladium coating inside and out they will cost ~$660/m. The total cost of the material then becomes $34,000; the diffuser assemblies are estimated at $134,000 each. Molecular sieve beds with regenerative equipment will cost $72,500 each. Pumps and controls will cost $64,000 for each system. Finally, with installation and checkout, the fuel recovery systems will cost a total of $3,155,000 each.

FUEL RECOVERY DURING START-UP

The initial tritium breeding ratio for this reactor is 1.05. About 90% of the tritium (59 μmol/s) will be recovered in a continuous process as T_2 gas. The remainder (6 μmol/s) will be recovered as T_2O in a cyclical process which will take 210 days at this breeding ratio. Since the reactor will burn 62 μmol/s, an external supply of tritium equivalent to ~3 μmol/s (1.8 g/day) must be provided until the first T_2O is recovered from the molecular sieve beds.

We noted earlier that the molecular sieve beds always have a residual loading of 0.2 wt% water, and that they will be loaded to 0.5 wt% water equivalent as T_2O. During the first T_2O desorption cycle, we will get roughly proportional amounts of T_2O and of the residual water loading. This means that the first cycle will recover only 430 g of T_2, although 720 g of T_2 were absorbed (all as T_2O); the remaining tritium builds up the residual inventory on the molecular sieve beds. However, 430 g of T_2 is enough to meet all reactor requirements until the next desorption cycle, which will be a similar cycle for the second molecular sieve bed.

The initial residual loading of the molecular sieve beds will be D_2O. Then the mixtures of $(D, T)_2$ recovered [as $(D, T)_2O$] from early desorption cycles can be fed directly to the isotopic separator, without contamination from H_2.

The tritium breeding ratio increases to a value of 1.11 after about 5 years and reaches a constant value of 1.30 after 20 years. With the above start-up conditions, we can show that:

- The reactor will need an outside supply of 376 g of T_2 during the first 210 days, in addition to the starting inventory.
- No significant excess T_2 will be available during the first 2 years. After 2 years, the reactor will produce about 410 g/year of excess T_2.
- Excess T_2 will increase to 1300 g/year after 5 years, and to 3550 g/year after 20 years.

Alternate Systems

The system just described was chosen to give a continuous process for recovering tritium with a minimum inventory and to be compatible with a lithium aluminate

blanket. Two primary alternates can be considered:

- Addition of oxygen with lithium aluminate to collect all tritium as T_2O, or
- A lithium aluminum (LiAl) blanket to produce all tritium as T_2.

For the UWMAK-II reactor, it is proposed that 1.3 kPa of oxygen be used in the coolant to form T_2O.[10-3] The T_2 pressure then becomes vanishingly small, and very little tritium will diffuse through heat-exchanger tube walls into the steam power system. However, T_2O is many times more hazardous to personnel than T_2, is much more difficult to outgas, and equipment is harder to decontaminate for maintenance and repair purposes.

The hybrid fusion-fission reactor could operate with added oxygen, using the molecular sieve bed as described for all tritium as T_2O. The bed would then be regenerated on 17-day cycles, with inventories as described earlier. The vanadium diffuser and the make-up heat exchanger would be eliminated.

The second alternative, a blanket using a solid lithium alloy such as LiAl, is similar to that in the Brookhaven minimum-activity blanket.[10-16] Here, all tritium is present as T_2, and traces of impurities such as oxygen and water react with the blanket to form stable compounds. The molecular sieve bed and its heat exchangers are eliminated. Because the melting point of LiAl is 718°C, its service temperature must be much lower than lithium aluminate. The disadvantages of a T_2O system are avoided; however, as with our proposed fuel recovery system, T_2 in the helium could diffuse into th steam power system. We have not attempted to address this problem here.

At this time, we do not have enough information either on pertinent physical and chemical properties of blanket materials, or on reducing the diffusion of tritium in heat exchanger designs, to suggest a preferred alternate choice.

A uranium bed was considered in lieu of a vanadium diffuser for the present system and was rejected. To process enough helium, the size of the bed would have required inventories of at least many tens of kilograms of tritium.

PURIFICATION AND ISOTOPIC SEPARATION

A schematic of the hybrid fusion-fission reactor fuel system is shown in Fig. 10-4. The major components in the purification and isotopic separation system are the palladium diffusers and the isotopic separator. These components are closely patterned after those in the FERF reactor.[10-1]

This system is sized to handle the entire flow returning from the reactor [140 m mol $(D, T)_2$/s], and to separate it into streams of T_2 (37 m mol/s) and D_2 (103 m mol/s). Each stream must have a minimum isotopic purity of 90% for reinjection.

The entire system operates below atmospheric pressure, frequently under vacuum conditions. Special pumps minimize the possibility of leakage or contamination.

Palladium Diffusers

All gas returning from the reactor must be purified before it goes to the isotopic separator. The major impurities

are ^{3}He from radioactive decay of tritium (~1 μmol/s) and ^{4}He from the D-T burn (125 μmol/s). Traces of oxygen, nitrogen, and water can come from minor vacuum leaks and normal outgassing. Some methane production is expected also from radiolytic reaction between tritium and carbon compounds.[10-17]

The D-T gas is purified by diffusing it through hot (400°C) palladium-silver membranes. The process has been calculated using a computer code[10-18] and our design is simply scaled up in size from that for FERF.[10-1, 19] Figure 10-5 shows a schematic diagram of the process.

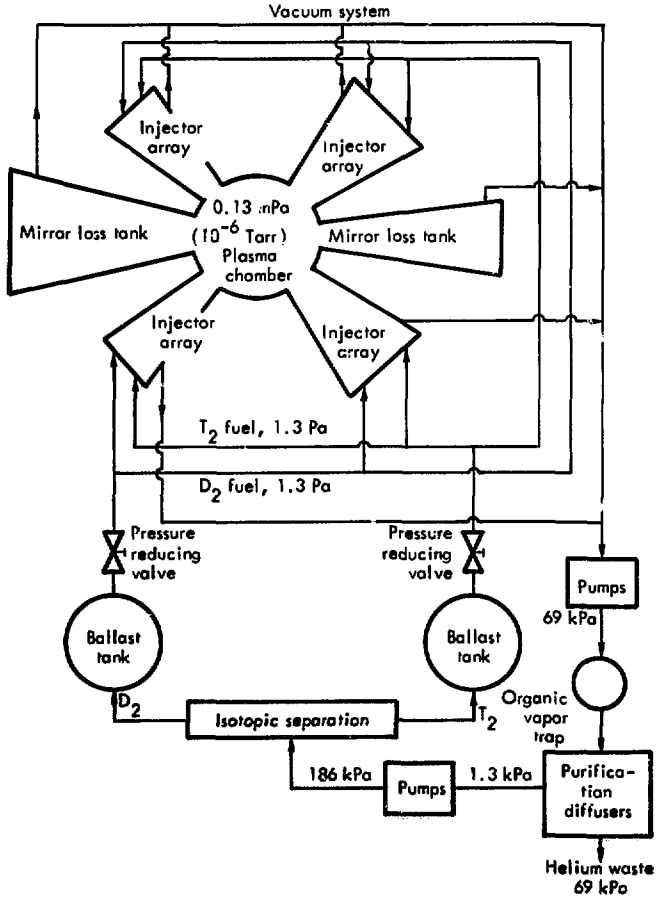

Fig. 10-4. Fuel system.

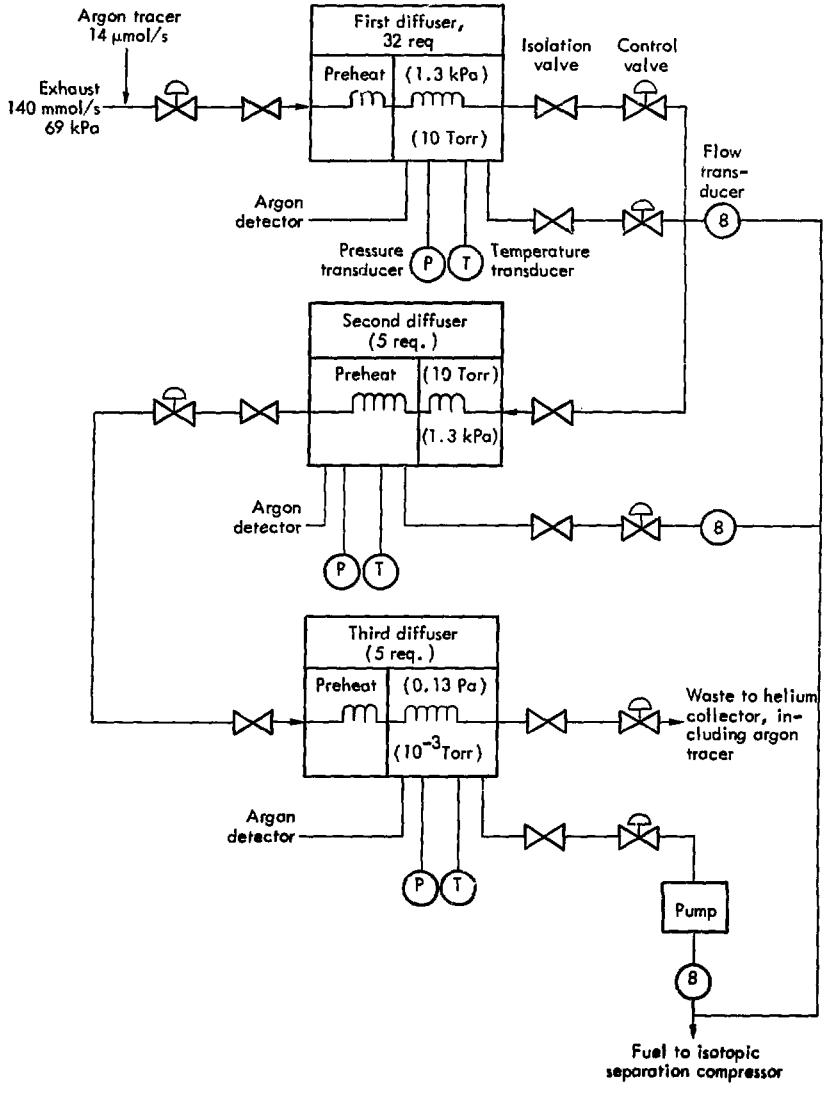

Fig. 10-5. Fuel purification system.

The purifier used 32 palladium-silver tubes, each 6.35 mm in diameter by 7.62 m long and having a 0.127-mm-thick wall. The tubes are connected in parallel. Impure gas at 69 kPa flows inside the tubes. Pure $(D, T)_2$ gas permeating the tubes is collected at 1.32 kPa; about 90% of the required flow will permeate this array of tubes.

Gas passing the first array is directed through a manifold into a second array of five identical tubes with the same operating conditions. Nearly all of the remaining $(D, T)_2$ is collected here. Finally, the remaining gas (now nearly all helium) passes into a third array of five tubes, each 1.27 mm in diameter by 7.62 m long, where the outside pressure is held at 0.13 Pa. Gas exiting these tubes is 99.9998% helium and other non-permeable gases. [10-20] A small mercury ejector pump (5 ℓ/s) will boost the $(D, T)_2$ gas from the third diffuser up to 1.32 kPa for collection with gas from the other two diffusers. All mercury pumps, here and elsewhere, must include cryotraps upstream and downstream to keep mercury vapor from the palladium.

An argon tracer is added as an impurity at the inlet. Argon detectors placed in the $(D, T)_2$ collection lines insure the integrity of the diffusers.

Costs for the palladium diffusers are based on those for the FERF design, with an allowance for inflation. The diffusers and furnaces will cost $677,500 for each set. Certified installation and checkout is estimated at 1.5 times the equipment cost (including that for auxiliary equipment).

Isotopic Separation of Deuterium and Tritium

Purified $(D, T)_2$ gas from the palladium diffusers is compressed to 186 kPa and sent directly to the cryogenic distillation columns. These columns are designed to process all fuel returning from the reactor. Gas from the diffusers will consist of 0.08 T_2, 0.40 DT, and 0.52 D_2, at a total rate of 140 mmol/s.

The design for the cryogenic distillation columns is patterned after that of Wilkes. [10-21] A schematic diagram of the components, indicating mass flows and compositions, is shown in Fig. 10-6. We have assumed that minor changes in Wilkes' design will accommodate the desired compositions and flow rates.

The two columns are 219 mm in diameter, with a combined height of 1.5 m. The bottom of column 1 requires a boiler rated at 2960 W, while the top of column 2 requires a refrigerator rated at 2960 W at 25 K. To convert part of the DT molecules into T_2 and D_2 molecules for further separation, a catalytic isotope equilibrator is used for the raffinate stream from column 2.

Gas returned as injector feed must have at least 90% isotopic purity for proper operation of the injectors, and this requirement is easily met. The separated fuel streams are returned immediately to the injectors for use before significant quantities of ^3He build up.

The isotopic separator contains about 1182 g (196 g moles) of liquid T_2 inventory, in a total inventory of 472 g mol of $(D, T)_2$ liquid. Loss of liquid helium in the cryostate would permit all of this to vaporize. Hence, adequate pressure relief devices must be provided for a

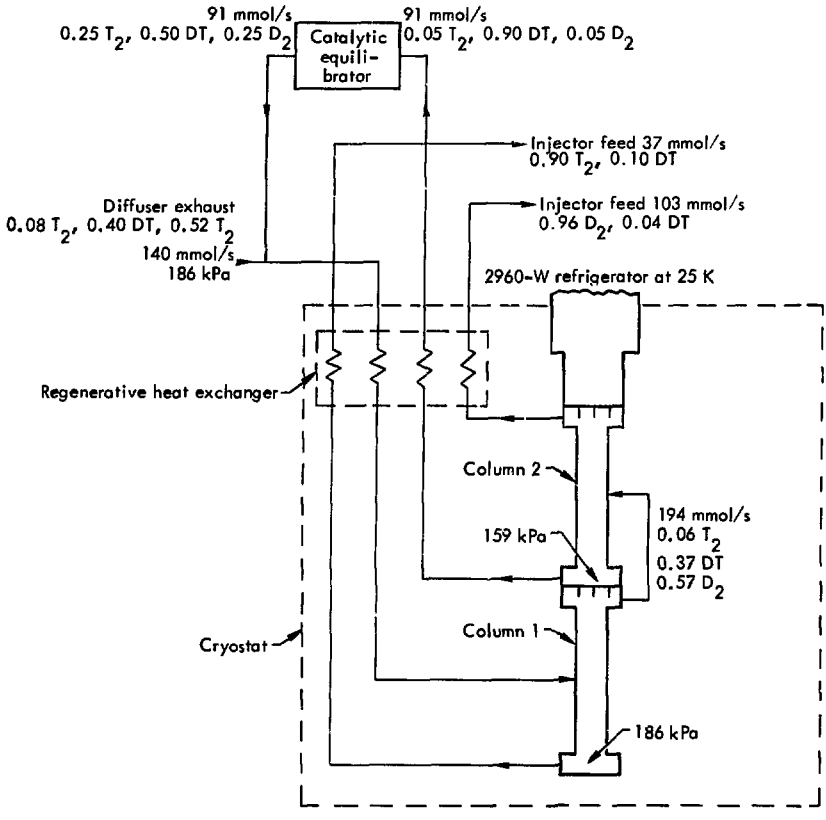

Fig. 10-6. Fuel isotopic separation system.

LOCA. Should a LOCA occur, the resulting gas would be vented into 160ℓ storage bottles.

Cryogenic stills are estimated to cost $297,500 each. The cryogenic refrigerators are estimated to cost $500,000 each. Because this installation is relatively simple, certified installation and checkout are estimated at $932,000; this is 0.6 times equipment costs (including auxiliary equipment costing $59,000).

Pumps

All of the fuel-handling processes require pumping of the $(D, T)_2$ gas, frequently starting at vacuum conditions. Primary requirements for all pumps are that they must not leak to the environment and must not contaminate the fuel. We have selected pumps that do not have moving shaft seals. All elastomer seals will be replaced with metal seals.

Gas from the mirror loss tanks and the injector cryopanels is pumped by mercury diffusion pumps and mercury ejectors to about 13 kPa. The gas must also pass a cryogenic trap to remove all traces of mercury. At a flow of 140 mmol/s and ambient temperature, the pumping rate is 26 ℓ/s.

A new "wabble" movement pump* has high pumping speeds in this pressure range. Compression is achieved by a piston with a "wabble" motion (roughly similar to a nutating piston meter) without valves, packing, or shaft seals. Two such pumps in series, each with a nominal displacement of 167 ℓ/s (600 m^3/hr)† will boost the gas to ~69 kPa for the palladium diffusers.

Purified gas from the palladium diffusers at 1.3 kPa is boosted to 13 kPa with a mercury ejector pump.** Two SRTI wabble pumps, as described above, will give 69 kPa. A diaphram compressor with a nominal displacement of 6 ℓ/s†† will provide final compression to 186 kPa for the isotopic separator.

All tritium pumping requirements can be met by combinations of these pumps. Hickman[10-19] also suggested the use of a gallium-filled Sprengel pump for FERF applications. This type is good for general service without staging, and can be designed to pump from ~1 Pa to >100 kPa. However, it has slow pumping speeds at very low pressures.

Commercial prices are available for or can be estimated for all pumps. The SRTI model scaled up 2.5 times in capacity is estimated at two times the PR 20 cost, or $40,000 each. A mercury ejector pump 12 times the capacity of the Edwards Model XME3 is estimated at 3.5 times the XME3 cost, or $87,500 each. Computer controls, certified installation, and checkout costs range from $15,000 to $20,000 per pump.

TRITIUM INVENTORY AND STORAGE

Estimated tritium inventories are given in Table 10-1. We have assumed a 10-day reserve of tritium for normal operations. The total inventory of tritium becomes ~4092 g. Note that 1746 g is tightly bound as T_2O on molecular sieve beds. Reactor start-up would require 2309 g of tritium, including the 10-day reserve.

Safe storage of the tritium must include a reservoir to abort the cryopanels and the isotopic separator in case of a liquid-helium coolant failure. This volume is for $(D, T)_2$ mixtures, and requires ~23 m^3 at atmospheric pressure. Tritium from the molecular sieve bed (batch process) and the reserve require another 4.5 m^3 of storage. To allow for flexibility, a total storage of 40 m^3 would be in the form of 250 tanks, each with a 160-ℓ volume. These tanks would be installed in a separate sealed vault and would be used only for storage.

Deuterium reserves are stored in high-pressure bottles outside the tritium storage vault.

*Societe de Recherches Techniques et Industrielles (SRTI) Dry and Air-Tight Mechanical Pump, Model PR-9 (developed for the French AEC).

†This would be 2.5 times the volume of the largest current model PR 20.

**Similar to, but 12 times the size of, Edwards Vacuum Components Model XME3.

††Similar to Pressure Products Industries Model 3235.

Table 10-1. Estimated tritium inventories.

Location	Amount (g)
Lithium aluminate blanket	37
Helium coolant	<0.1
Working molecular sieve bed (maximum)	1200
Stand-by molecular sieve bed (residual)	480
Auxiliary molecular sieve beds (residual, 2 beds)	66
Cryopanels[a]	803
Isotopic separator	1182
10-day tritium reserve	324
Total Inventory:	4092 g

[a]This assumes that all cryopanels are taken through a "defrost" condition every 2 hours by processing one-fourth of the cryopanels every 30 minutes.

We are currently buying 30-ℓ bottles certified for tritium storage for $1000 each. In quantity, 160-ℓ bottles should cost no more than $2000 each. Certified installation and checkout will cost about $7500 each.

TRITIUM CONTAINMENT

The basic concepts of tritium containment outlined for the FERF reactor[10-1,19] are directly applicable here. We will concern ourselves here primarily with new or modified concepts that affect permeation through hot walls, and with secondary containment as applied to the use of tritium recovery systems.

Those subjects covered by Hickman[10-1,19] for the FERF reactor that can be applied here without further elaboration include:

- Calculations for off-site exposures due to accidental or intentional releases.
- The fact that boron, which is used as a neutron shield to protect the magnets, can undergo several nuclear reactions to produce tritium.
- Monitoring and personnel protection procedures.

Secondary Containment

We are concerned both with the possible escape of tritium to the environment and with possible leakage of air into the reactor systems. Hickman[10-1, 19] has discussed the hazards associated with the entry of oxygen into the tritium systems. Leak-tight, metal-lined rooms were proposed as a secondary container for areas in which large quantities of tritium are handled, e.g., the reactor room, fuel processing and storage rooms, and main and secondary effluent-recovery rooms. In addition, the reactor room and the fuel-processing and storage rooms will be filled with nitrogen or argon. With either of these atmospheres, explosive mixtures can not occur in case of leakage into the tritium systems and, should there be a tritium leak, T_2O will not be formed in the rooms.

Main Effluent-Recovery System

The main effluent-recovery system (ERS) removes any tritium escaping into the reactor room or the fuel processing rooms. This system consists (see Fig. 10-7) of a catalyst bed to convert T_2 to T_2O, molecular sieve beds to trap the T_2O, and provision for isotopic swamping with H_2O.[10-1,19] This equipment should reduce the tritium content to ~500 $\mu Ci/m^3$. For flexibility, the main ERS is divided into several in-parallel ERS units. Only two of the ERS units need preheaters for the catalyst beds; the catalysts need be heated only in the presence of impurities such as hydrocarbons, carbon monoxide, or carbon dioxide.

The sizes involved require treatment of large quantities of gas. The reactor room contains ~350,000 m^3, and simple dilution calculations indicate that 12 to 16 volume changes are needed to get down to a level of 500 $\mu Ci/m^3$. However, our experience suggests that as many as 40 volume changes are necessary at low levels, especially where surfaces may adsorb and desorb T_2 or T_2O readily. Thus, if entry is planned within 24 hours of a tritium spill, the system must be able to handle ~160 m^3/s. Even then,

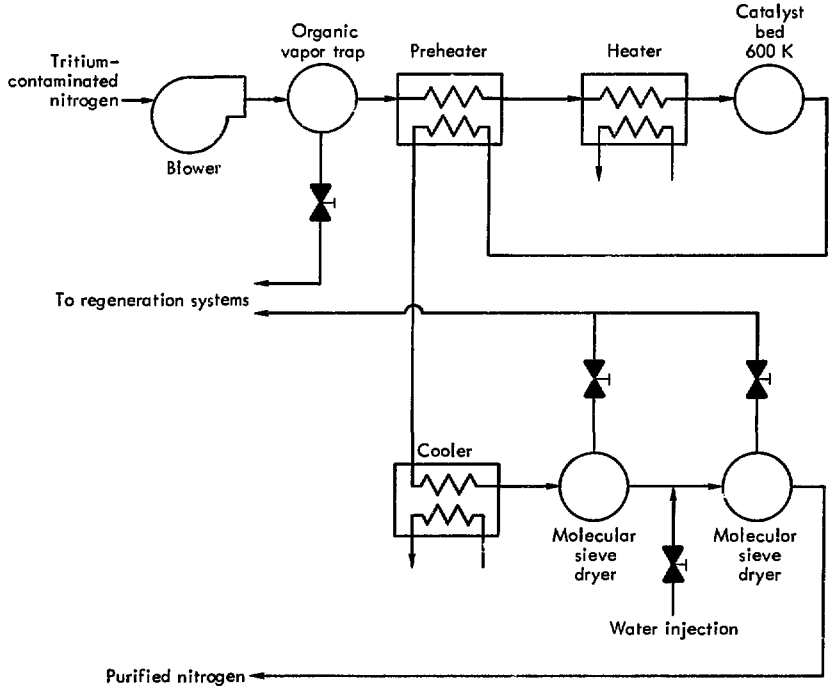

Fig. 10-7. Schematic of effluent recovery system.

for working in the inert atmosphere, personnel must wear protective suits and have independent air supplies.

Opening large pieces of equipment contaminated with tritium poses problems of additional release, even if inside the metal rooms. Hickman described outgassing procedures to reduce this problem.[10-1,19] Additional control can be achieved with portable hoods and ducting over the area to be opened, similar to conventional flush hoods for handling tritium, using part of the nitrogen flow to the main ERS. This is an effective method of tritium control.[10-22]

The "worst accident" situation involving the tritium systems would be a rupture of the helium coolant into the plasma chamber or injector areas. This would result in rapid boil-off of all $(D, T)_2$ on the injector cryopanels into large amounts of helium; the emergency tritium storage tanks would be inadequate. In this case, the $(D, T)_2$ would be recovered from the helium by converting it into $(D, T)_2O$ using controlled amounts of oxygen while passing the contaminated helium through one of the ERS catalyst beds. The helium and $(D, T)_2O$ stream would then be diverted to one of the molecular sieve beds in the fuel-recovery system to remove the $(D, T)_2O$. Later, the $(D, T)_2O$ could be recovered and reprocessed as described earlier. The ERS molecular sieve beds are designed for large-volume atmosphere control, but not for rapid recovery of tritium for reuse. The vanadium diffuser would not be used, since the high $(D, T)_2$ concentrations could lead to embrittlement.

A 0.08-m^3/s capacity system being constructed at Sandia Laboratories Livermore will have a cost equivalent to \$5,000,000 per m^3/s capacity. The FERF design had a capacity of 50 m^3/s, at a cost equivalent to \$374,000 per m^3/s capacity. Construction of this main ERS (169 m^3/s) might permit further reductions to an estimated cost of \$330,000 per m^3/s capacity.

Secondary Effluent-Recovery System

The main ERS rooms must be treated in a similar manner by a secondary ERS, except that the atmosphere can be air. These areas can be entered within 4.8 hours by treating ~4.6 m^3/s. To reduce the tritium exhausted to the atmosphere, air locks to enter these areas for maintenance can also be treated like a "flush hood."

Permeation of Hot Walls

The required handling of hot helium containing low partial pressures of tritium exposes large areas to potential tritium permeation. A new type of "getter wall" is proposed for these areas, as well as for the outer wall of the reactor.

The getter wall includes a structural wall, probably of stainless steel, that forms a diffusion barrier to the tritium. The outside of the structural wall is coated with a getter material, e.g., titanium, zirconium, or scandium, that form stable tritides. The getter material need react only with the small amounts of hydrogen isotopes permeating the structural wall, and a thin coating will last a long time. The outside surface of the getter is covered either by a protective metal layer or by an inert atmosphere inside an outer skin.

Because the getter wall must operate reasonably near ambient temperature, the helium lines would require a vacuum gap or some other thermal barrier.

REFERENCES

10-1. T. H. Batzer et al., Conceptual Design of a Mirror Reactor for a Fusion Engineering Research Facility (FERF), Lawrence Livermore Laboratory Rept. UCRL-51617 (1973).

10-2. R. H. Wiswall and E. Wirring, The Removal of Tritium from Solid CTR Blanket Materials; A Progress Report, Brookhaven National Laboratory Rept. BNL-19766 (1975).

10-3. R. W. Conn et al., "Major Design Features of the Conceptual D-T Tokamak Power Reactor, UWMAK-II," in Proc. Fifth Conf. on Plasma Physics Controlled Nuclear Fusion, 1974 (IAEA, Tokyo, Japan, 1974), IAEA-CN-33/G1-2.

10-4. L. J. Wittenberg, "Materials for Nonmobile Blankets," in Trans. Amer. Nuc. Soc., 1974 Winter Meeting (1974).

10-5. E. Ledoux, Chem. Eng. 55, 118-9 (1948).

10-6. V. A. Maroni, J. Nucl. Mat. 53, 293-8 (1974).

10-7. T. S. Elleman and K. Verghese, J. Nucl. Mater. 53, 299-306 (1974).

10-8. S. A. Steward, Diffusion and Solubility of Hydrogen and Deuterium in the Group VB Transition Metals, Dissertation, Arizona State University (1974).

10-9. R. Griffiths, J. A. Pryde, and A. Righini-Brand, J. Chem. Soc. (Faraday Trans. I) 68, 2344-49 (1972).

10-10. E. Veleckis and R. K. Edwards, J. Phys. Chem. 73, 683-92 (1969).

10-11. B. A. Kolachev, Vodorodnaya Khrupkost' Tsvetnykh Metallov, (Izdatel'stvo Metallurgiya, Moscow, 1966); Hydrogen Embrittlement of Nonferrous Metals, trans. by Ch. Nisenbaum, Israel Program for Scientific Translations, (S. Monson, Jerusalem, 1968).

10-12. W. Rostoker, The Metallurgy of Vanadium (J. Wiley & Sons, 1958).

10-13. R. G. Hickman, Nucl. Technol. 21, 39-49 (1974).

10-14. J. S. Watson, An Evaluation of Methods for Recovering Tritium from the Blankets or Coolant Systems of Fusion Reactors, Oak Ridge National Laboratory Rept. ORNL-TM-3794 (1972).

10-15. R. W. Werner, Heat Pipes for Recovery of Tritium in Thermonuclear Reactor Blankets, Lawrence Livermore Laboratory Rept. UCRL-72329 (1970).

10-16. J. Powell et al., "Minimum Activity Blankets Using Aluminum Structure," in Proc. First Topical Meeting on the Technology of Controlled Nuclear Fusion, CONF-740402, April 16-18, 1974.

10-17. V. P. Gede, Lawrence Livermore Laboratory, private communication (1975).

10-18. F. J. Ackerman and G. T. Koskinas, "A Model for Predicting the Permeation of Hydrogen - Deuterium - Inert Gas Mixtures

Through Palladium Tubes," Ind. Eng. Chem. Fund. 11, 332 (1972).
10-19. R. G. Hickman, Tritium in the Fusion Engineering Research Facility, Lawrence Livermore Laboratory Rept. UCRL-75354 (1974).
10-20. F. J. Ackerman, Lawrence Livermore Laboratory, private communication to R. G. Hickman (1974).
10-21. W. R. Wilkes, Monsanto Research Corporation, Mound Laboratory, private communication to R. G. Hickman (1973).
10-22. C. L. Folkers and K. A. Johnson, Repairing a Large Tritium-Contaminated System, Lawrence Livermore Laboratory Rept. UCRL-50850 (1970).

11. Cost Analysis

This cost estimate is quite crude:

- It is an estimate made on a preliminary conception, not on a finished engineering design.
- The cost estimate itself is a broad look rather than the really carefully detailed study which a project of this magnitude would require before one embarked on actual construction.

Nevertheless, developing an estimate enables us to understand the relative costs of the various components and to make rough comparisons with other preliminary designs.

CAPITAL COSTS

In estimating the capital costs, we have followed the general rules outlined in Ref. 11-1. We have not, however, tried to fit our individual items into the numbered account system that was designed for fission reactors. Costs for the nuclear island, for the thermal conversion system, and for building and facilities are detailed in Tables 11-1, 11-2, and 11-3, respectively, and summarized in Table 11-4. Plant operation and maintenance costs are listed in Table 11-5. Power costs are summarized in Table 11-6.

Superconducting Coil Winding

The cost of the superconductor, $2/kA·m, is based on 1972 superconductor costs plus stabilizing material and is conservative for very large-scale production. This may be reduced a factor of about 2.[11-2] The cost of the insulation, winding fixtures, winding, and assembly and installation is based on recent experience at LLL in building superconducting coils.

Coil Structure and Thermal Shield

Unit costs for the coil tanks, coil clamps, nitrogen-cooled shields, and reflective heat shields are based on similar costs developed for FERF,[11-3] with allowance for subsequent inflation. The FERF costs were in turn based on informal inquiries to industry.

Coil Refrigeration System

Coil refrigeration system costs are based on informal inquiries to industry.

Power Supplies

Power supply costs are based on recent LLL experience.

Ion Sources

Ion sources costs are based on projections from Lawrence Berkeley Laboratory experience in building Berkeley-type sources.

Uranium Blanket

In accordance with Ref. 11-1, p. 3-1, "The investment costs of the first core loading is not included (in the capital costs) but is considered in the calculation of fuel costs." We have therefore not shown the cost of either the uranium carbide or the lithium aluminum oxide under capital costs. Instead, we have allowed for these under operating costs.

Other parts associated with the blanket are based on current unit costs.

Helium Cooling System and Thermal Power System

The costs of the helium circulators, the steam generators, and the turbo-generators are based on informal inquiries to industry.

Direct Energy Converters

The costs of the components of the direct converters are based on costs developed for Ref. 11-4, which were in turn based on informal inquiries to industry.

Miscellaneous

The costs of the vacuum envelope, shielding, module handling system, diagnostics, controls and instrumentation, etc., are based on current unit costs, LLL and LBL experience, and (it must be admitted) plain guesses.

Tritium System

Costs for commercially available equipment are based on current prices with allowances for larger sizes as required. These items include molecular sieve beds, pumps, storage tanks, and cryogenic refrigerators. Costs for other equipment such as diffusers are estimated from costs for the closest comparable equipment certified for tritium service at LLL. Installation costs are estimated from the relative complexity of the various systems, and also reflect our current experiences for handling tritium.

Site Costs

In regard to site costs, Ref. 11-1 suggests "When other information is not available, use a cost of $500,000 for plants larger than 750 MW_t. For smaller plants between 500 and 750 MW_t, assume that the cost varies linearly between $250,000 and $500,000." This reference is, however, dated 1969; therefore, we have assumed a site cost of $1 million.

Building, Ancilliary Equipment, and Utilities

Cost for these items are based on current unit costs, LLL experience, and informal inquiries to industry.

Escalation

In accordance with Ref. 11-1, escalation is not included.

Engineering

Engineering is included using the graphs shown in Ref. 11-1. Percentages

for engineering on the thermal conversion system and buildings and facilities are taken from Fig. C-1. Engineering costs for the Nuclear Island are extrapolated from Fig. C-2 using the curve for "Novel and Extrapolated Designs." The engineering costs taken from this latter curve seem to be very low indeed. This may be at least partially explained by the fact that under the Ref. 12-1 rules, page 3-2, "....it should be assumed that the plant is not a first-of-a-kind unit" and, "The cost estimate does not include the costs of the R&D programs which are necessary to establish the technical feasibility of specific design features . . ."

Contingency

Contingency is included using the factors recommended in Table C-3 of Ref. 11-1. A contingency of 20% is used for the nuclear island on the basis of "Novel Design." A contingency of 3% is used for the thermal conversion system on the basis of "Proven Design." A contingency of 5% is used for building and facilities.

Interest During Construction

Interest during construction is included based on Fig. C-3 on page C-5 of Ref. 11-1. Figure C-3 shows curves for interest rates of 4%, 6%, and 7.2%. Presumably, these rates were based on conditions in 1969. To be more realistic for today's conditions, we assume an interest rate of 8%. The length of the construction period is taken as 73 months based on a plant rating of 600 MW and "Novel Design" as per table on page 3-40 of Ref. 11-1. The overall interest for the 73-month period is then 24% extrapolating from Fig. C-3. This overall interest figure assumes the S-curve Expenditure versus Time curve shown in Fig. C-4.

Plant Operation and Maintenance

The operating and maintenance (O & M) costs are estimated using the methods and data given in Section 4 of Ref. 11-1.

The O & M costs are those associated with:

- Staffing;
- Consumable supplies and equipment;
- Coolant makeup;
- Outside support services;
- Nuclear liability insurance; and
- Miscellaneous.

The miscellaneous costs include such items as training, annual operating fees, travel, and office supplies.

The total estimated O & M costs are $2.5 million per year. At a plant duty factor of 0.8, 4.28×10^9 kWh of net electrical power are produced in an average year. Therefore, the unit O & M costs are 0.57 mills/kWh.

Other Costs

Other costs such as taxes, insurance, staff training, startup, general office and administrative costs, licensing, etc., are included as indicated in Ref. 11-1 on page 3-6 and Fig. C-1 (curve for "Account 93").

Temporary Facilities

The cost of temporary facilities used during construction are included as indicated in Ref. 11-1, page 3-6 and Fig. C-1 (curve for "Account 91").

FUEL-CYCLE COST ANALYSIS

This portion of the cost analysis is presented in Section 6 as part of the blanket and fuel management calculations. A fuel-cycle cost of -0.62 mills/kWh resulted from this analysis.

Table 11-1. Cost estimate details for nuclear island for hybrid fusion-fission reactor.

Item			Thousands of $[a]
Magnet			
Windings (Incl. auxiliary coils)			
Superconductor, NbTi, 1.08×10^{10} A·m @ $\$2 \times 10^{-3}$ A·m		$ 22,000	
Insulation		2,200	
Winding fixtures		1,000	
Winding		20,000	
Assembly & installation		2,000	
Total coil windings:			$ 47,200
Structure			
Coil tanks, 1.1×10^7 lb @ $5.20/lb (Incl. Fab.)		$ 57,000	
Coil clamps, 3.2×10^7 lb @ $3.70/lb (Incl. Fab.)		118,000	
Bolts, fittings, small parts		7,000	
Assembly & installation		18,000	
Total coil structure:			$200,000
Thermal shield			
Nitrogen-cooled panels, 4×10^4 ft^2 @ $20/ft^2		$ 800	
Reflective heat shields, 1.2×10^5 ft^2 @ $4/ft^2		500	
Fittings & small parts		200	
Installation		500	
Total coil thermal shield:			$ 2,000
Refrigeration system (incl. cryopumping)			
Helium refrigerator/liquifier (34,000 hp @ $1000/hp)		$ 34,000	
Liquid-helium storage Dewar		1,300	
Helium recovery system		10,500	
Liquid-nitrogen storage Dewar		2,000	
Installation costs		4,200	
Total coil refrigeration system:			$ 52,000
Power supplies			
900-kW power supply module			
Power supply	$ 90		
SCR switching & resister	25		
Firing circuits	15		
Total:	$130		
Modules, 8 @ $130 $\times 10^3$		$ 1,040	
SCR contactor		90	
Total power supplies:			$ 1,130
Total superconducting magnet:			$302,330

Table 11-1 (continued)

Item		Thousands of $[a]	
Injectors			
Ion sources, 280 @ $60,000		$ 16,800	
Ion source power supplies			
Filament 60 Hz to 400 Hz converters			
42 MW @ $75/kW	$ 3,150		
Filament transformers, 280 @ $1500 Ea.	420		
Arc supplies, 136 kW, 280 @ $27 × 10^3	7,560		
Deuterium source, topping accel. P.S.			
250 kW, 140 @ $25 × 10^3	3,500		
Deuterium source, decel, P.S.			
26 kW, 140 @ $9 × 10^3	1,260		
Tritium source, topping P.S.			
250 kW, 140 @ $25 × 10^3	3,500		
Tritium source, decel, P.S. 140 @ $11×$10^3$	1,540		
Total power supplies:		$ 20,930	
Flapper valves & drives, 4 @ $25,000		100	
Base plate assemblies, 4 @ $100,000		400	
Internal shielding		50	
Cryopumping panels, 2000 ft^2 @ $100/$ft^2$		200	
Cryopumping panel removal mechanism		100	
Cooling water piping		50	
Assembly & installation		250	
Spares:		$ 38,880	
Ion sources, 70 (25%)		4,200	
Ion source power supplies (10%)		2,090	
Total injectors:			$ 45,170
Blanket			
Uranium blanket (Excl. handling gear, shielding and fuel)			
Carbon, $7.4 × 10^5 lb @ $2.30/lb		$ 1,700	
Stainless steel structure, $2.4 × 10^6 lb @ $5.20/lb		12,480	
Tracks & rollers		2,400	
Helium piping & valve assemblies		1,200	
Assembly & installation		10,000	
Total uranium blanket:			$ 27,780
Spare blanket modules, 25%:			7,000

Table 11-1 (continued)

Item	Thousands of $[a]	
Module-handling system		
Module carts (incl. drives), 4 @ $300,000	$ 1,200	
Caskets (4), lead, 8.0×10^5 lb @ $2.00/lb (Incl. Fab.)	1,600	
After-heat cooling systems, 4 @ $50,000	200	
Shielding plug handling device, 4 @ $50,000	200	
Tracks	1,000	
Assembly & installation	1,000	
Total module-handling system:		$ 5,200
Total blanket:		39,980
Shielding		
Magnet shielding		
Main magnet (coil and structure)		
Iron[b], 7×10^6 lb @ 3.0 $/lb	$ 21,000	
Lead, 2.6×10^5 lb @ 2.00 $/lb	530	
Boral, 8.6×10^3 ft^2 @ 30 $/ft^2	260	
	21,790	
Auxiliary magnet (coil and structure)		
Iron[b], 1.2×10^6 lb @ 3.0 $/lb	3,600	
Lead, 2.3×10^5 lb @ 2 $/lb	460	
Boral, 7.5×10^3 ft^2 @ 30 $/ft^2	230	
	4,290	
Biological shielding		
Internal concrete (encapsulated) concrete, 1.2×10^4 yd^3 @ 1000 $/yd^3	12,000	
Injector chambers (4)		
Inline, Iron[b], 1.25×10^6 lb @ 3 $/lb	3,750	
External, concrete 4.8×10^3 yd^3 @ 1000 $/yd^3	4,800	
	8,550	
Direct converter chambers (2)		
External, concrete, 1.05×10^4 yd^3 @ 1000 $/yd^3	10,500	
Bolts, fittings, piping	10,000	
Assembly & installation	10,000	
Total shielding cost:		$ 77,130
Direct energy converter		
Direct energy converters (mechanical, excl. vacuum envelope)		
Ribbons (incl. seals, spools, drives) 2800 @ $3000	$ 8,400	
Wires (incl. seals, spools, drives) 5600 @ $2000	11,200	
Insulators, shields	1,300	

Table 11-1 (continued)

Item	Thousands of $[a]	
Water-cooled liner	1,500	
Heat shields	500	
Total direct energy converters (mech.):		$ 22,900
Direct energy converter electrical system		
Power supplies	$ 360	
Bushings	70	
Cable	100	
Switchgear	70	
Total direct energy converter electrical system:		$ 600
Total direct energy converter:		$ 23,500
Vacuum system		
Vacuum envelope		
Main spherical tank, 5.7×10^5 lb @ $5.00/lb	$ 2,850	
Injector tanks (4), 3.2×10^5 lb @ $5.00/lb	1,600	
Expander tanks 7.7×10^5 lb @ $5.00/lb	3,850	
Gates for modules, 24 @ $100,000	2,400	
Expander tank structure	3,000	
Tank supports	1,000	
Misc. parts	500	
Installation	1,400	
Total vacuum envelope:		$ 16,600
Vacuum pumping system (Refrigeration incl. in coil refrigeration)		
Mechanical pumps	$ 720	
Valves	3,900	
Piping	430	
Cryopumping panels, 11,500 ft^2 @ $100/$ft^2$	1,150	
Nitrogen-cooled panels, 11,500 ft^2 @ $50/$ft^2$	580	
Reflective heat shields, 11,500 ft^2 @ $25/$ft^2$	290	
Miscellaneous parts	1,450	
Installation	2,170	
Total vacuum pumping system:		$ 10,690
Total vacuum system:		$ 27,290
Tritium system		
Purification & isotopic separation system	$ 5,080	
Fuel-recovery system	6,310	
Storage	1,880	

Table 11-1 (continued)

Item	Thousands of $[a]	
Containment	55,230	
Monitoring & personnel protection	990	
Tritium-associated shielding costs	200	
Total tritium system:		$ 69,690
Diagnostics	$ 750	
		$ 750
Plasma start-up equipment	$ 2,000	
		$ 2,000
Total nuclear island construction:		$587,840

[a] In 1975 dollars.

[b] A non-magnetic alloy of iron.

Table 11-2. Cost estimate details for thermal conversion system for hybrid fusion-fission reactor.

Item	Thousands of $[a]	
Helium cooling system		
Helium circulators, 4 @ $3.5 × 10^6	$14,000	
Helium manifolds, 4,200 ft @ $300/ft	1,260	
Helium leads to modules, 3,800 ft @ $100/ft	380	
Remotely operable joints, 4/mod. × 24 mod = 96 @ $5,000	480	
Installation	200	
Total helium cooling system:		$ 16,320
Steam system		
4 steam generators @ $12 × 10^6 (Installed)	$48,000	
Turbo-generators, 2 @ $22 × 10^6	44,000	
Switchgear, controls, installation	9,500	
Feedwater system, condensers, piping	20,000	
Total steam system:		$121,500
Electrical substation		
230-kV switchgear	$ 800	
230- to 138-kV transformers, 1000 MVA total	2,500	
13.8-kV switchgear and feeders	1,500	
13.8-kV to 480-V unit substations	8,000	
Total electrical substation:		$ 12,800
Cooling water system		
Cooling towers & associated equipment, 2000 MW	$ 9,600	
Water-treatment system	800	
Pumps & auxiliary	600	
Cooling-water distribution system	1,000	
Total cooling water system:		$ 12,000
Controls and instrumentation		$ 2,800
Total thermal conversion system:		$165,420

[a] In 1975 dollars.

Table 11-3. Cost estimate details for building and facilities for hybrid fusion-fission reactor.

Item	Thousands of $[a]	
Building		
Excavation	$ 200	
Piling	1,000	
Containment vessel	15,000	
Hot assembly & disassembly, 7,040 ft^2	1,060	
Generator room, 11,900 ft^2	1,190	
Penetrations (400)	160	
Low-bay areas, 110,360 ft^2	7,170	
Hydraulic shielding doors (2)	1,200	
Total building:		$26,980
Auxiliary equipment		
200-ton crane	$ 850	
Remote manipulators (incl. tooling)	6,000	
Radiation monitoring & control	200	
Shop equipment	400	
Viewing equipment (incl. windows)	2,000	
Total auxiliary equipment:		$ 9,450
Site		
Aquisition	$ 1,000	
Utilities	800	
Improvements (landscaping, roads, etc.)	600	
Total site:		$ 2,400
Total building, facilities, & site:		$38,830

[a] In 1975 dollars.

Table 11-4. Cost summary for hybrid fusion-fission reactor.

Item	Thousands of $[a]		
Nuclear island			
Magnet	302,330		
Injectors	45,170		
Blanket	39,980		
Shielding	77,130		
Direct energy converter	23,500		
Vacuum system	27,290		
Tritium system	69,690		
Diagnostics	750		
Plasma start-up equipment	2,000		
Total nuclear island construction (A):		587,840	
Engineering, 2.5% of (A):		14,700	
Contingency, 20% of (A):		117,570	
Total nuclear island:			720,110
Thermal conversion system			
Helium cooling system	16,320		
Steam system	121,500		
Electrical substation	12,800		
Cooling water system	12,000		
Controls and instrumentation	2,800		
Total thermal conversion system constr. (B):		165,420	
Engineering, 5.6% of (B):		9,260	
Contingency, 3% of (B):		4,960	
Total thermal conversion system:			179,640
Building, facilities, and site construction (C)		38,830	
Architect, engineering, 11% of (C)		4,270	
Contingency, 5% of (C)		1,940	
Total building, facilities, & site:			45,040
Temporary facilities, 0.4% of (A)+(B)+(C)			3,170
Other costs (taxes, insurance, training, start-up, administration, licensing, etc.) 3.6% of (A)+(B)+(C)			28,520
Total (D):			976,480
Interest during construction, 24% of (D)			234,360
Total plant cost:			1,210,480

[a] In 1975 dollars.

Table 11-5. Summary of annual costs for plant operation and maintenance.

Item		Thousands of $
Staff payroll[a]		1,090
Fringe benefits, 10%[a]		109
	Subtotal:	1,199
Blanket submodule replacement[b]		190
Consumable supplies and equipment[c]		510
Outside support services[c]		180
Miscellaneous O & M costs[c]		105
	Subtotal:	985
General and administrative[d]		148
Coolant makeup[e]		7
Nuclear liability insurance[f]		300
	Subtotal:	455
	Total annual direct costs (excluding fuel):	2,639
Interest at 10% on O & M working capital[g]		39
	Total annual O & M cost (excluding fuel):	2,678

[a]Staffing costs taken from Tables 4-2 and 4-4, Ref. 11-1, (for a 750-MW_e plant) and increased 50% to account for escalation.

[b]Replacement of blanket submodules (structure) after an integrated 14-MeV neutron wall loading of 5 MWy/m^2 (a first-wall 14-MeV neutron fluence of $\sim 8 \times 10^{21}$ n/cm^2).

[c]Cost taken from Table 4-5, Ref. 11-1, (for a 750-MW_e plant) and escalated 50%.

[d]15% of preceding subtotal per Table 4-1, Ref. 11-1.

[e]20% loss of He inventory at 0.12 $/$ft^3$ STP. Reference page 4-17 and Table 0-2, Ref. 11-1. A 50% escalation is included.

[f]Insurance cost taken from Table 4-6, Ref. 11-1, for a 750-MW_e plant.

[g]As outlined in Table 4-7, Ref. 11-1.

Table 11-6. Summary of electric energy generation costs.

Cost component	Capital Cost ($\$ \times 10^3$)	Fixed Charge Rate (%)	Annual cost ($\$ \times 10^3$)	Unit energy cost (mills/kWh)
Plant investment:				
Depreciating assets	1,217,000	14[a]	170,380	39.7
Fuel:				
Unit direct cost	–	–	-11,900	-2.77
Unit indirect cost	92,000	10	9,200	2.15
Subtotal:				[illegible]63
Operation & maintenance:				
Direct cost	–	–	2,640	
Working capital	390	10	39	0.63
Subtotal:			2,679	
Total electric energy generation cost:				39.7

[a]From Table 2-1 of Ref. 11-1.

REFERENCES

11-1. Guide for Economic Evaluation of Nuclear Reactor Plant Designs, NUS Corp. Rept. NUS-531 (1969).

11-2. J. R. Powell, "Design and Economics of Large D.C. Fusion Magnets," in Proc. Conf. Applied Superconductivity, 1972 (Annapolis, MD, 1972), IEEE 72CHO682-5-TABSC, p. 346.

11-3. T. H. Batzer et al., Conceptual Design of a Mirror Reactor for a Fusion Engineering Research Facility (FERF), Lawrence Livermore Laboratory Rept. UCRL-51617 (1974).

11-4. W. L. Barr, R. J. Burleigh, W. L. Dexter, R. W. Moir, and R. R. Smith, IEEE Trans. Plasma Science, PS-2, 2, 71 (1974).

12. Parametric Analysis

The mirror hybrid fusion-fission reactor described here resulted from reasonable estimates of some parameters and rather arbitrary choices of others. To analyze the results of varying these parameters, we have chosen two quantities to use as figures of merit:

- The overall system efficiency, and
- The capital cost of the various components per kilowatt of electricity produced.

The value of the fuel produced is considered separately.

System efficiency, η_{system}, is defined as the ratio of the net power output to the total power produced both by fusion and by neutron-induced reactions in the blanket. From the power-flow diagram shown in Fig. 4-1, it is seen that η_{system} is given by

$$\eta_{system} = P_e/(0.2QP_{in} + 0.8QP_{in}M) \quad (12\text{-}1)$$

where the various quantities were defined in Section 5 and listed in Table 5-1 for the reference design. P_e is expressed in terms of P_{in} and the other parameters in Section 4 (Eq. (4-1)).

One important variable that does not appear explicitly in P_e or η_{system} is the injection energy. Since $W_{T,in} = (3/2)W_{D,in}$ and the mean energy of the trapped plasma ions is also roughly proportional to $W_{D,in}$, we consider the variation of $W_{D,in}$ assuming that all energies vary proportionally.

Figure 12-1 shows Q plotted as a function of $W_{D,in}$. We normalized the curve to give our reference value of $Q = 0.935$ at $W_{D,in} = 100$ keV and we assume that Q is proportional to $W_{D,in}^{1/2}$ and to $(\sigma v)_{DT}$, as indicated by Eq. (5-5), and that $n\tau \propto W_{D,in}^{3/2}$. The curve rises rapidly with energy below $W_{D,in} \sim 150$ keV, and is flat above that energy. The Fokker-Planck calculations of Futch et al.[12-1] show that this scaling of Q with energy is accurate when the α particles do not thermalize in the plasma, as is the case here. When the α's are confined, Q peaks around 150 to 200 keV and then declines at higher energy.

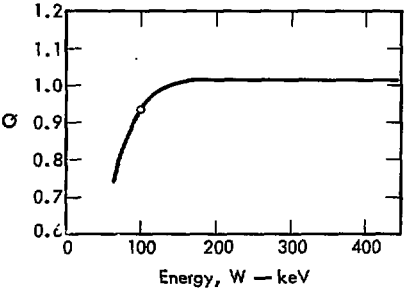

Fig. 12-1. Variation of Q with energy. Line is drawn through the calculated design point, assuming $Q \propto (\sigma v)_{DT}\sqrt{W}$.

Taken alone, Q would suggest $W_{D,in} > 150$ keV. However, economics forces the use of $W_{D,in} < 150$ keV because:

- The cost of the magnet increases almost linearly with the energy of the ions to be confined, and
- Our decision to use positive ion accelerators in our injectors necessitates the use of lower energy.

The efficiency F of neutralizing energetic positive ions decreases rapidly with increasing energy. Figure 12-2 shows the injector efficiency, η_i, for the complete injection process: creation, acceleration, neutralization, and trapping; and including the direct conversion of unneutralized ions. The injector is discussed in Section 9, and the power-flow diagram for it is shown in Fig. 4-2. For comparison, the figure also includes the similar curve for negative ion acceleration, for which the efficiency of neutralization improves with increased energy.

The dashed curve in Fig. 12-3(a) shows the variation of the overall system efficiency, η_{system}, with $W_{D,in}$. Since

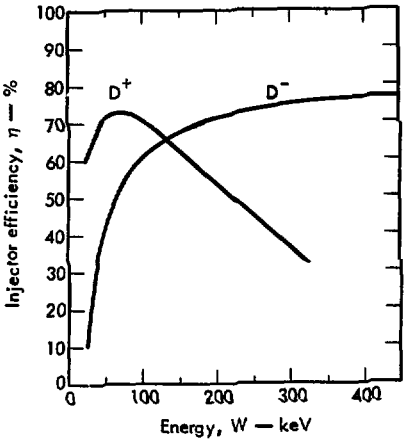

Fig. 12-2. Injector efficiency, including creation, acceleration, neutralization, and trapping.

$$P_e/P_{in} = \eta_{DC} + (1 - \eta_{DC} + 0.2Q)\,\eta_{Th2} + 0.8QM\eta_{Th1} - 1/\eta_i, \qquad (12\text{-}2)$$

and we assume that the efficiency, η_{DC}, of the direct energy converter is independent of energy. Eq. (12-1) shows that $W_{D,\,in}$ affects η_{system} only through Q and η_i. The injection energy $W_{D,\,in} = 100$ keV (and $W_{T,\,in} = 150$ keV) was chosen because it gives the maximum value of $\eta_{system} = 0.30$. It will be seen that economics suggests a lower energy. However, the problems associated with beam penetration into the plasma and of pumping the increased gas flow that would result from lower energy will prohibit any very significant decrease in energy.

To determine the effect on the capital cost of changes in the various physics parameters, a scaling law was established for each of the major components. The costs listed in Section 11 were taken as the reference point. Engineering, contingency, and interest costs are not included here. The components and the cost-scaling laws used are the following:

- Magnet cost, $C_{Mag} = \$302 \times 10^6$ in the present design, is assumed to vary as B^2 because most of the cost is in the support structure. It was shown in Section 5 that $\beta \propto \rho_\perp/B^2 \propto nW/B^2$; therefore, for a fixed β, $B^2 \propto nW$. Also, because $P_F \propto n^2\,(\sigma v)_{DT}$ and $P_F = Q\,P_{in}$, $n \propto \sqrt{Q\,P_{in}/(\sigma v)_{DT}}$. Finally then,

$$C_{Mag} = \$302 \times 10^6 \times \left(\frac{W_{D,\,in}}{100}\right) \sqrt{\frac{Q\,P_{in}}{210} \times \frac{9.2 \times 10^{-16}}{(\sigma v)_{DT}}}\,.$$

- Injector cost, $C_{inj} = \$47 \times 10^6$ in the present design, is assumed to vary directly as P_{in} because most of the cost is in the power supplies. We therefore take

$$C_{inj} = \$47 \times 10^6 \times (P_{in}/225).$$

- Blanket cost, $C_{B1} = \$40 \times 10^6$ in the present design, is assumed to depend almost entirely on geometry and internal structure because the fuel is listed as an operating cost. C_{B1} is therefore taken to be independent of the choice of physics parameters:

$$C_{B1} = \$40 \times 10^6.$$

- Shielding cost, $C_{sh} = \$77 \times 10^6$ in the present design, scales similarly to C_{B1}:

$$C_{sh} = \$77 \times 10^6.$$

- Direct energy converter cost, $C_{DC} = \$25 \times 10^6$ in the present design, scales directly with the power into the direct energy converter because the necessary surface area of collectors and the electrical equipment both scale that way:

$$C_{DC} = \$25 \times 10^6 \times (P_{in}/225).$$

- Thermal system cost, $C_{Th} = \$142 \times 10^6$ in the present design, scales approximately as the power output from the thermal system. We ignore the variation of the cost of the smaller bottoming cycle for the direct energy converter and for the beam direct converter in the injector system. Then,

$$C_{Th} = \$142 \times 10^6 \times (M/12)(Q\,P_{in}/210).$$

- "Other cost", C_{oth}, includes the vacuum system, tritium system, diagnostics, startup equipment, building site, and facilities. We assume C_{oth} is independent of the physics parameters and use the value given in Section 11:

$$C_{oth} = \$138 \times 10^6.$$

Figures 12-3(a) through 12-3(f) show the variation of individual and total component costs per kilowatt of electric power output. The scaling laws are used for the component costs, and Eq. (12-2) is used to give P_{in} in terms of P_e. In Fig. 12-3(a), the injection energy is varied and P_e is held fixed. Varying W changes Q and η_i and, through Eq. (12-2), it also changes P_{in}. Total component cost appears to minimize for $W_{D,\,in} = 65$ keV, but this is probably misleading. At such a low energy, the beam probably could not be made to penetrate into the large plasma. Also, the lower system efficiency and the lower energy both require higher injection currents and, therefore, a greater gas load on the vacuum system. These problems were ignored in the cost scaling.

Figure 12-3(b) shows how the cost / kW_e varies with Q when $W_{D,\,in}$ and P_{in} are held fixed. P_e therefore changes as Q is varied and is shown on a separate scale. In the present design, Q = 0.935, and the total component cost is \$1270/kW_e. The cost would become prohibitive if Q were significantly decreased, as might result from microinstabilities in the plasma. System efficiency, η_{system}, is also shown in the figure and is seen to decrease rapidly with a decrease in Q, going negative below Q = 0.2.

Figure 12-3(c) shows how the cost varies when P_e is varied by changing P_{in} with Q and $W_{D,\,in}$ held fixed. It is clear that the cost/kW_e decreases as the power is increased. However, the limited space available for injectors and problems with beam penetration and with gas pumping will limit how far P_e (and hence P_{in}) can be increased.

Figure 12-3(d) shows the variation in cost/kW_e when the magnetic field strength B is varied. Since the power generated increases as B^4 while the dominating magnet cost increases as B^2, there is a saving in \$/kW by going to higher fields. However, the assumed Nb-Ti superconductor can only be used up to $B_{conductor} = 9.0$ T. Higher fields require the use of Nb_3Sn, for which the technology has not yet been developed. Also, the present design of the support structure for the coil cannot be scaled

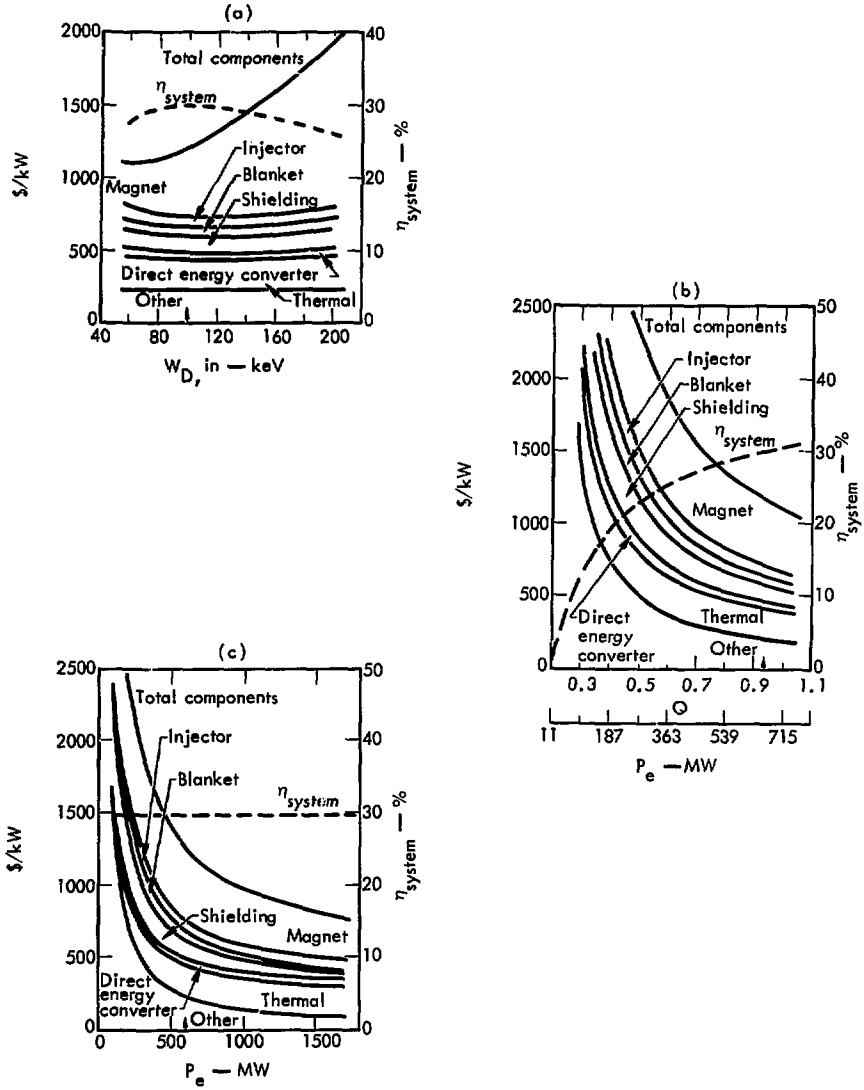

Fig. 12-3. Variation of system efficiency and component costs per kW_e output with various parameters (arrow indicates design point): (a) Varying $W_{D,in}$ with fixed P_e; (b) Varying Q with fixed $W_{D,in}$ and P_{in}; (c) Varying P_e via P_{in} with fixed M, Q, W; (d) Varying B with fixed Q, M; (e) Varying M with fixed P_e; (f) Varying M with fixed P_{in}.

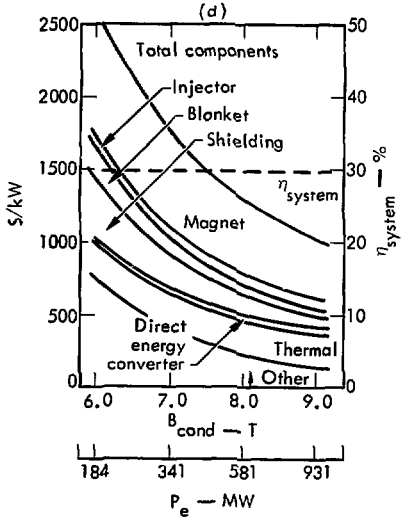
(d)
Total components
Injector
Blanket
Shielding
η_{system}
Magnet
Direct energy converter
Thermal
Other
$/kW
η_{system} — %
B_{cond} — T
P_e — MW

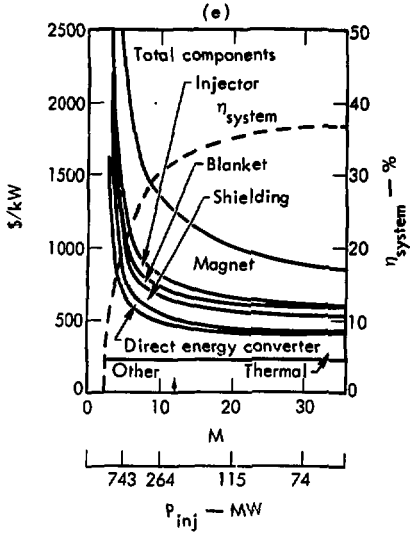
(e)
Total components
Injector
η_{system}
Blanket
Shielding
Magnet
Direct energy converter
Other
Thermal
$/kW
η_{system} — %
M
P_{inj} — MW

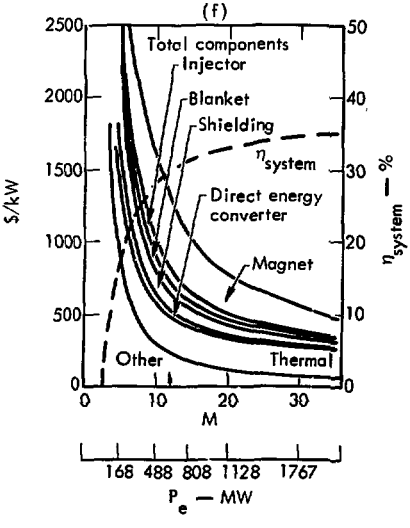
(f)
Total components
Injector
Blanket
Shielding
η_{system}
Direct energy converter
Magnet
Other
Thermal
$/kW
η_{system} — %
M
P_e — MW

up indefinitely (see Section 7). Since $P_e \propto B^4$, Figs. 12-3(c) and 12-3(d) show the same effects, and the same limiting factors apply to both.

Figures 12-3(e) and 12-3(f) show the effect of changing the blanket multiplication, M. In Fig. 12-3(e), P_e is held fixed so that as M is increased P_{in} is decreased to maintain the same output power. In Fig. 12-3(f), P_{in} is held fixed and P_e is allowed to increase as M is increased. Thus, the cost/kW_e of most components decreases nearly as P_e^{-1}, much faster than in Fig. 12-3(e) where P_e was fixed. Clearly, there is a strong economic incentive to increase M and hence P_e. The blanket in the present design (M = 12) uses natural uranium. To increase M, the blanket must contain enriched uranium.

Finally, Fig. 12-4 shows the effect on cost/kW_e and on system efficiency of using neutral beams produced from negative ions. Since the efficiency of neutralization of negative ions increases with energy, the injector efficiency (see Fig. 12-2) and the system efficiency also increase. However, the cost of the magnet increases almost linearly with ion energy, and this practically cancels the gain from higher efficiency at high energy. As is clear from comparing Figs. 12-3(a) and 12-4, at lower energy ($W_{D,in} < 140$ keV), positive ion-acceleration is better than negative ion acceleration.

The direct energy converter cannot be varied in a continuous manner. There are essentially three choices:

- A one-stage unit giving $\eta_{DC} = 0.50$ followed by a thermal cycle with $\eta_{Th2} = 0.35$ (the present design),
- A simple plasma dump with $\eta_{DC} = 0$ and $\eta_{Th2} = \eta_{Th1} = 0.38$, or
- A multistage unit giving perhaps $\eta_{DC} = 0.70$ followed by $\eta_{Th2} = 0.35$.

We compare the three cases in Table 12-1, where $P_{in} = 225$ MW in all three. Equations (12-1) and (12-2) give η_{system} and P_e. The component costs shown in the table were obtained from the scaling laws presented earlier by considering the power flow in the three cases. Since P_{in} is the same in all three, only the direct energy converter, the injector (its power supplies change), and the thermal converter are different in the three cases.

The effect of removing the direct energy converter (compare Case 2 with Case 1) is to reduce the total component cost by 1% and to reduce the output power by 11%. The net result is that removing the direct energy converter results in a 10% increase in cost per kW_e.

In Case 3 ($\eta_{DC} = 0.70$), we assume the cost of the direct energy converter is increased by 60% over the reference case (Case 1). With this assumption, the increased cost is just compensated for by the extra 29-MW output, the $1 million saving on injector power supplies, and the $3 million saving on the thermal converter. However, the system efficiency is then increased to 31%.

REFERENCES

12-1. A. H. Futch, Jr., J. P. Holdren, J. Killeen, and A. A. Mirin, Plasma Phys. 14, 211 (1972).

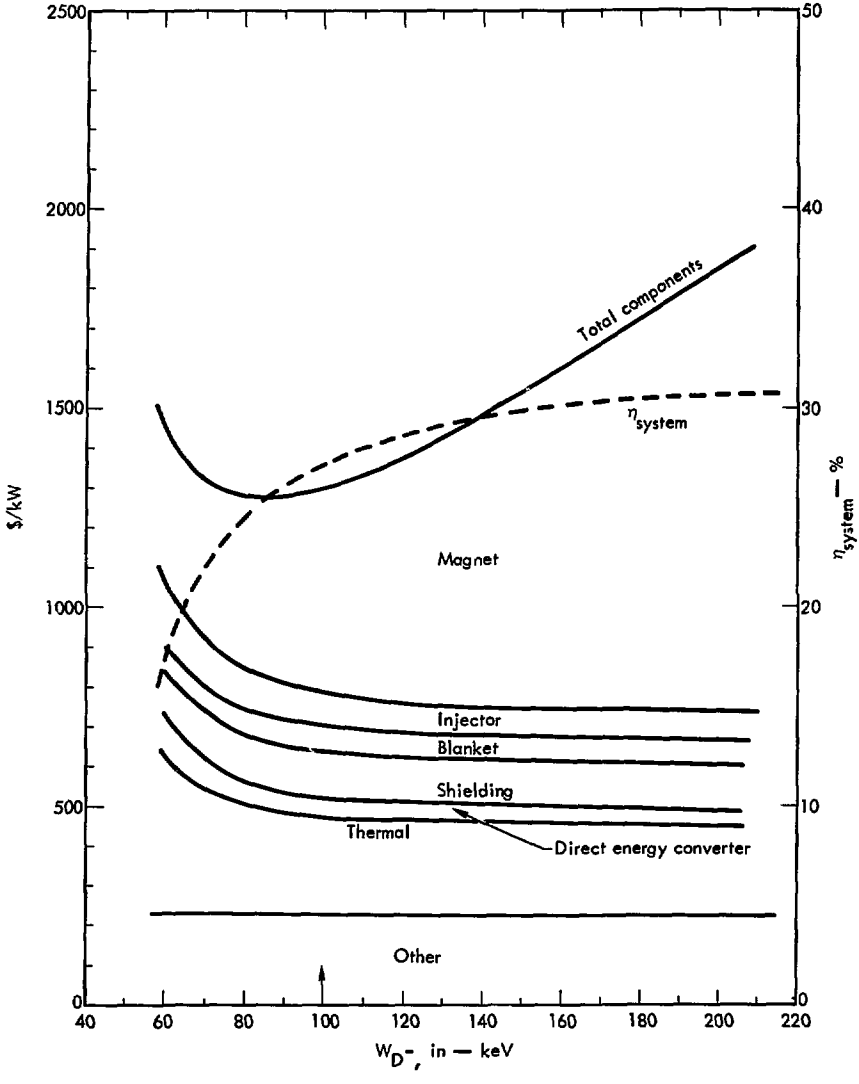

Fig. 12-4. Variation of system efficiency and component costs per kW_e output when varying W_{in} with fixed P_e, for D^- acceleration.

Table 12-1. Comparison of cost and efficiency with different direct energy converters, for P_{in} = 225 MW, Q = 0.935, M = 12, and η_{Th1} = 0.38.

	Case 1	Case 2	Case 3
Type of direct energy converter	one-stage	none	two-stage
Bottoming η_{Th2}	0.35	0.38	0.35
η_{DC}	0.50	0	0.70
P_e (MW)	611	546	640
η_{system}	0.297	0.266	0.311
C_M ($\$10^6$)	302	302	302
C_{inj} ($\$10^6$)	47	49.5	46
C_{Bl} ($\$10^6$)	40	40	40
C_{sh} ($\$10^6$)	77	77	77
C_{DC} ($\$10^6$)	25	0	40
C_{Th} ($\$10^6$)	142	157.5	139
C_{oth} ($\$10^6$)	138	138	138
C_{total} ($\$10^6$)	771	764	807
C_{total} ($/kW)	1262	1399	1261
ΔC_{total} ($/kW)	0	+137	-1

13. Future Work and Conclusions

During our present work, we have identified several areas for further work. They can be divided into two categories:

- Improvements on the basic design, and
- New designs.

In the first category, improvements on the basic design, the magnet stands out as the single most costly item; we have already begun work on superconducting magnet designs having much more efficient and lower-cost structural members. The uranium-bearing blanket modules turned out to be too heavy. However, now that we have shown one blanket module design that makes routine removal for changing uranium fuel and first-wall replacement at least possible, we will work on blanket module designs which are both lighter in weight and easier to handle. The cylindrical pressure vessel concept will also be further evaluated. In redesigning the modules, we will strive towards reducing the peak-to-average 14-MeV neutron flux so as to increase the power and thus decrease unit costs. The safety systems that prevent partial blanket melt in the case of a loss of flow of coolant have received little attention so far and will be worked on.

In the second category, new designs, we plan to design blankets that will be so safe that, should the cooling systems fail, the fuel pins will be cooled by

conduction, natural convection, and radiation to the ambient surroundings, thus preventing clad melting and release of fission products. This blanket would be passively safe from a LOCA. If a hybrid reactor could be designed (in a practical way) to be passively safe, and considering that a chain reaction is not possible, then, the hybrid would have a large potential environmental advantage. It is this environmental advantage that interests us in the passively safe blanket.

We shall continue investigating both fast-fission and thermal blankets, and we shall continue studying fuel cycles and fuel management schemes that optimize either fuel production or power production.

Appendix A. Fusion Electric Breeder

In a fusion electric breeder, electrical energy would be converted into fusion neutrons that produce fissile (^{233}U or ^{239}Pu) atoms from uranium or thorium by neutron capture but the nuclear heat would not be converted to electricity. This process is then analogous to the process of producing enriched fuel in a diffusion plant with an electric-power input. If the heat is not converted to electricity, the technical requirements on the blanket become easier because lower-temperature coolants can be used.

To assess the potential of the mirror reactor as a fusion electric breeder, we have modified our reference design in the following ways.

- The fusion power was doubled by increasing the magnetic field and doubling the injected current.
- The natural uranium in the metallic form rather than uranium carbide giving 2 times more fissile production (1.8 atom/fusion).

The cost estimate of the reference design was then modified and is given in Table A-1.

In producing 2760 kg of Pu per year, the plant will have to buy 418 MW_e of power and will dump 4116 MW of thermal power at a relatively low temperature (a few hundred °C). At an availability of 80%, a capital charge of 14%, and electricity cost of 20 mills/kWh, the plutonium could be sold for \$86/g (\$21/g due to cost of electricity, \$55/g due to cost of the capital investment, and ~\$10/g for fuel reprocessing and fabrication).

For this electric breeder to be practical, both electrical and capital costs would have to go down. Already, we have improved the capital cost compared to the reference case by raising the fuel production rate by a factor of 4.0 while increasing the capital cost by only 15%; still, the capital cost (as measured by \$55/g) is a factor of 5 or more too high. The electrical cost (as measured by \$21/g) is only about a factor of 2 too large for economical use. The system efficiency and Q need to be improved so that the ratio of fusion power to input electrical power, Q', is increased by 2

$$Q' = Q \frac{\eta_i}{1 - \eta_{DC}\eta_i} \quad ,$$

where Q is the ratio of fusion power to trapped injected power, η_i is the injection efficiency (including the trapping efficiency), and η_{DC} is the efficiency of direct conversion of end losses. The reference case takes $Q = 0.935$, $\eta_i = 0.7$, $\eta_{DC} = 0.5$, $Q' = 1.007$. If the following values were achieved, then the electric cost would be competitive and only the capital cost would have to be improved by a factor of 4 or more: $Q = 1.1$, $\eta_i = 0.85$, $\eta_{DC} = 0.63$, $Q' = 2.014$. We do not now know how to obtain such an additional large improvement over our reference design.

Table A-1. Cost estimate for electric breeder.

Nuclear Island:			Millions of $[a]
Magnet	$302 \times \sqrt{2} = 427$		
Injector, 2 @ 47	94		
Blanket	40		
Shield	77		
Direct energy converter 2 @ 25	50		
Vacuum system	27		
Tritium system	90		
Diagnostic	0.75		
Plasma start-up	2		
Total nuclear island construction (A)			808
Engineering, 2.5% of (A)			20
Contingency, 20% of (A)			162
		Total nuclear island:	990
Thermal System:			
Helium cooling system	16		
Steam system (heat exchanges)	80		
Electrical substation	–		
Cooling water systems	12		
Controls and instrumentation	2		
Total thermal conversion system construction (B):			110
Engineering, 5.6% of (B)	2		
Contingency, 3% of (B)	1		
Total thermal conversion system:			33
Total building facilities and site (C)			45
Temporary facilities, 0.4% of (A), (B), & (C)			4
Other costs (Taxes, insurance, training start-up, administration, licensing, etc.) 3.6% of (A), (B), and (C)			38
		Total (D):	1110
Interest during construction, 24% of (D)			266
		Total plant cost:	1376

[a] In 1975 dollars.

Appendix B. Comments on the Utilization of Fissile Fuel Produced in the Hybrid Fusion-Fission Reactor

The 690 kg of plutonium produced per year in our reference case (1380 kg in the scaled high-power case, Table 2-4) can be used either to refuel or as initial loading of essentially any reactor. The bred fuel then can be used to produce power in addition to the 611 MW_e in our reference case. To put this extended power yield in perspective, we note that each atom of Pu will yield about 190 MeV/$(1 - C_R)$ energy, where C_R is the conversion ratio for the particular fission reactor and fuel cycle considered. The 690 kg Pu/yr can produce 840 $MWy_e/(1 - C_R)$ in a fission reactor with a 40% thermal efficiency and an 80% duty factor. In Fig. B-1, we plot the electrical power produced from both the hybrid and fission reactors as a function of C_R.

It is also interesting to ask what the total cost would be for a hybrid fuel producer plus the burner fission reactors it fuels. For this example, we will take the cost of the fission reactor to be \$700/kW_e and our reference hybrid reactor cost to be \$2000/kW_e. The total cost is then

$$\frac{\$2000/\text{kW} \times 611\ \text{MW} + \$700 \times \frac{840\ \text{MW}_e}{(1 - C_R)}}{611 + \frac{840}{1 - C_R}},$$

which is plotted in Fig. B-2. Note that for converter reactors such as the high-temperature gas-cooled reactor (HTGR) or the heavy-water reactor (HWR) such as the Canadian CANDU reactor, the incremental cost for the fuel producing hybrid is only about \$100/kW. This

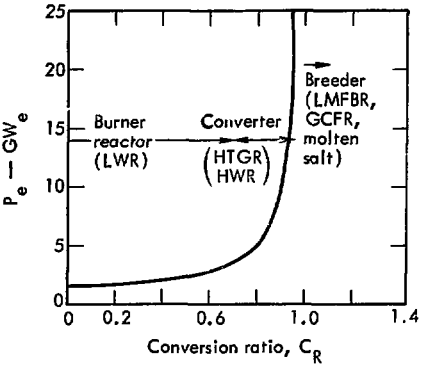

Fig. B-1. Electrical power from both hybrid and fission reactor.

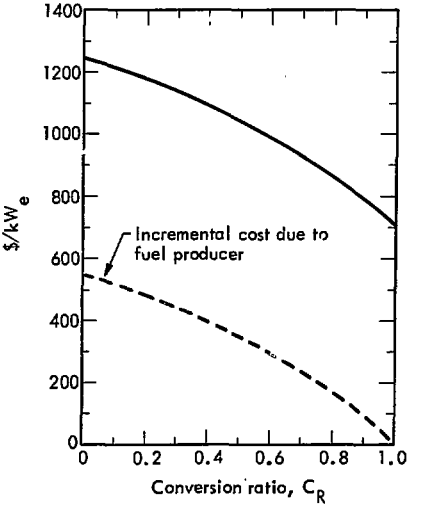

Fig. B-2. Capital cost of hybrid plus fission reactor.

incremental cost would be even less for our projected optimized hybrid (see for example in Table 2-4). In both cases (Figs. B-1 and B-2), only make-up fuel is considered. Initial core loading is not included.